GEOCHEMICAL AND GEOCHRONOLOGICAL CONSTRAINTS ON THE

TECTONOTHERMAL HISTORY OF THE CENTRAL AND EASTERN NEPAL

HIMALAYA: IMPLICATIONS FOR THERMAL-MECHANICAL MODELS

by

Stacey Lynn Corrie

A dissertation

submitted in partial fulfillment

of the requirements for the degree of

Doctor of Philosophy in Geosciences

Boise State University

May 2010

BOISE STATE UNIVERSITY GRADUATE COLLEGE

DEFENSE COMMITTEE AND FINAL READING APPROVALS

of the dissertation submitted by

Stacey Lynn Corrie

Dissertation Title: Geochemical and Geochronological Constraints on the Tectonothermal History of the Central and Eastern Nepal Himalaya: Implications for Thermal-Mechanical Models

Date of Final Oral Examination: 02 April 2010

The following individuals read and discussed the dissertation submitted by student Stephanie Stacey Starr, and they also evaluated her presentation and response to questions during the final oral examination. They found that the student passed the final oral examination, and that the dissertation was satisfactory for a doctoral degree and ready for any final modifications that they explicitly required.

Matthew J. Kohn, Ph.D.	Chair, Supervisory Committee
Mark D. Schmitz, Ph.D.	Member, Supervisory Committee
Clyde J. Northrup, Ph.D.	Member, Supervisory Committee
Delores M. Robinson, Ph.D.	External Examiner

The final reading approval of the dissertation was granted by Matthew J. Kohn, Ph.D., Chair of the Supervisory Committee. The dissertation was approved for the Graduate College by John R. Pelton, Ph.D., Dean of the Graduate College.

ACKNOWLEDGEMENTS

Dr. Mark Harrison, Dr. Jane Gilotti, and Dr. Erik Scherer. Additional thanks go to Dr. Chris Parkinson for collecting the Arun River samples.

Oceans of thanks go out to all the monkeys (i.e., other grad students) I have interacted with over the past many years; without them, I would have died of boredom and/or insanity a long time ago. Shine on you crazy diamonds.

To whoever came up with the nifty idea of fermented beverages – Here's to you for dulling the pain just a little.

To Jim, for making me happy.

Above all, I wish to thank my parents for their continued love, support, and yes, occasional befuddlement over my total immersion in academia. This work is a product of much contemplation, idea gestation, frustration, mood swings, and angry outbursts, plus long hours of labor, pain, and breakthroughs. Congratulations Mom and Dad on your first grandchild! It's a dissertation, and it is dedicated to you.

ABSTRACT

Syntheses of Himalayan tectonics imply an average shortening rate of ~2 cm/yr across the Himalaya over the last 20-25 Myr. However, despite decades of research, basic questions still remain about how strain was partitioned. Fluctuations in the timing and rate of thrusting could have significant implications for strain partitioning across the Himalaya, and for partitioning during collisional orogenesis as a whole.

Due to the observed chronology and thermobarometry of Greater Himalayan Sequence (GHS) rock units in the Annapurna region of central Nepal, we revise the original interpretation of the Bhanuwa Fault from a normal fault to a thrust, and identify a new thrust called the Sinuwa Fault structurally above the Bhanuwa thrust. The calculated slip rates for the Sinuwa (ST), Bhanuwa (BT), and Main Central (MCT) Thrusts show P-T-t consistency with a 2 cm/yr convergence rate component across the Himalaya from ~25 to ~15 Ma. These results support models that presume constant rates since at least 25 Ma. The similarity in inferred peak ages for the ST, BT, and MCT could in principle indicate simultaneous initial cooling of all three sheets at ~22 Ma. A simple explanation would involve transport and cooling of each rock package along the same basal thrust (the MCT), and later juxtaposition of already-cooled rocks along the ST and BT. That is, this model implicitly requires as much as 100 km of out-of-sequence thrusting. Additional measurements from other parts of the orogen in India and Bhutan are needed to verify whether these estimates could be applied to the orogen as a whole.

Lu-Hf dates from garnet separates in one relict eclogite from the Arun River valley in eastern Nepal indicate an age of 20.7±0.4 Ma, the first direct measurement of the timing of eclogitization in the central Himalaya. Four proximal garnet amphibolites from structurally lower horizons are 14-15 Ma, similar to post-eclogitization ages published for rocks along strike in southern Tibet. P-T calculations indicate three metamorphic episodes for the eclogite: eclogite-facies metamorphism at 23-16 Ma, a peak-T granulite metamorphism, and a late-stage amphibolite-facies metamorphism at ~14 Ma. Three models are considered to explain the observed P-T-t evolution. The first assumes that the Main Himalayan Thrust (basal thrust of the Himalayan thrust system) cuts deeper at the Arun River valley than elsewhere. While conceptually the most simple, this model has difficulty explaining both the granulite-facies overprint and the pulse of exhumation between ~25 and 14 Ma. A second model assumes that (aborted) subduction, slab breakoff, and ascent of India's leading edge occurred diachronously: ~50 Ma in the western Himalaya, ~25 Ma in the central Himalaya of Nepal, and presumably later in the eastern Himalaya. This model explains the P-T-t path, particularly heating during initial exhumation, but implies significant along-strike diachroneity, which is generally lacking in other features of the Himalaya. A third model assumes repeated loss of mantle lithosphere, first by slab breakoff at ~50 Ma, and again by delamination at ~25 Ma; this model explains the P-T-t path, but requires geographically restricted tectonic behavior at Arun. The P-T-t history of the Arun eclogites may imply a change in the physical state of the Himalayan metamorphic wedge at 25-16 Ma, ultimately giving rise to the Main Central Thrust by 16-15 Ma.

TABLE OF CONTENTS

LIST OF TABLES

LIST OF FIGURES

CHAPTER 1. INTRODUCTION

1.1 Introduction to Himalayan Orogen

Stretching over 2400 km from Nanga Parbat in Pakistan eastward across parts of India, Nepal, and Bhutan, to Namche Barwa in Tibet (Figure 1.1), the Himalayan mountain belt is one of the most prominent and striking examples of continent-continent collisional orogenesis. Approximately 400-700 km of shortening have been taken up across the Himalaya since 20-25 Ma (e.g., Yin and Harrison, 2000; DeCelles et al., 2001; Guillot et al., 2003; Robinson et al., 2006), which corresponds well with the modern Himalayan accommodation rate of ~2 cm/yr extrapolated over 20-25 Myr (Bilham et al., 1997; Larson et al., 1999). During this time, sediments initially deposited on the northern continental margin of India were buried, deformed, metamorphosed, and exhumed, with these same processes continuing through to the present. The Himalaya therefore present scientists with an ideal setting in which to test models of collisional orogenesis.

1.2 Description of the Research

Metamorphic rocks are commonly exposed in the Himalaya, and geologists recognized that the relationships between the metamorphic rocks and the fault zones that cut them are critical to understanding the processes that created the orogen (e.g., Gansser, 1964; Le Fort, 1975). Numerous studies have focused on Himalayan metamorphic rocks, particularly the highest-grade rocks exposed in the thrust belt, the Greater Himalayan

Sequence (GHS). GHS rocks are exposed along a strip in the geographic interior of the orogen, where they rest structurally above the Lesser Himalayan Sequence (LHS) along the Main Central Thrust (MCT). Most researchers find increasingly high-grade rocks exposed at progressively higher structural levels as one progresses from the Main Frontal Thrust northward toward the South Tibetan Detachment. This pattern of metamorphism is referred to as inverted metamorphism, and explanations for this feature are critical components of tectonic evolution models for Himalayan orogenesis (e.g., Le Fort, 1975; England and Molnar, 1993; Jamieson et al., 1996; Harrison et al., 1999a).

Understanding any evolutionary process is directly related to how well we understand the timing of events. The goal of this study is to contribute to our understanding of the timing and processes involved in the formation of the Himalayan orogen through an examination of the tectono-thermal history of portions of the exhumed crystalline core of the Himalaya (the GHS). Combining metamorphic petrology with geochronology and geochemistry permits the construction of pressure-temperature-time (P-T-t) histories and an estimation of the rates and mechanisms of crustal shortening. This information allows examination of the thermal evolution of the crystalline core of the Himalaya in the context of recent evolutionary models. Key questions addressed by this research include:

1) Has the Indo-Asian convergence rate remained constant at ~2 cm/yr, or has it fluctuated significantly over time?

2) Can strain measurements and shortening rate estimates from one location be extrapolated across the orogen, or are they only valid for that region?

3) Was movement along the major faults (specifically, the MCT) in different

regions contemporaneous, or was movement stalled in some areas while active

in others?

4) Was the Greater Himalayan Sequence in the central Himalaya partially

subducted in the Cenozoic?

5) Is the behavior of the crust during Himalayan orogenesis sufficiently explained

by the thermal-mechanical model of channel flow (Beaumont et al., 2001, 2004;

Jamieson et al., 2002, 2004), which calls for a combination of focused erosion and

an extremely weak middle and lower crust, or instead the critical taper model

(e.g., Henry et al., 1997), which is based on maintaining a certain wedge

geometry?

Addressing these issues is not only important to the development of the Himalaya,

but also is relevant to the overall behavior of continental crust during collisional

orogenesis.

1.3 Organization of the Dissertation

This dissertation is organized into six chapters. The first provides the reader with

an introduction to the Himalayan orogen, and sets out the questions and goals of this

dissertation.

Chapter 2 describes the geology of the Himalaya, emphasizing the major

tectonostratigraphic units and major fault systems. This chapter also reviews the two

major end-member thermal-mechanical models of Himalayan development and how each

model can be tested by examining the age and P-T history of the crystalline core of the Himalaya (i.e., the Greater Himalayan Sequence, GHS).

Chapter 3 reviews the methodology used to obtain geochronologic and geochemical data from rock samples collected along two transects through the crystalline Himalaya of central and eastern Nepal. It details operating conditions for *in situ* monazite Th-Pb ion microprobe dating as well as the chemical and instrumental protocols for Lu-Hf garnet dating via multi-collector inductively coupled plasma mass spectrometry (MC-ICP-MS). Additionally, operating procedures for gathering chemical information via the electron microprobe and laser ablation inductively coupled plasma mass spectrometer (LA-ICP-MS) are given.

Chapter 4 presents thermobarometry and monazite geochronology from the first of two transects studied over the course of this project – the Annapurna transect along the Modi Khola in central Nepal. The data are used to suggest 1) that distinct chemical zones in monazite are petrologically linked to geochronology; 2) the presence of three distinct groups of rocks within GHS Formation I; 3) the presence of an unrecognized fault within Formation I that we refer to as the Sinuwa Thrust; and 4) that strain measurements in one part of an orogen can be realistically extrapolated to another part within a few hundred kilometers.

Chapter 5 presents thermobarometry and garnet geochronology from the second transect – the Arun River valley in eastern Nepal. These data represent the first attempts to directly date high-pressure eclogitization in the central Himalaya, although several attempts have been made to date the over-printing granulite metamorphism in the region. The age and evolution of eclogites in this study contrast markedly with the ultra-high

pressure eclogites from the northwest Himalaya in a number of ways. The Arun rocks were metamorphosed at much lower pressures, show significant heating during initial exhumation, and were metamorphosed 20-30 Myr later, potentially signaling different tectonic processes between the two regions.

Chapter 6 is the conclusion of the dissertation. The major contributions of this research are summarized and the potential for new work is discussed.
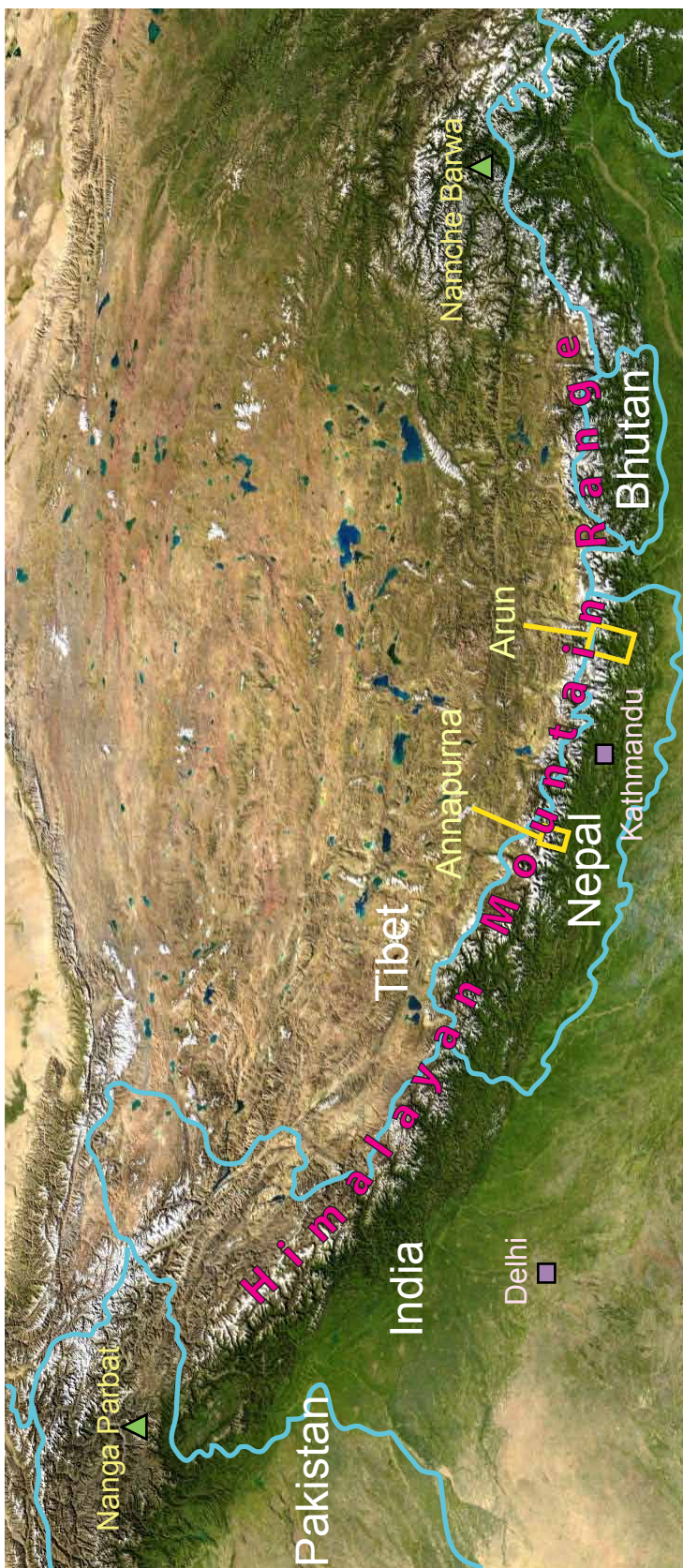
Figure 1.1. Satellite image of the Himalayan orogen, showing the expanse of the Himalayan Range. Purple squares are major cities, green triangles are the major peaks representing the syntaxes, yellow boxes represent field areas for this study.

CHAPTER 2. GEOLOGY OF THE HIMALAYA

Prior to Indo-Asian collision, the northern Indian plate was probably composed of a thinned continental margin covered by Proterozoic clastic deposits and a Cambrian-Eocene shelf sequence (Le Fort, 1996). At present, the collisional mountain belt features roughly parallel, south-directed crustal-scale fault systems that bound distinctive lithologic units along strike.

2.1 Major Tectonic Subdivisions and Structures

2.1.1 Geology of the Major Tectonostratigraphic Units

In general, laterally extensive, crystalline thrust sheets of the Nepalese Himalaya can be grouped into two main lithotectonic units: the Greater Himalayan Sequence (GHS) and the Lesser Himalayan Sequence (LHS), which are bounded above by the South Tibetan Detachment System (STDS), and below by the Main Boundary Thrust (MBT) (Figure 2.1).

Greater Himalayan Sequence (GHS)

Also called the High Himalayan crystallines, the high-grade metasediments of the GHS form the metamorphic core of the Himalayan orogen. Throughout much of Nepal, the crystalline rocks of the GHS are commonly grouped into three formations: I, II, and III (LeFort, 1975; Colchen et al., 1986; Pêcher and Le Fort, 1986). In central Nepal, the

lowest structural unit of the GHS, Formation I, consists of migmatitic upper amphibolite-facies two-mica schist and gneiss of generally pelitic composition. Formation II is composed of alternating beds of pyroxene and amphibole-bearing calc-silicate, marble, and quartzite. Formation III is a thin unit of pelitic schist and an augen gneiss. In this study, we further divide GHS Formation I into three subgroups: 1a, 1b, and 1c based on petrology. Formation 1a is muscovite-rich and contains garnet that exhibits growth zoning and/or oscillations of the major elements. Formation 1b rocks are locally migmatic and the garnets have homogenous zoning. Formation 1c rocks are migmatitic with segregated leucosomes and zoning in garnet that shows thick resorption rims following diffusional homogenization.

In eastern Nepal, the convention of dividing the GHS into 3 units is maintained, though the names and mineralogies differ (Lombardo et al., 1993; Pognante and Benna, 1993; Carosi et al., 1999; Goscombe and Hand, 2000). Comparable to Formation I in central Nepal, the Barun Gneiss also consists of migmatized pelitic schist and gneiss, but is additionally interbedded with intermittent metabasites and calc-silicates. The middle unit, the Namche Migmatite orthogneiss, is composed of sillimanite-bearing granitic orthogneisses. The upper unit in the GHS of eastern Nepal is the Black Gneiss, a high-grade pelitic paragneiss with interbedded quartzite. The uppermost sections of the GHS typically contain abundant leucogranite intrusions that are the product of early Miocene crustal anatexis from dehydration melting of the GHS (Harris and Massey, 1994; Harrison et al., 1999a, 1999b; Kohn, 2008). The depositional age for the sedimentary protolith of the GHS is estimated at 600-500 Ma based on detrital zircon ages and c. 500 Ma felsic intrusions (DeCelles et al., 2000; Gehrels et al., 2003). Some researchers have

suggested a two-stage metamorphic history of the GHS, with Neogene metamorphism preceded by an Eocene ("Eohimalayan") metamorphic and anatectic(?) event in the GHS related to nappe burial and crustal thickening (Pognante and Benna, 1993; Vannay and Hodges, 1996; Hodges et al., 1996; Coleman, 1998; Godin et al., 2001). Chronologic evidence for an Eohimalayan event comes from monazite grains containing an inherited component of Oligocene-Eocene age (Hodges et al., 1996; Edwards and Harrison, 1997; Coleman, 1998; Coleman and Hodges, 1998). However, without the benefit of direct correlation between the ages and chemical zonation, it is uncertain whether these monazites formed due to early solid-state metamorphic reactions, as in the Langtang region of Nepal, ~200 km to the east (Kohn et al., 2004, 2005), or as a result of partial melting, as was inferred by Godin et al. (2001).

Lesser Himalayan Sequence (LHS)

The LHS is often split into two sub-units: lower Lesser Himalayan (LLHS) and upper Lesser Himalayan (ULHS). The LLHS consists of the weakly metamorphosed metasediments of the Kuncha Formation, typically chlorite schists and quartzites, sporadically interbedded with orthogneisses, felsic metavolcanics, and metabasalts. The ULHS comprises greenschist- to amphibolite-facies schists, marbles, and calc-silicates of the Dhading (dolomitic marble), Benighat (carbonaceous pelite), and Malekhu (marble and calcic schist) Formations. Older and younger LHS rocks are separated by a major unconformity contemporaneous with Pan-African tectonics (Valdiya, 1995). The lower, older formations are interpreted as proximal to a Paleoproterozoic (c. 1830 Ma) continental arc that bordered the northern margin of the Indian plate, the leading edge of

which is now buried beneath the Himalaya and Tibet (Kohn et al., 2010). Permian to

Paleocene sedimentary rocks of Gondwanan affinity overlie the Dhading-Benighat-

Malekhu sequence (Sakai, 1983).

In general, the metamorphic grade within the LHS increases structurally upward

towards the MCT, i.e., an inverted metamorphic field gradient (Pêcher, 1989).

Metamorphic grade in LHS rocks ranges from chlorite- to garnet-grade toward the MCT,

and in some areas, the upper part of the unit reached kyanite-grade conditions.

Metamorphic grade in the LHS is seemingly correlated with structural position below the

MCT. A number of studies have endeavored to explain this phenomenon, as it is a key

feature in tectonic reconstructions of the Himalaya (more in Section 2.1.3).

2.1.2 Major Fault Systems

Within the GHS and LHS are several north-dipping faults with various

displacement amounts, timing, and rates. Himalayan faults have typically progressed in

sequence, so from highest structural position to lowest, the major faults of the crystalline

Himalaya are:

South Tibetan Detachment System (STDS)

This fault is an extensional feature rather than a thrust, and its development is

important to the tectonic evolution of the Himalayan metamorphic core. The STDS

juxtaposes low-grade Tethyan metasediments against the high-grade migmatites of the

GHS, and it is now generally believed that movement of the MCT and STDS was

synchronous at ≤16-17 Ma (see Edwards and Harrison, 1997; Hodges et al., 1998;

Harrison et al., 1998 for age of STDS; Kohn et al., 2004 regarding timing of main

movement on the MCT).

Main Central Thrust (MCT)

Generally speaking, the MCT is the fault along which the GHS was thrust

southward over the LHS. Despite the fact that the MCT is a fundamental feature in

tectonic reconstructions of the Himalaya (e.g., Yin, 2006 and references therein), some

contention exists regarding the characteristics and location of the boundary, stemming

from dispute over the various criteria used to identify the MCT. The crustal architecture

of the orogen is made difficult in some regions by the presence of at least two major

faults, one or both of which have been mapped as the MCT (or MCT-I, MCT-II, upper

MCT, lower MCT, etc.) at several different structural and stratigraphic levels (see review

of Yin, 2006). The MCT has been mapped: 1) as a metamorphic contact by following the

kyanite isograd (e.g., Bordet, 1961; Le Fort, 1975; Colchen et al., 1986); 2) as a

lithological contrast between a distinctive quartzite beneath an orthogneiss (Daniel et al.,

2003); 3) by differences in Sr and/or Nd isotope compositions (Ahmad et al., 2000;

Robinson et al., 2001; Martin et al., 2005; Richards et al., 2005, 2006); 4) by differences

in U-Pb detrital zircon ages (Parrish and Hodges, 1996; DeCelles et al., 2000); 5) by

discrete Th-Pb monazite ages (Harrison et al., 1997; Catlos et al., 2001, 2002; Kohn et

al., 2004); 6) using strain indicators to find the maxima of a shear gradient (Martin et al.,

2005; Searle et al., 2008); 7) as an entire zone of high ductile strain up to 10 km thick that

is bounded above and below by related thrusts (e.g., Catlos et al., 2001; Grujic et al.,

2002). There are difficulties in using any one of these methods independently to define

the MCT. General lithology, detrital zircons, and isotopic analysis provide information on stratigraphy, and mineral isograds and monazite ages provide information about metamorphic reactions. As a structural feature, the MCT should be defined to a first order by structural methods, i.e., strain analysis (Martin et al., 2005; Searle et al., 2008). However, due to variable rheological responses from different rock types, potential pre-existing stratigraphic and tectonic structures, and possible migration over time of the main locus of thrusting on the MCT, strain analysis alone does not present a clear definition of what, or where, the MCT should be. Additionally, a lack of an obvious break in metamorphic grade between the LHS and GHS across the MCT makes it difficult to distinguish in the field. For this study, the MCT is assigned to the GHS-LHS contact, defined on a combination of lithologic, isotopic, and geochronologic criteria.

Chronologically speaking, initial movement on the thrust was generally viewed as being ~20-22 Ma based on hornblende ^{40}Ar/^{39}Ar and monazite U-Pb ages (Hubbard and Harrison, 1989; Hodges et al., 1996; Johnson et al., 2001). However, more recent work has suggested initial movement on the MCT in central Nepal and Bhutan at 16±1 Ma and crystallization of *in situ* melts by 13 Ma (Daniel et al., 2003; Kohn et al., 2004, 2005). The displacement on the thrust is estimated to be ~125 km (DeCelles et al., 2001, 2002; Robinson et al., 2003, 2006; Kohn et al., 2004), with a displacement rate of about 2 cm/yr between 16 and 10.5 Ma (Kohn et al., 2004).

Munsiari Thrust (MT)

In central Nepal, the MT (also referred to as the Ramgarh Thrust: DeCelles et al., 2001) sits just below the MCT and emplaces stratigraphically lower LHS atop

stratigraphically higher LHS (Robinson et al., 2003; Kohn et al., 2004; Pearson and DeCelles, 2005). It was first active in central Nepal at 10.5±0.5 Ma (Kohn et al., 2004). Displacement on the thrust is estimated at ~120 km in western Nepal and ~110 km in central Nepal (DeCelles et al., 2001; Robinson et al., 2003, 2006; Kohn et al., 2004).

Lesser Himalayan Duplex (LHD)

In central Nepal, the LHD is not well exposed; however, metamorphic ages that have been collected within the duplex range from ~8 Ma to 3 Ma (Catlos et al., 2001, 2002; Kohn et al., 2004). The geometry of some of the P-T paths assembled for LHS rocks suggest that there is at least one thrust between the MT and the MBT, providing petrologic support for a duplex (Catlos et al., 2001; Kohn et al., 2001). In western Nepal, the LHD accommodated ~300 km of shortening (Robinson et al., 2006), but in central Nepal, displacement is more difficult to estimate due to the strong influence of erosion on cooling; in this region, exhumation and cooling rates have been calculated at 6-7 mm/yr and >150°C/Myr, respectively (Lavé and Avouac, 2001; Kohn et al., 2004), comparable to erosion rates at both the eastern and western syntaxes (Zeitler et al., 2001; Stewart et al., 2004).

Main Boundary Thrust (MBT)

The MBT places the lowest-grade crystalline rocks of the LHS on top of the unmetamorphosed Siwalik Group syntectonic clastic rocks to the south. Initial movement on the fault has been placed as early as ~5 Ma (DeCelles et al., 1998).

Main Himalayan Thrust (MHT)

The MHT is the main decollment beneath the Himalaya. All of the other major thrusts in the Himalaya are believed to sole into the MHT (Zhao et al., 1993; Nelson et al., 1996), implying that the main faults within the GHS are abandoned and exhumed former MHT surfaces (Kohn, 2008).

2.1.3 Inverted Metamorphic Field Gradient

The most distinctive feature of Himalayan metamorphism is its inverted metamorphic field gradient, which forms a gradual progression from chlorite-grade at the base of the LHS to sillimanite-grade toward the top of the GHS. This does not necessarily represent an inverted geotherm, however. Inverted metamorphism has been associated with regions that have experienced widespread thrust faulting (Ernst, 1973; Graham and England, 1976; Spear et al., 1995). Models of inverted metamorphism in central Nepal include pre- to syn-metamorphic thrusting and then thermal relaxation (Le Fort, 1975; Hubbard and Harrison, 1989; Molnar and England, 1990; Macfarlane, 1995), syn- to post-metamorphic thrusting (Harrison et al., 1998; Huerta et al., 1998), or post-metamorphic thrusting (Inger and Harris, 1992; Hubbard, 1996). Age distributions and P-T histories of rocks from central Nepal seem consistent with a thermotectonic model in which the inverted metamorphic sequences formed during continuous syn-metamorphic to post-metamorphic thrust-sense shearing which caused heating of footwall rocks during transport of the hot hanging wall (Harrison et al., 1998; Catlos et al., 2001; Kohn et al., 2001, 2004; Kohn, 2008).

2.1.4 Magmatism

Many geochronological studies of the Himalaya have concentrated on leucogranites from Nepal and the south Tibet section of the Himalayas, and these studies show that the most important period of leucogranite production occurred ~20–24 Ma (e.g., Schärer, 1984; Harrison et al., 1999b). The most intensively studied pluton in the Himalaya is the Manaslu leucogranite. The pluton intrudes high-grade rocks at the top of the Greater Himalayan Sequence, but does not cross-cut the South Tibetan Detachment (Searle and Godin, 2003). The Manaslu leucogranite is located ~100 km east-northeast of Annapurna, making it the closest large leucogranite body to the Annapurna region. Ion microprobe monazite data indicate that the Manaslu intrusive complex was constructed during pulses of magmatism at 22.9 ± 0.6 Ma and 19.3 ± 0.3 Ma, with the second phase representing approximately one-third of the overall leucogranite exposure (Harrison et al., 1999b). At Annapurna, Hodges et al. (1996) reported ~22.5 Ma deformed kyanite-grade migmatitic segregations in Formation I above the Main Central thrust, and zircons from leucogranite dikes crosscutting Formation II calc-silicates that yield a lower intercept age of 21.5 Ma.

Leucogranites in the Rongbuk valley, on the north side of the Everest Massif and adjacent to the Qomolangma detachment, a segment of the South Tibetan detachment system, are the nearest dated igneous rocks to the Arun River valley. The leucogranites are exposed in the footwall of the detachment, dated at 16-17 Ma, and do not crosscut the fault system (Murphy and Harrison, 1999).

Overall, the ages of these high-level igneous rocks overlap inferred ages of thrusting from Annapurna, and the geochemistry of the leucogranites is broadly

consistent with derivation from a metasedimentary source (Le Fort et al., 1987; Guillot and Le Fort, 1995). There is no specific structural or geochemical link between low-level migmatites exposed in Formation 1b-1c and high-level plutons. For example, partial melts within Formation 1b-1c at Annapurna are segregated on scales of centimeters to decimeters, and lack dikes or other evidence of larger-scale mobility (Hodges et al., 1996; Martin et al., 2005).

2.2 Models for the Origin and Evolution of the Himalayan Orogen

Numerous models have been proposed to explain the evolution of the Himalayan orogen, and, in conjunction, its major fault systems (i.e., STDS, MCT, MHT), since the apparent inverted metamorphism observed in the Himalayas must be indicative of whatever tectonothermal process is at work. The two most popular models for the development of the Himalayan orogen are channel flow (Beaumont et al., 2001, 2004; Jamieson et al., 2002, 2004) and critical taper (e.g., Henry et al., 1997).

2.2.1 Channel Flow Model (CFM)

The channel flow model of the Himalaya (Beaumont et al., 2001, 2004; Jamieson et al., 2002, 2004) requires a large partial melt channel that dominates the tectonics of the orogen by coupling with the erosional front (Figure 2.2). Over time and distance (10's of Myr and up to 100's of km), the channel moves toward the orogenic front, advecting heat and bringing partially molten rocks close to the surface. Flow in the channel requires an inclined thrust surface with normal shearing between the GHS and Tethyan Himalaya, and is particularly sensitive to lateral pressure gradients and viscosity. The channel flow

model is compatible with the development of an inverted metamorphic sequence, and predicts a systematic trend in P–T–t histories across the presumed channel (Jamieson et al., 2004). For GHS rocks, P-T paths are predicted to show isothermal exhumation until rocks begin cooling relatively close to the surface (ca. 10 km depth at ca. 10 Ma) at a rate of ~150 °C/Myr.

2.2.2 Critical Taper Model (CTM)

The critical taper model (Henry et al., 1997; Bollinger et al., 2006) assumes that the Himalaya is a wedge of material between the underthrust Indian plate and the overriding Asian plate. In order to maintain its steady-state geometry, the wedge will deform internally, typically through in-sequence, flat thrusting, with thrusts soling to a master decollment; however, it does not discount the possibility of out-of-sequence thrusting that may occur should the wedge become sub-critical. Thrust packages are successively abandoned as thrusting (and deformation) propagates forward in response to underplating of new material from the Indian subcontinent. In contrast to the CFM, normal faulting at the top of the structural package (i.e., the STDS) is not a primary feature, though in the CTM, shear could have involved normal faulting if the wedge became supercritical. Another important difference between the CTM and CFM is the dominance of flow in the weak mid-crust. In critical taper, the effect of a partially molten channel is small; while the model does not rule out partial melts at depth, those melts are not transported forward to the orogenic front by flow. This would be reflected in an older crystallization age than one would expect from the CFM (ca. 20 Ma rather than ca. 10

Ma), and P-T paths for GHS rocks would show initial isobaric cooling far from the

surface at a rate of ~50 °C/Myr.

2.3 Discussion

There is a distinct lateral consistency of the first-order lithotectonic units along

strike in the Himalaya (Figure 2.1). However, there are some smaller-scale dissimilarities

between one transect and another, which may provide new evidence for the tectonic

processes at work. Regional-scale models for the Himalayan orogen need to be able to

account for local variations observed in different transects in order to provide a robust

picture of Himayalan evolutionary development. When evaluating the validity of

different tectonic models in this context, one may ask what observations might

distinguish among competing models. Since all researchers agree that the GHS was

partially molten in the middle and lower crust at one point (i.e., a weak channel), one may

further ask how strongly the channel affected the development of the orogen. While both

end-member models account for lower-level thrusting, higher-level normal faulting, and a

partial-melt zone deformed at high temperatures and consequently exhumed, they require

different thrust geometries, P-T-t histories, and kinematic relationships between the

Tethyan and GHS. Attempts will be made to explore the similarities and differences

between the two models in anticipation of finding a model that best represents the

observed and calculated data.

19
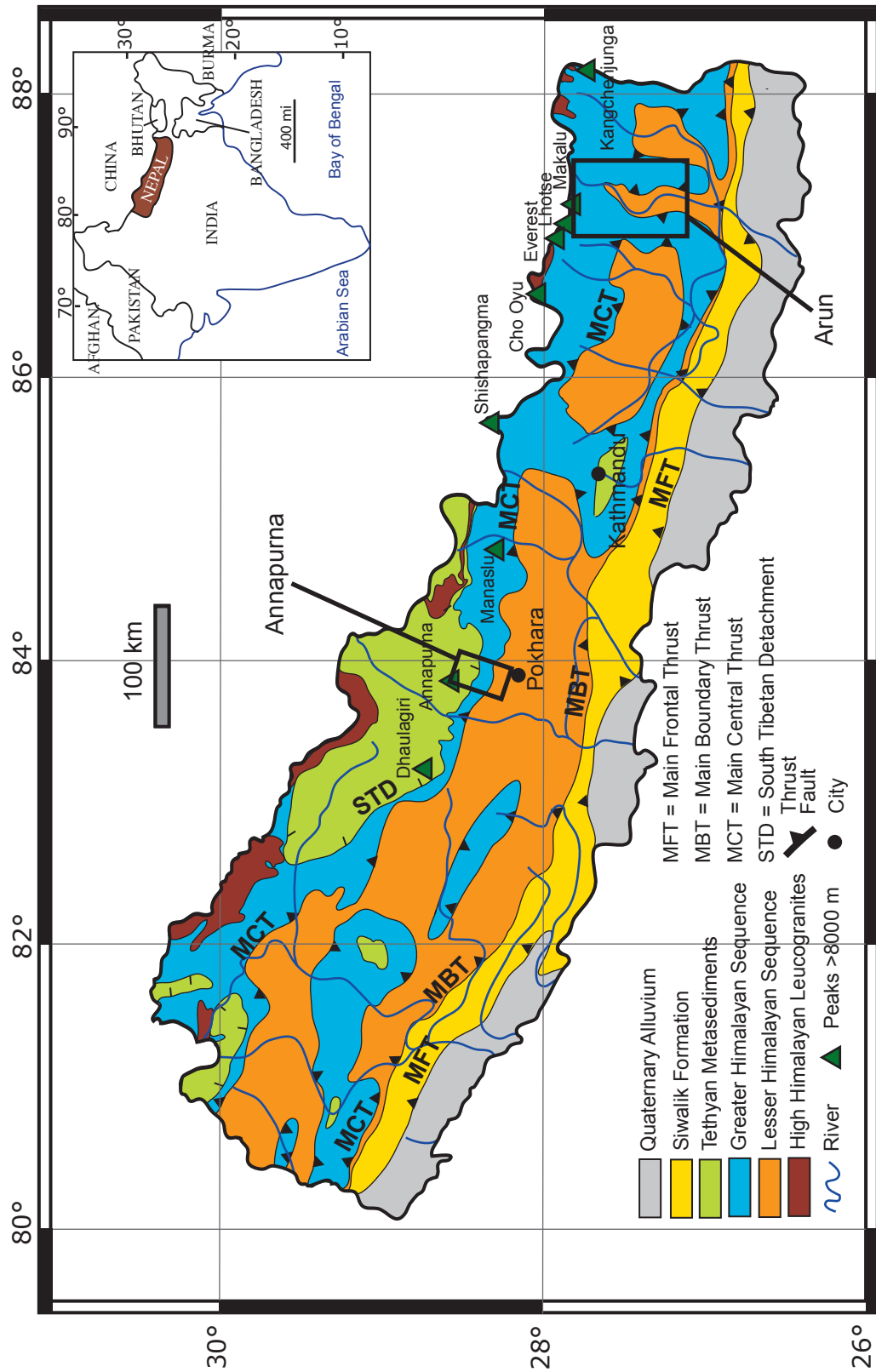
Figure 2.1. Generalized geologic map of Nepal illustrating the major tectonostratigraphic units (after

DeCelles et al., 2004). Black boxes represent field areas for this study
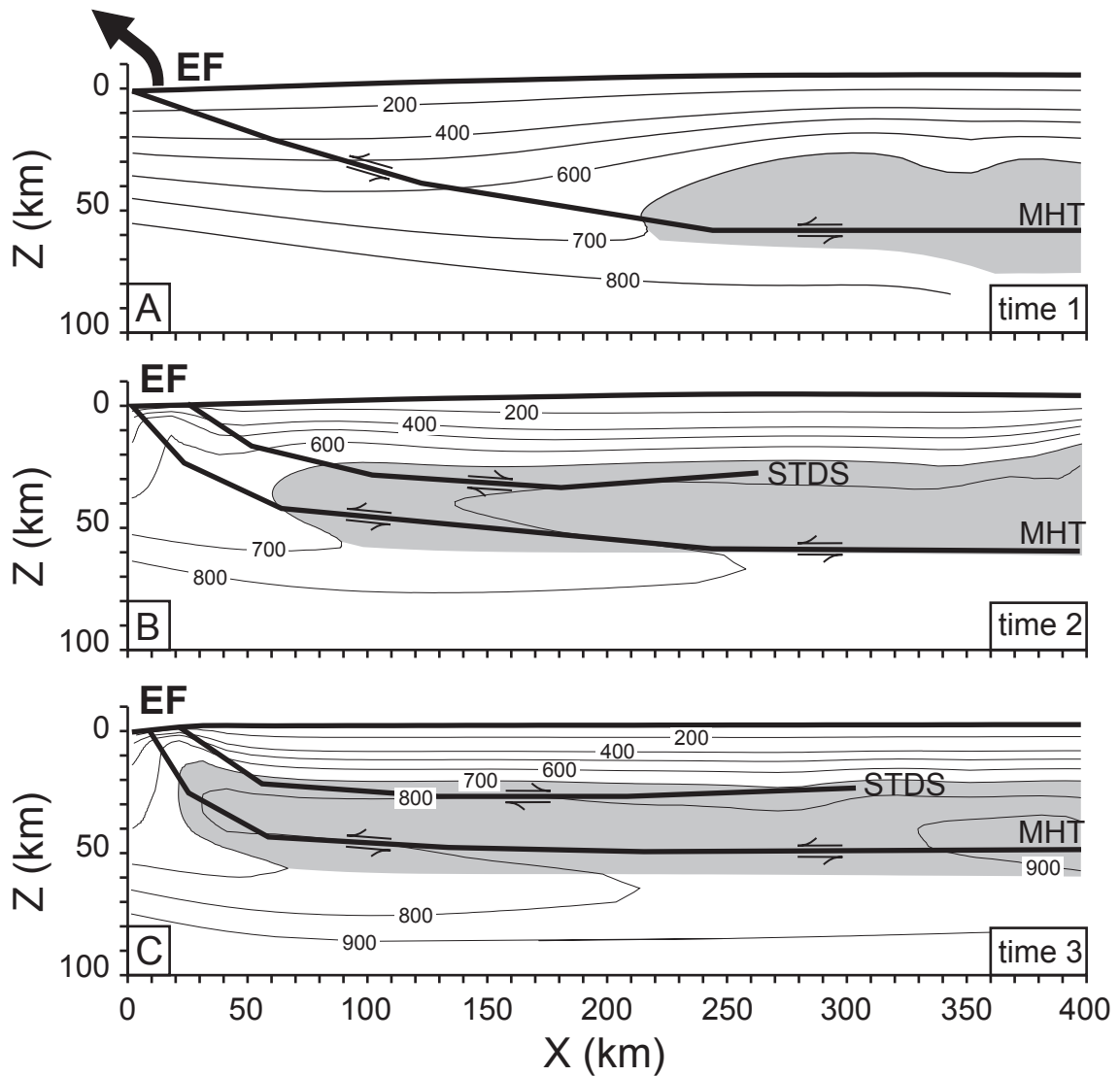
Figure 2.2. Channel Flow model of Himalayan development (from Kohn, 2008; based on Beaumont et al., 2004 and Jamieson et al., 2004). Partial melt channel (gray zone, ≥700°C) couples with an erosional front (EF) and propagates forward over time until hot, partially molten rocks are brought close to the surface before cooling begins.
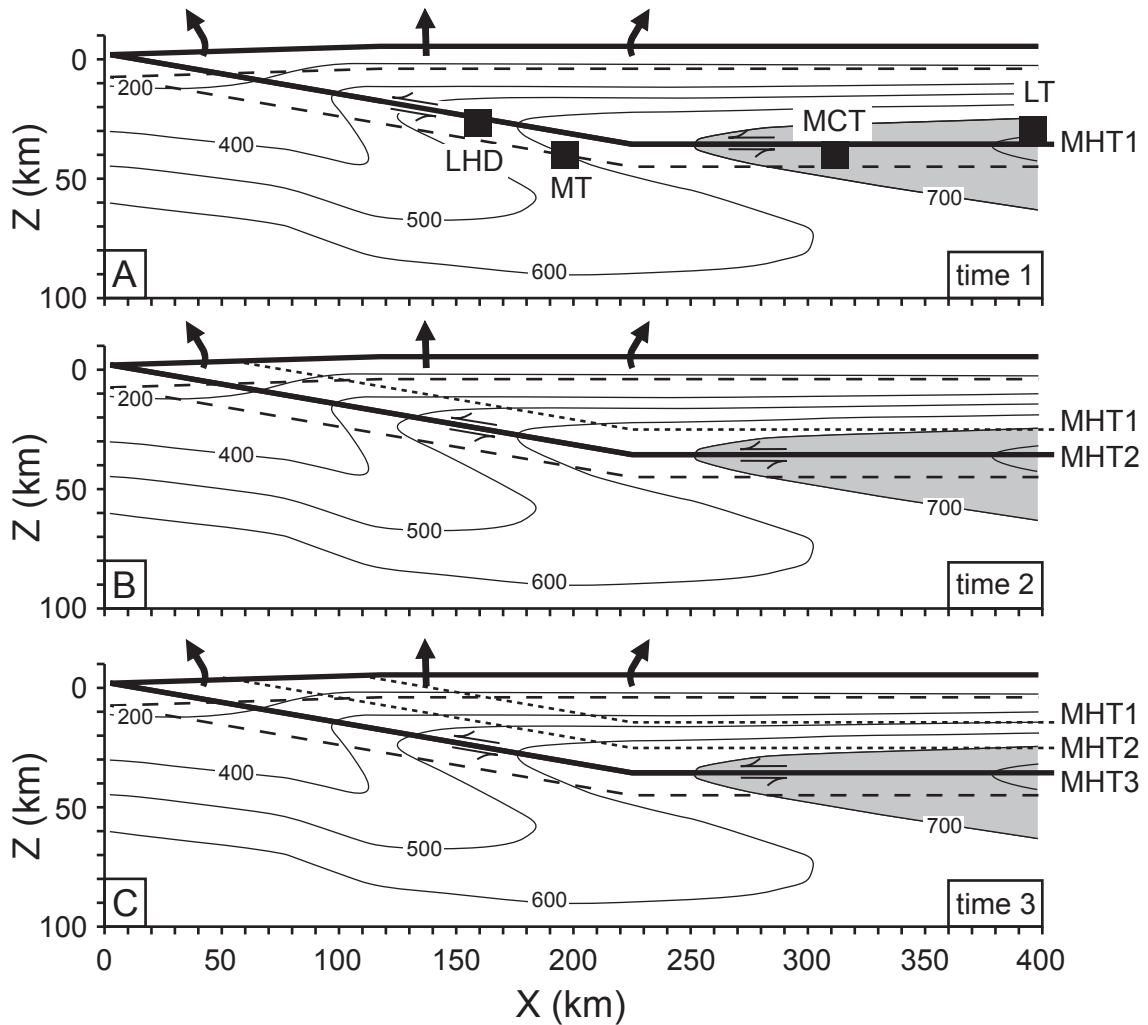
Figure 2.3. Critical taper model of Himalayan development (from Kohn, 2008; based on Henry et al., 1997 and Bollinger et al., 2006). As erosion uniformly removes material from on top of the section, thrusts progressively under-plate, creating a series of in-sequence thrusts over time. A partial melt zone exists, but remains far from the orogenic front.

CHAPTER 3. METHODS OF ANALYSIS

3.1 *In situ* Th-Pb Ion Microprobe Dating of Monazite

Monazite grains were first identified in thin section using back-scattered electron (BSE) imaging on the Cameca SX-100 electron microprobe housed in the Department of Earth and Environmental Sciences at Rensselaer Polytechnic Institute, Troy, New York. The monazite grains are typically zoned and range in size from 20 to 300 μm. Monazite grains were then X-ray mapped using the electron microprobe (operating conditions below) to identify chemically distinct zones. They were then re-identified in thin section using an optical microscope, and, using a Medenbach microdrill, were subsequently drilled from the slides in ~3 mm disks, preserving the textural relationship of the monazite grain with the surrounding matrix. The glass disks containing the monazites were then mounted in 1-inch epoxy rounds with a block of 5-10 grains of polished standards (monazite 554, Harrison et al., 1999b). To aid in locating the monazite for analyses, reflected light images were taken of each glass disk containing a monazite grain, as well as the entire epoxy round (Figure 3.1). The sample rounds were cleaned in distilled water in an ultrasonic bath, dried, and gold coated. Monazite grains were analyzed using the Cameca ims 1270 ion microprobe in Department of Earth and Space Sciences, University of California-Los Angeles.

Details of analytical protocols for ^{208}Pb/^{232}Th dating of monazite using the Cameca ims 1270 ion microprobe have been describe previously by Harrison et al. (1995, 1999b).

Operating conditions for this study involved a primary beam current of 6-10 nA, a spot size of ~10-20 μm, and a mass resolving power of 4500, which sufficiently separates all molecular interferences in the 204-208 mass range. Energy offsets were +10 to +15 eV for ^{232}Th$^+$, and -8 to -13 eV for ThO$_2^+$. Total time per spot analysis was 12 minutes. ^{208}Pb$^+$/Th$^+$ is corrected for common Pb using the relationship ^{208}Pb*/Th$^+$ = (^{208}Pb$^+$/Th$^+$)[1-(^{208}Pb/^{204}Pb)$_S$(^{204}Pb$^+$/^{208}Pb$^+$)], where (^{208Pb}/^{204}Pb)$_S$ is the known ratio of the standard; the asterisk indicates the species is corrected for common Pb. The Pb/Th relative sensitivity factor required to calculate a Th-Pb age from isotopic data obtained from an unknown monazite is determined by referring the ThO$_2$/Th ratio determined in the sample analysis to a linear calibration curve that is constructed from several ion microprobe spot measurements of ThO$_2$/Th vs. Pb/Th from standard monazite 554 (Figure 3.2). This correction factor permits the determination of Pb/Th ratios of unknown grains measured under the same instrumental conditions. Reported age uncertainties reflect counting statistics and the reproducibility of the standard calibration curve.

3.2 Garnet Geochronology

Whole rock samples were processed in a jaw crusher and sieved until the entire portion passed through a 750 μm sieve. Approximately 0.5 to 1 g of garnet was handpicked under a binocular microscope, excluding grains with abundant visible inclusions. Contrary to many other studies, garnets were still retained if they contained a moderate number of inclusions since rim fragments tended to be inclusion-free and the sought-after age is that of the core. Dissolving these fractions should have no effect on calculated age as zircon is the only phase present as an inclusion that contains measurable

Hf, and zircon is not dissolved with the garnet during table-top digestion procedures.

Sample dissolution, chemical separations, and isotopic analysis protocols follow

Vervoort et al. (2004) and Cheng et al. (2008), and are described in detail below. Each

geochronological point called for ~0.25 g of garnet or whole-rock sample. Two aliquots

of whole-rock powders were digested per sample. The first followed the same tabletop

dissolution procedure as that of garnet to determine the zircon-free whole-rock

composition. The second used high-pressure Teflon bombs to ensure total dissolution of

refractory phases, including zircon.

Stage 1: Leaching and Sample Dissolution

Approximately 250 mg of garnet separate or whole-rock powder was weighed

into clean 15 ml Savillex® beakers (or bombs, depending on dissolution method). The

garnet samples were then subjected to a light leaching process where ~4 ml 1M HCl was

added to the beakers, which were then capped, sonicated for 5 minutes, and let rest for 5

minutes. The acid was pipetted off, ~5 ml mQ H_2O was added, and the beaker was once

again sonicated for 5 minutes. The water was pipetted from the sample.

The sample dissolution procedure for garnet and whole-rock powders began by

adding 1-2 ml of a 10:1 mix of 29M HF: 14M HNO_3 to the beakers and drying them

down on a hotplate set at ~150°C. Next, 10 ml of the 10:1 mixture was added and the

beakers were capped and left on the hotplate for 24 hours. Whole-rock samples intended

for total bomb dissolution were instead inserted into steel jackets and put in an oven for 3

days. Beakers (or bombs) were then uncapped and dried down on the hotplate. A boric

acid/HCl mixture (1 ml H_3BO_3 + 2 ml 6M HCl per every 100 mg sample) was added to

complex fluorides, and the beakers were capped and left overnight on a hotplate at 100 °C. For bomb-dissolved whole-rock samples, a few additional steps were applied at this point: after the orthoboric acid step, the samples were dried down, ~10 ml 6M HCl was added, the bombs were capped and then left to sit on the hotplate overnight. The next day, the bombs were uncapped, dried down, and ~ 10 ml 6M HCl was added. The bombs were once again capped, jacketed, and put in the oven for ~6 hours. Once removed, the samples were transferred to Savillex® beakers. All samples were then dried down. 10 ml 6M HCl was added and the beakers were capped and left to equilibrate on the hotplate. Beakers were removed from the hotplate to cool, spiked with a mixed ^{176}Lu-^{180}Hf tracer, capped, equilibrated on a hotplate overnight, uncapped, and thoroughly dried down.

Stage 2: 1st Stage Hf and Lu (Separation of Hf and Lu from bulk matrix)

The sample was dissolved in 0.5 ml 6M HCl and sonicated for 5 minutes, then diluted with 2.5 ml mQ H$_2$O to make a 1M HCl solution, which was once again sonicated for 5 minutes. 20 μL 8M HF was added to the solution to complex the Hf, and the beaker was warmed on the hotplate for ~10 minutes. Each sample was transferred to two 1.5 ml centrifuge vials and centrifuged at 3000-3500 rpm for 10-15 minutes.

Columns filled with 10 ml of Bio-Rad AG50w-X12 cation exchange resin were backwashed and conditioned with 1M HCl. Only the supernatant from the centrifuge tubes was loaded onto the resin. In the load solution, Hf and other HFSE were complexed as fluoride anions which do not interact with the resin. Consequently, the columns are washed in only 1 ml 1M HCl/0.1M HF before Hf is collected with 6 additional washes of 1 ml 1M HCl/0.1M HF. The columns were washed with 5 additional ml of 1M HCl/0.1M

HF, followed by 100 ml 2.5M HCl to flush away most of the other elemental components in each sample. Lu + HREE were collected with 60 ml 2.5M HCl. To clean, columns were washed with 160 ml 6M HCl, 20 ml 6M HCl + 2 ml 8M HF, and then a full reservoir of 6M HCl. The Hf and Lu sample cuts were dried down in preparation for additional separation.

Stage 3: 2nd Stage Hf (Separation of Hf from other HFSE)

The dried sample cut of Hf from the previous separation was redissolved in 5 ml 2.5M HCl, capped, and heated to equilibrate. Columns filled with 1.0 ml of Ln-Spec resin were resettled and conditioned with 2.5M HCl. The sample was loaded onto the resin bed and washed with 10 ml 2.5M HCl, then 3 iterations of a 10 ml 6M HCl wash to remove any incorporated REE. The columns were washed with 5 ml H_2O to rinse away the HCl. To remove Ti, the columns were rinsed 4-6 times with 10 ml of 0.09M HCit/0.45M HNO_3/1wt% H_2O_2, until the orange color (created by the interaction of Ti with the citric acid) was washed from the resin, ensuring total removal of Ti. The columns were then washed with 5 ml 0.09M HCit/0.45M HNO_3 and 2 times 10 ml 6M HCL/0.06M HF. Hf was recovered in 5 ml 6M HCl/0.4M HF and dried down for the final Hf purification stage. The columns were cleaned with 10 ml 2M HF, 10 ml 6M HCl, 10 ml H_2O, and then stored in 0.14M HCl.

Stage 4: Hf Cleanup

The final stage of Hf separation and cleaning is to remove any remaining HREE that may present isobaric interferences during mass spectrometry. The columns used are

essentially extremely scaled-down versions of the 1st stage columns. To the dried Hf cut from the previous separation, 25 µL 2.5M HCl were added, and the sample was heated on the hotplate for ~5 minutes. 30 µL H_2O were added, and the sample was once again heated on the hotplate for ~5 minutes. 20 µL 0.3M HF were added, and the sample was loaded into the columns conditioned with 1M HCl. Hf was collected with 5 rinses of 50 µL 1M HCl/0.1M HF. The columns were cleaned with 120 µL 1M HCl/0.1M HF and 5 ml 2.5M HCl. The final Hf fraction was dried down, treated with 1 drop 14M HNO_3 to remove any organic compounds, dried down, treated with 1 drop 8M HF to complex the Hf with fluoride, and dried down again.

Stage 5: 2nd Stage Lu (Separation of Lu from HREE)

The dried Lu cut from the first stage separation was redissolved in 0.5 ml 2.5M HCl. Columns filled with 0.9 ml of Ln-Spec resin were resettled and conditioned with 2.5M HCl. The solution was loaded onto the columns and washed 4 times with 7.5 ml 2.5M HCl and 2 times with 5 ml 2.5M HCl, which removes most, but not all, of the Yb from the sample, leaving enough to make an accurate fractionation correction, but not so much that the ^{176}Yb interference on ^{176}Lu is prohibitively large (Vervoort et al., 2004). Lu was collected with 5 ml 6M HCl. The columns were cleaned by filling the reservoir 3 times with 6M HCl, and were then stored in 0.14M HCl. The Lu cut was dried down, treated with 1 drop 14M HNO_3 to remove any organics, and dried down again.

<u>Stage 6: Mass Spectrometry via MC-ICP-MS</u>

The dried Lu and Hf fractions were dissolved in 750-1000 μL 2% HNO3,

sonicated for 10-15 minutes, and transferred to centrifuge tubes for mass spectrometry

analysis.

Isotopic data were collected on a ThermoFinnigan Neptune™ multi-collector

inductively coupled plasma mass spectrometer (MC-ICP-MS) in the GeoAnalytical

Laboratory at Washington State University. Protocols for Lu analysis and data reduction

are described by Vervoort et al. (2004). Hafnium ratios were corrected for mass

fractionation using ^{179}Hf/^{177}Hf = 0.7325 and the exponential law for mass bias correction.

Isotopic compositions were then normalized using an external Hf standard, JMC475

(^{176}Hf/^{177}Hf = 0.282160). The average ^{176}Hf/^{177}Hf for JMC475 taken over the course of

this study was 0.282142 ± 0.000025 (2σ, n=54). External uncertainties applied to

measured data are 0.5% for ^{176}Lu/^{177}Hf and the quadratically combined 2-sigma in-run

error and a blanket 0.005% uncertainty for ^{176}Hf/^{177}Hf. Lutetium-hafnium ages were

calculated using the ^{176}Lu decay constant of 1.867×10^{-11} (Scherer et al., 2001; Söderlund

et al., 2004) and isochrons were produced using the program Isoplot/Ex (Ludwig, 2003).

Errors are reported at 95% confidence.

3.3 Electron Microprobe Chemical Analysis

Elemental compositions and X-ray maps were collected using the Cameca SX-

100 electron microprobe housed in the Department of Earth and Environmental Sciences

at Rensselaer Polytechnic Institute, Troy, New York. Natural and synthetic silicates and

oxides were used for calibrations, and quantitative measurements were made using an

accelerating voltage of 15 kV and a current of 20 nA (major silicates) or 100 nA (rutile

and titanite). A minimum beam size was used on most minerals, except plagioclase and

micas (10 μm), and rutile and titanite (2 μm). Peak count times were 10 s (Na, Ca, Fe,

Mn, Si, Al), 20 s (Mg, Ti, K), 45 s (Zr in rutile), and 75 s (Zr in titanite). Operating

conditions for the X-ray maps consisted of an accelerating voltage of 15 kV, current of

200 nA, pixel time of 30 msec, and step size of 2-5 μm/pixel. X-ray compositional maps

of the elements Fe, Mg, Mn, Ca, and Al were collected on garnet, and Th, Y, U, Ce, and

Ca on monazite. Garnet maps were collected via stage-mapping, monazites via beam-

mapping.

3.4 Laser Ablation ICP-MS

Understanding the distribution of Lu in garnet is important for interpreting Lu-Hf

isochrons within the context of progressive metamorphism. Therefore, trace element

profiles were collected across eclogite garnets using a UP193 laser and Element XA

magnetic sector ICP-MS housed at the University of Lausanne, Switzerland. Prior to data

collection, line traverses were pre-ablated with a spot size of 25 μm, a stage movement

rate of 50 μm/sec, and a power intensity of 6.2 J/cm^2, as metered directly at the surface.

Traverse data were then collected with a spot size of 15 μm, a stage movement rate of 10

μm/sec and a power intensity of 6.2 J/cm^2. Intensities were measured in low resolution

mode for a large suite of major and trace elements ranging from Mg to Hf, the most

important issue being the distribution of Lu. Raw counts of ^{175}Lu were normalized to

^{27}Al, and standardized against NIST612 glass. For sample AR01-43c, concentrations of

Lu were calculated from averages measured across the core versus rim.
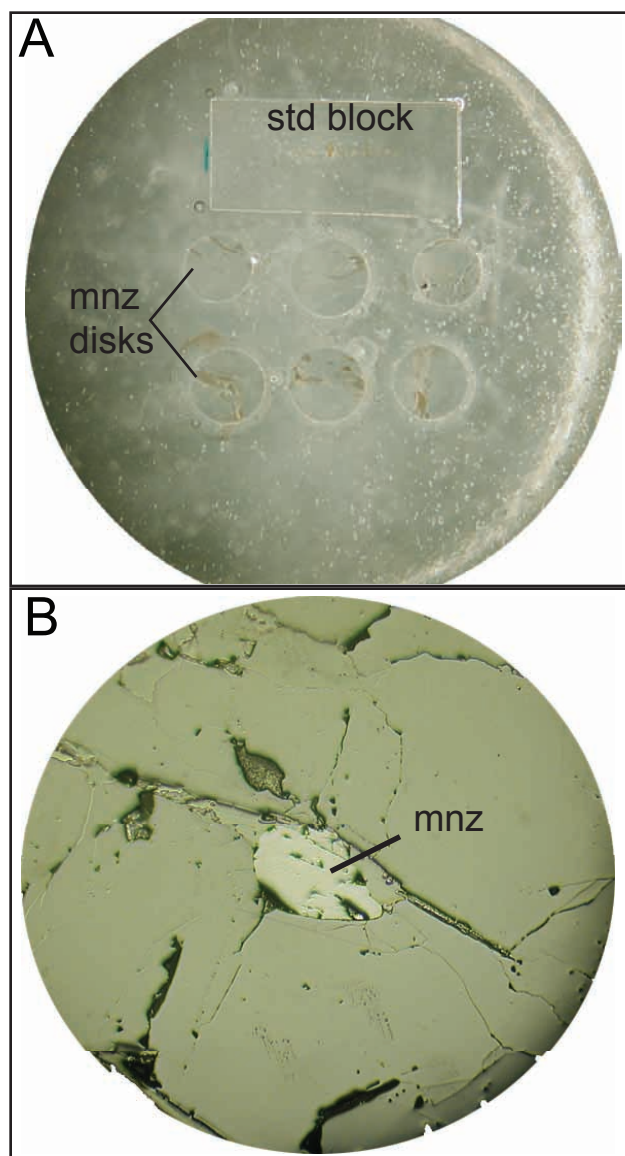
Figure 3.1. Example reflected-light images of monazite samples. A) 1-inch epoxy round containing disks drilled from thin section and rectangular block of standards. B) Example 3 mm glass disk containing monazite from sample AS01-16a.
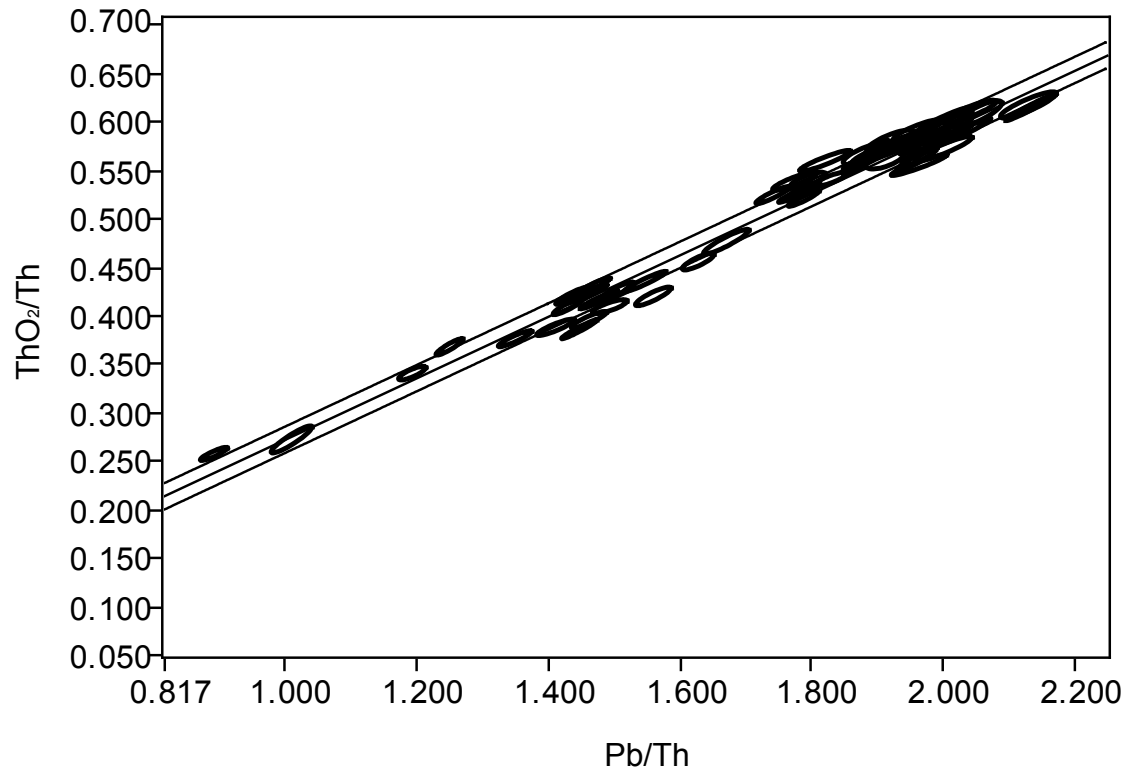
Figure 3.2. Th-Pb calibration curve for standard monazite 554 (see
Harrison et al., 1999b). Along with the age of 554 (45 ± 1 Ma), this
relationship allows the relative sensitivity factor to be calculated,
permitting determination of Pb/Th ratios of unknown monazites under
the same analytical conditions. Error ellipses represent 1σ uncertainties
on the measurement; error margin on calibration line represents 1σ
uncertainty on the calibration. n = 55.

CHAPTER 4. GEOCHRONOLOGY AND THERMOBAROMETRY OF THE

CENTRAL HIMALAYA, ANNAPURNA TRANSECT, CENTRAL NEPAL

4.1 Introduction

Syntheses of Himalayan tectonics indicate 400-700 km of shortening have been

taken up across the Himalaya over the last 20-25 Myr (e.g., Yin and Harrison, 2000;

DeCelles et al., 2001; Guillot et al., 2003; Robinson et al., 2006). The implied average

shortening rate, ~2 cm/yr, corresponds well with estimates of modern rates of shortening

across the Himalaya (Bilham et al., 1997; Larson et al., 1999). Yet despite decades of

research, basic questions still remain about how strain was partitioned. Has the

convergence rate remained constant at ~2 cm/yr, or has it fluctuated significantly over

time? Can strain measurements and shortening rate estimates from one location be

extrapolated across the orogen, or are they only valid for that region? Was movement

along the major faults in different regions contemporaneous, or was movement stalled in

some areas while active in others? Thermal and mechanical models typically assume a

constant shortening rate in the Himalaya since ~25 Ma (e.g., Bilham et al., 1997; Henry

et al., 1997; Harrison et al., 1998; Huerta et al., 1998, 1999; Beaumont et al., 2001, 2004;

Jamieson et al., 2002, 2004), but significant variations in the displacement rate on

million-year timescales have been proposed in central Nepal (Kohn et al., 2004), and

elsewhere within the Indo-Asian collision (Dunlap et al., 1998). With the development of

a new method that combines petrology and geochronology to determine thrust

displacement rates in crystalline rocks (Kohn et al., 2004), strain partitioning in the past

can be compared to present rates, as well as comparing rates and timing across the

Himalaya. Fluctuations in the timing and rate of thrusting could have significant

implications for strain partitioning across the Himalaya, and for partitioning during

collisional orogenesis as a whole.

To address these issues, samples were collected from a transect through the

crystalline Himalaya along the Modi Khola in central Nepal, south of the Annapurna

Massif (Figure 4.1). This transect is located ~200 km west of a Langtang transect that

has been studied extensively (Inger and Harris, 1992; Macfarlane, 1993, 1995; Fraser et

al., 2000; Kohn, 2004; Kohn et al., 2004, 2005) and therefore serves as a good basis of

comparison. Martin et al. (2010) reported new P-T estimates for Greater and Lesser

Himalayan rocks along the Modi Khola, but did not offer them in a geochronological

context. P-T estimates have also been published from other transects through the central

Himalaya of Nepal, including a transect along the Kali Ghandaki river to the west of the

Modi Khola (Vannay and Hodges, 1996), and along the Marsyandi (Catlos et al., 2001)

and Darondi (Kohn et al., 2001) rivers to the east between the Modi Khola and Langtang.

In order to verify whether thrusting and convergence at Annapurna had the same rate,

timing, and thermochemical evolution along strike to Langtang (which would indicate

whether results from one area of an orogen are likely to be representative of the orogen as

a whole), the pressure-temperature evolution, age of peak metamorphism, timing of

movement along major Himalayan thrusts, and transport rate of the region will be established.

This work relies heavily on monazite crystallization ages. Monazite [(LREE, Y, Th)PO$_4$] is a common accessory mineral in metapelites (Overstreet, 1967; see also review of Spear and Pyle, 2002), and is a very popular chronometer in metamorphic rocks because of its high U and Th contents, very low initial Pb, and high retentivity of radiogenic Pb (e.g., see summaries of Parrish, 1990; Harrison et al., 2002). A critical step when employing monazite chronology is linking ages to corresponding metamorphic conditions via monazite chemistry. Many geochronologists still fail to make this link, even though numerous studies have shown the petrogenetic and tectonic value of this endeavor (e.g., Pyle and Spear, 1999, 2003; Ferry, 2000; Foster et al., 2000, 2002, 2004; Pyle et al., 2001, 2005; Spear and Pyle, 2002; Wing et al., 2003; Gibson et al., 2004; Kohn and Malloy, 2004; Dahl et al., 2005; Kohn et al., 2004, 2005; Corrie and Kohn, 2008). By investigating these links, monazite ages may be assigned to specific points along the P-T path of a metamorphic assemblage, i.e., reflecting prograde, retrograde, or hydrothermal processes.

4.2 Petrography and Petrology

4.2.1 Mineral Assemblages

Lesser Himalayan Sequence metapelites are generally characterized by the mineral assemblage Qtz + Ms ± Pl ± Bt ± Grt ± Chl, with accessory apatite + tourmaline + zircon ± ilmenite ± allanite (Table 4.1). Two samples from one location contain

chloritoid. LHS rocks that have a higher Ca-content may also contain hornblende and calcite. The foliation in rocks below the Munsiari Thrust is defined primarily by muscovite and chlorite; biotite in these assemblages is fine grained. Further upsection, within 500 m below the MT, and between the MT and MCT, biotite and muscovite define the primary foliation and the mode of prograde chlorite decreases until it disappears from the prograde assemblage altogether.

The mineral assemblage of GHS Formation I pelitic rocks is predominately Qtz + Pl + Bt ± Ms ± Grt, with accessory apatite + tourmaline + zircon ± rutile ± monazite ± staurolite ± xenotime ± epidote (Table 4.2). A few of the more calcic beds may contain hornblende, chlorite, and clinozoisite. Although several samples contain kyanite, AS01-22a is the only sample that contains sillimanite, which is locally developed as fibrous mats along quartz-plagioclase and plagioclase-plagioclase grain boundaries (Figure 4.2). This sillimanite does not appear to be a regional feature. Kaneko (1995) reported similar sillimanite textures in the Modi Khola valley.

The calc-silicates and calcic quartzites from GHS Formation II contain the assemblage Qtz + Pl + Hbl ± Grt ± Ms, with accessory calcite + clinopyroxene + apatite ± titanite ± clinozoisite ± zircon ± potassium feldspar ± epidote. Formation II amphibolites have the assemblage Qtz + Pl + Hbl + Cpx ± Grt ± Chl, with accessory apatite ± titanite ± zircon ± epidote.

4.2.2 Mineral Chemistry

X-ray maps of garnet below the Munsiari Thrust show that major element zoning is smooth and typical of garnet growth (Figures 4.3-4.5). Grossular and spessartine contents decrease from core to rim, whereas almandine and pyrope increase, as expected for prograde garnet growth (Spear et al., 1990). Additionally, these garnets tend to display S-shaped or snowball inclusion textures due to rotation during crystal growth (Figure 4.6). These spiral inclusion trails are suggestive of up to 160° of rotation relative to the matrix schistosity, which consistently indicates top-to-the-SSW shearing (Hodges et al., 1996).

Garnet from rocks within 500 m of the MCT (above and below) retains primary zoning patterns, particularly for calcium (Figure 4.7 and 4.8). Oscillatory zoning of calcium has been observed in garnets near the MCT in the Darondi and Langtang regions of central Nepal (Kohn et al., 2001; Kohn et al., 2005) and was proposed to result from heterogeneous (instead of constant) thrusting and heating along the MCT (Kohn et al., 2005).

Garnet X-ray maps from GHS Formation I samples indicate progressively more diffusional modification structurally upwards. Near the MCT, from GHS Formation 1a, garnet still retains Mn and Mg trends that are consistent with growth zonation (Figure 4.8). Further from the MCT, garnet zoning becomes increasingly relaxed due to diffusion. This is typical in high-grade metamorphic rocks (e.g., Florence and Spear, 1991), and is consistent with that reported from this transect (Kaneko, 1995; Martin et al., 2010) and in the Marsyandi and Langtang regions of central Nepal (Catlos et al., 2001; Kohn et al.,

2004). In Formation 1b, garnet zoning profiles are flat (Figure 4.9), while even higher upsection in Formation 1c, garnets display homogenous zoning in the cores, but have rim zoning that is consistent with resorption and back diffusion during cooling (Florence and Spear, 1991; Figure 4.10).

Plagioclase grains show core-rim zoning with higher-Ca cores and lower-Ca rims (conversely, lower-Na cores and higher-Na rims). This is expected from garnet growth and fractional crystallization, as garnet growth depletes the matrix in Ca (Spear et al., 1990).

4.3 Thermobarometry

Peak temperature and pressure estimates were calculated via exchange reactions and thermodynamic equilibria. The garnet-biotite thermometer of Ferry and Spear (1978) with the Berman (1990) garnet solution model was used for all samples except AS01-41b, in which the garnet-chlorite thermometer of Dickenson and Hewitt (1986; modified in Laird, 1988) was used in conjunction with the Berman (1990) garnet solution model. Depending on the mineral assemblage of the sample, pressures were calculated using the barometer garnet-plagioclase-aluminosilicate-quartz (Koziol and Newton, 1988), garnet-plagioclase-muscovite-biotite (Hoisch, 1990), or garnet-plagioclase-biotite-quartz (Hoisch, 1990). In two samples from the Lesser Himalayan Sequence plagioclase was not found, so only temperature was estimated. Different thermobarometric calibrations may shift the pressures and temperatures reported for each sample by as much as 25°C and 1 kbar, but the major trends are preserved.

4.3.1 Selecting Compositions for Thermobarometry

Appropriate mineral compositions were selected using standard petrologic criteria (e.g., Kohn, 2008) to provide the best estimate of peak metamorphic conditions (Tables 4.3-4.8). Mineral inclusions suitable for thermobarometry are sparse, so directly constraining prior metamorphic assemblages, and their pressures and temperatures, is difficult. Thus, garnet chemistry provides the principal record of evolving P-T conditions. The composition of garnet that most closely preserves peak metamorphic conditions is the composition nearest the rim that was not affected by retrograde reactions. In the LHS, temperatures were sufficiently low that prograde garnet compositions are commonly retained, and compositions at or near the rim were selected. These garnet compositions were combined with compositions of plagioclase (when present), biotite, muscovite, and chlorite (only one sample) near the garnet that appeared to be texturally equilibrated, rather than retrograde products.

In the GHS, however, sufficiently high temperatures were reached that diffusion, retrograde exchange reactions, and/or retrograde net transfer reactions (ReNTRs) either partially or entirely modified the original growth zoning in garnet (e.g., Kohn and Spear, 2000; Catlos et al., 2001; Kohn et al., 2001, 2004). Homogenization of major element zoning in garnet compromises retrieval of prograde pressures and temperatures. Exchange reactions entail exchange between two elements in two minerals without consuming or producing new minerals. For example, Fe-Mg exchange between biotite and garnet during cooling causes biotite to become more Mg-rich and garnet to become more Fe-rich, causing estimated temperatures to be erroneously low. Retrograde net

transfer reactions consume garnet, returning its constituent elements to the matrix; this process can enrich nearby minerals in Fe and Ca, but can also cause Mn (±Fe) to pile up on the garnet rim and back-diffuse towards the core. Garnet has a much greater Fe/Mg ratio than biotite, and dissolution enriches both biotite and garnet rims in Fe (Kohn and Spear, 2000). These retrograde modifications cause garnet zoning patterns to exhibit a increase at the rim in Mn and Fe, and a decrease in Mg. A common method to circumvent this problem is to use the composition of garnet where Mn and Fe/(Fe+Mg) form a trough. That is, the composition nearest the rim that was not affected by retrograde reactions. In some cases where diffusional homogenization has occurred, this location is near the core of the garnet. However, pairing a garnet composition with a nearby biotite composition that has experienced Fe enrichment will cause the estimated temperatures to be too high. Therefore, a correction must be made to the biotite composition to account for Fe enrichment due to garnet dissolution.

Using garnet X-ray maps to estimate the amount of dissolution of the garnet, the amount of Fe enrichment in biotite due to ReNTRs may be estimated, and the biotite compositions subsequently corrected (Kohn and Spear, 2000). In some samples, the correction to the biotite compositions was minor, and equivalent temperatures could be calculated by using compositions from biotite distal to the garnet that were not affected by ReNTRs. In other samples, correction to the biotite compositions lowered estimated temperatures 10 to 50 °C. To calculate P-T conditions in GHS samples, the garnet composition with the lowest Fe/(Fe+Mg) and Mn were chosen and combined with

corrected or distal biotite (depending on the sample), proximal muscovite, and rim

compositions of proximal plagioclase.

Evidence to support the estimated P-T conditions includes agreement with the

stability of observed mineral assemblages and consistency with P-T conditions of nearby

samples that have different compositions.

4.3.2 Estimated P-T Conditions

Rocks from the Modi Khola valley show chemical and textural evidence for only

one episode of metamorphism, and display the familiar apparent inverted metamorphism

associated with the Main Central Thrust. Mineral isograds increase progressively from

biotite and garnet in the LHS up to at least kyanite in the GHS. Below the Munsiari

Thrust in the LHS, rocks experienced peak metamorphic conditions of about 515 °C and

7.5 kbar (Table 4.9, Figure 4.11). Within the Munsiari Thrust sheet, pressures and

temperatures were about 555 °C and 10.5 kbar. Peak pressure and temperature conditions

increase across the MCT (Figs. 4.12 and 4.13) where, at the base of the thrust sheet, P-T

conditions are 650 °C and 12.0 kbar, similar to data reported from the hanging wall of the

MCT in the Annapurna region (Kaneko, 1995) and in the Marsyandi, Darondi and

Langtang regions of central Nepal (Catlos et al., 2001; Kohn et al., 2001, 2004; Kohn,

2008), though much lower than the P-T conditions reported by Martin et al. (2010) for

the same transect (Figure 4.14). Temperatures increase systematically upsection away

from the MCT, to 735 °C and 12.5 kbar in the middle of Formation I (Fm. 1b) to 775 °C

and 12.5 kbar at the top of Formation I (Fm. 1c). These P-T conditions accord with those

of Martin et al. (2010), as do those from Formation II, which we estimate to be ~ 775

°C and 14.0 kbar.

4.4 Monazite

4.4.1 Monazite Petrogenesis

Monazite is a common accessory in metapelitic GHS rocks and is typically zoned

in Thorium (Th) and Yttrium (Y). As previously mentioned, variations in these elements

are often associated with reactions among the major silicates. As monazite grows, it

preferentially fractionates Th, progressively depleting the matrix, and resulting in earlier

vs. later grown monazite having higher vs. lower Th contents (Kohn and Malloy, 2004).

Allanite also hosts Th, and though allanite is the primary LREE-accessory phase in the

LHS, it was found in only one GHS rock – a quartzite with a high-calcium bulk

composition. Monazite also sequesters Y into its structure, but so do other minerals

including garnet, allanite, and xenotime (Spear and Pyle, 2002), potentially complicating

interpretation of Y systematics. No evidence exists for prograde allanite or xenotime in

any of the monazite-bearing GHS rocks. Garnet x-ray maps of Y do not indicate growth

in the presence of xenotime, though a few samples contain minor retrograde (?) xenotime

that is texturally associated with monazite rims. Yttrium systematics in most samples thus

depend principally on the interplay between garnet and monazite (Pyle and Spear, 1999,

2003; Pyle et al., 2001). During prograde growth, Y is incorporated into garnet, so

concentrations of Y in monazite should decrease with progressively higher grade. This

simple trend changes during partial melting (normally via muscovite dehydration-

melting), where monazite begins to dissolve, erasing direct chemical or chronological evidence of peak metamorphic temperatures. However, this reaction liberates Y to the melt (Spear and Pyle, 2002), where, upon cooling and melt crystallization, it is incorporated in relatively high concentrations in re-growing monazite. Thus, post-anatectic rims of monazite should be chemically distinct (high-Y and possibly high-Th) from monazite that grew along the prograde path (e.g., Kohn et al., 2005). That is, Th and Y systematics in monazite allow specific zones and ages to be chemically correlated within P-T space (Kohn et al., 2005).

4.4.2 Monazite Chemistry and Th-Pb Geochronology

Tables 4.10 and 4.11 list compositions of Himalayan monazites from two GHS rocks (corresponding to spot analysis locations in Figure 4.15). ThO_2 and Y_2O_3 concentrations ranges from 3.2-8.1 wt% and 0.5-2.8 wt%, respectively. Most GHS monazite grains show substantial Y and Th zoning. As expected due to Th fractionation, grains from several samples display a rimward decrease in Th. Many grains exhibit low-Y cores and higher-Y rims, but a number of samples contain grains that have either a relatively homogenous Y distribution or a mottled Y-zoning pattern that shows no distinct Y zones, but is not homogenous. These different zones were targeted for *in situ* ion probe analysis to chemically link (wherever possible) each zone and its corresponding age.

Monazite from GHS Formation 1a contains mottled Y and Th zoning and no distinct high-Y rims that would indicate partial melting, which is in agreement with

calculated sub-anatectic P-T conditions for those samples (Figure 4.16, Table 4.12). The 21-25 Ma ages from these grains are thus considered to represent prograde metamorphism. One monazite from sample AS01-15b contains evidence for an inherited component, with a low Y and Th core and anomalously old, probably mixed ages that are not interpretable within the context of the Indo-Asian collision.

Formation 1b monazite either displays distinct low-Y cores and high-Y rims, or an indistinct zoning that is nevertheless geochronologically inhomogeneous (Figure 4.17, Table 4.12). Low-Y, prograde core ages are 24-29 Ma, though one monazite from AS01-16a has an age of 33 Ma, presumably the result of early prograde nucleation and growth. High-Y rim cooling ages are 17-22 Ma. Sample AS01-17b does not show signs of multiple episode of growth, as it does not contain well-defined cores with overgrowth rims. Rather, these monazites have slightly high Th cores, rimward Th decreases, and a relatively flat distribution of Y. However, the monazites are small, high-Y, and exhibit relatively young ages (~18 Ma), and so are interpreted to have entirely grown during post-anatectic cooling.

Monazite in samples from Formation 1c generally have low-Y cores and high-Y rims, the product of prograde growth and post-anatectic cooling, respectively (Figure 4.18, Table 4.12). One grain from sample AS01-32 contains mottled zoning and slightly older ages, representing early prograde growth. Post-anatectic cooling and monazite growth occurred 19-15 Ma, as indicated by high-Y rims or small homogenous high-Y monazites with ages coincident with rim ages.

Monazite from GHS Formation III, just below the South Tibetan Detachment, exhibits either a mottled zoning pattern, or slightly higher-Th cores that decrease rimward. There is no evidence for rim growth associated with cooling after melting (Figure 4.19, Table 4.12). Higher Th zones in the monazite are 35-38 Ma and are ascribed to early prograde growth with later prograde growth represented by 30-35 Ma mottled Y and Th zones.

4.4.3 Monazite Age Distribution

Four generations of monazite have been identified in samples south of the Annapurna range along the Modi Khola in central Nepal. From oldest to youngest they are: inherited, early prograde, late prograde, and post-anatectic, and can be distinguished chemically and/or chronologically.

Age probability diagrams for monazite (Figure 4.20) show distinct peaks that correspond to specific chemistries, and thus to petrologic origins. Geochronologic analyses that clearly contained mixed zones (i.e., the ion probe spot covers two distinctly separate zones in the monazite) were not used in the age profile calculations. Particularly significant is the timing of the last growth of prograde monazite (youngest low Y and Th peak) versus the first instance of melt crystallization during cooling (high-Y overgrowth). Together, these ages bracket the timing of anatexis. Additionally, the diagrams demonstrate decreasing temperatures and ages of metamorphism structurally downward, consistent with progressive underthrusting of tectonic slices. In the structurally highest rocks of the Formation III orthogneiss, the last prograde monazites that formed have an

age of 30-33 Ma. Structurally lower in the next highest unit, Formation 1c, the latest

prograde sub-solidus monazite formed 27-30 Ma (3 Ma younger than Fm. III), with

crystallization of *in situ* melts 19-22 Ma. Peak-T metamorphism and anatexis thus

probably occurred ~25 ± 2 Ma in Formation 1c. Structurally lower rocks have the same

chemically defined generations of monazite, but again displaced to younger ages and

lower temperatures. Ages from Formation 1b imply melting at 23 ± 1 Ma, with post-

anatectic monazite growth from 22 to 17 Ma. This means that both packages of rocks

(Formations 1b and 1c) underwent similar reactions (specifically muscovite dehydration

melting and ensuing melt crystallization), but at different times. Monazite in Formation

1a experienced sub-solidus growth from 21-16 Ma.

4.5 Discussion

Due to the observed chronologic and thermobarometric differences between GHS

rock units in the Annapurna region, two thrusts are identified within GHS Formation I:

the Bhanuwa Thrust (BT; between Formations 1a and 1b), and the Sinuwa Thrust (ST;

between Formations 1b and 1c; Figure 4.1). The Sinuwa Thrust is inferred to place high-

T, pervasively migmatitic rocks of GHS Formation 1c atop slightly lower-T locally

migmatitic rocks of Formation 1b. Based on monazite geochronology (Figure 4.20),

initial melts may have formed in the Sinuwa thrust sheet (Formation 1c) as early as 27

Ma, but not until 23 Ma in the Bhanuwa thrust sheet (Figure 4.21). The large gap

between pre- and post-anatectic monazite in the Sinuwa thrust sheet precludes

pinpointing the timing of initial cooling. Possibly cooling commenced as early as 25-26

Ma, during heating of the Bhanuwa thrust sheet, implying emplacement of the ST at that time. Alternatively, the ST and BT rocks may have been buffered at anatectic conditions until cooling and melt crystallization in both sheets at ~22 Ma. From this point on, the two sheets probably experienced similar cooling histories as they were transported together in the hanging wall of the Bhanuwa Thrust. Presuming that cooling resulted primarily from thrust emplacement (Kohn et al., 2004; Kohn, 2008) rather than from erosion or vertical displacement, these data imply initial ST movement some time between 22 and 27 Ma, and initial BT movement at 22 Ma.

A fault between GHS Formations 1a and 1b was first identified by Martin et al. (2010) as a normal fault based upon a 4 kbar pressure difference between hanging wall and footwall rocks, shorter retrograde chemical profiles in garnet in footwall rocks, and the presence of kyanite in the hanging wall vs. its absence in the footwall. P-T data from this study do not support such a disparity in the pressures across the fault. Instead, our data indicate very little increase in pressure structurally upward, but ~85 °C increase in temperature (Table 4.9). This temperature increase can account for the presence of kyanite and longer retrograde diffusion profiles in the hanging wall vs. the footwall. P-T calculations and monazite geochronology do, however, support the presence of a fault in this location. Thus, we revise the interpretation of the Bhanuwa Fault from a normal fault to a thrust. Monazite data from the Bhanuwa thrust sheet and the structurally lower Formation 1a rocks in the MCT thrust sheet support the estimated P-T conditions in both packages. Temperatures in the Bhanuwa thrust sheet were high enough that partial melting would be expected via the muscovite dehydration reaction, and high-Y rims on

monazite due to post-anatectic cooling and crystallization confirm this. Underneath, in the MCT thrust sheet, peak temperatures were ~650 °C (Table 4.9), below partial melting temperatures, and monazite in these rocks does not contain evidence that they experienced melting and post-anatectic growth (Figure 4.16).

As noted by Viskupic and Hodges (2001), Harrison et al. (2002), and Kohn et al. (2005), there are some significant interpretational uncertainties for most published Greater Himalayan Sequence monazite ages. Recent work has shown that there can be three to five different generations of monazite of varying age and chemical compositions that can encompass over 20 million years of Himalayan metamorphism (Kohn et al., 2005; this study). A single age from a bulk analysis, single grain, or even grain fragment analyzed via ID-TIMS (e.g., Hodges et al., 1996; Coleman, 1998; Simpson et al., 2000; Godin et al., 2001; Johnson et al., 2001) may be a real age, but it could also be a geologically meaningless mix of inherited components, prograde and retrograde growth domains, and late-stage alteration (Harrison et al., 2002; Kohn et al., 2005).

Other monazite Th-Pb ion probe ages have been published from along the Marsyandi River valley, approximately 100 km east of the Annapurna transect (Catlos et al., 2001). However, the spot locations for the ages were presented without chemical context. That is, it is unclear whether the ages are collected from cores or rims, high-Y or low-Y domains, or even if the spot location overlapped two distinct chemical or chronological zones, thus rendering that age geologically meaningless. Probability distributions of these data generally show a range in ages that spans the entire course of Himalayan metamorphism (Figure 4.21). The age distribution from Formation 1b in the

Marsyandi valley could, in principle, reflect a similar cooling history to Formation 1b in the Annapurna region (i.e., 17-20 Ma), assuming those ages are from high-Y, post-anatectic rim domains and not cores. That is, monazite ages from the Marsyandi region show no overall disagreement with the data presented in this study, but are not especially diagnostic of the timing of thrust movement.

Combining thermobarometric and geochronologic data allows rates of thrusting to be calculated (e.g., Kohn et al., 2004). These calculations require that cooling in the hanging wall results from thrust juxtaposition against cold footwall rocks, rather than from erosion or displacement with a significant vertical component. This assumption is consistent with original shallow thrust orientations (DeCelles et al., 2001), allowing these faults to accommodate significant convergence at depth (30-40 km depth; Figure 4.22). Barometric estimates of footwall and hanging wall rocks are not so different that vertical exhumation due to erosion or vertical transport could have been the primary means of cooling. In addition, where the Main Himalayan Thrust is at those depths, modern erosion directly above is <2 mm/yr (Lavé and Avouac, 2001). The other assumption is that among the Sinuwa, Bhanuwa, and Main Central Thrusts, only one thrust may be active at any given time. This is problematic (see below), but allows for limits to be placed on the slip rate along fault surfaces.

Thrust rates were calculated using the method of Kohn et al. (2004). The minimum amount of cooling during fault slip was approximated based on the peak temperatures in the hanging wall and those in the footwall. Thermal models for the central Himalaya (Henry et al., 1997; Huerta et al., 1999) define temperature-depth

distributions on which peak P-T data may be plotted, and allow ΔT's of cooling to be converted into thrust distances (Figure 4.22, Table 4.13). Effectively, thermal models define lateral thermal gradients, from which ΔT's are converted to displacements. Peak metamorphic ages from monazite in different thrust sheets provide a maximum duration of thrust displacement. The thrust rate is thus derived from the displacement distance over the time period of displacement.

In reality, uncertainties in peak temperature and chronology propagate to large errors for estimates for the Sinuwa and Bhanuwa thrust rates. Thus we mostly consider our results in terms of evaluating consistency (or not) with a nominal 2 cm/yr Himalayan convergence rate. For the MCT sheet, the cooling rate is more precise, but because pressures appear slightly higher than in the underlying MT sheet, some component of vertical cooling must be considered. A maximum pressure difference of 3 kbar (10 km), and typical Himalayan thermal models (e.g., Royden, 1993; Henry et al., 1997; Harrison et al., 1998; Huerta et al., 1998, 1999; Beaumont et al., 2001, 2004; Jamieson et al., 2002, 2004), imply that up to 50 °C of MCT sheet cooling could be ascribed to vertical rather than lateral displacement. This leaves at minimum 200 (±30) °C of cooling to be explained by lateral transport.

The calculated slip rates for the Sinuwa, Bhanuwa, and Main Central Thrusts are 0.5 to 2.3 cm/yr at 23 to 27 Ma (ST), 0.8 to 3.2 cm/yr at 19 to 23 Ma (BT), and 1.4 to 2.4 cm/yr at 15 to 22 Ma (MCT; Figure 4.22, Table 4.13). These calculations show P-T-t consistency with a 2 cm/yr convergence rate component across the Himalaya from ~25 to ~15 Ma. These results support models that presume constant rates since at least 25 Ma

(Royden, 1993; Henry et al., 1997; Harrison et al., 1998; Huerta et al., 1998, 1999; Beaumont et al., 2001, 2004; Jamieson et al., 2002, 2004).

The similarity in inferred peak ages for the ST, BT, and MCT could in principle indicate simultaneous initial cooling of all three sheets at ~22 Ma (Figure 4.23 model 2). Because pressures appear to increase structurally upward slightly, such cooling is unlikely to occur in a single thrust with an inverted thermal gradient. Rather, a simpler explanation would involve transport and cooling of each rock package along the same basal thrust (the MCT), and later juxtaposition of already-cooled rocks along the ST and BT. That is, this model implicitly requires as much as 100 km of out-of-sequence thrusting. Whereas we cannot rule out this possibility on the basis of P-T-t data alone, we note that such large out-of-sequence thrusts have not yet been reported elsewhere in the Himalaya.

Geochemically similar generations of monazite occur at both Langtang and Annapurna (i.e., early prograde mottled zoning, late prograde low Y, and post-anatectic high-Y rims), but monazite ages along the Modi Khola appear older by ~5 Myr compared to Langtang. The MCT sheet at Langtang records late prograde monazite growth 16-23 Ma and post-anatectic cooling 13-16 Ma (Kohn et al., 2005), while MCT rocks at Annapurna record late prograde monazite growth 21-23 Ma and cooling 16-20 Ma. By comparison, rocks in the Langtang Thrust (LT) sheet at Langtang record late prograde monazite growth 22-23 Ma and cooling 17-19 Ma (Kohn et al., 2005). This could potentially indicate that the MCT at Annapurna is temporally equivalent to the LT at Langtang.

One explanation for the observed geochronological differences between the MCT at Annapurna and Langtang is the presence of a lateral ramp along strike (Figure 4.24, t_1). That is, the thrust plane cuts up section from west to east. Alternatively, the LT and MCT shear zones could have died out laterally (Figure 4.24, t_1). Because each thrust surface represents the accumulation of strain over millions of years, and because thrust surfaces may have shifted differently in different areas, the present-day distribution of lithologic packages (GHS Fm 1a, 1b, 1c, LHS, etc.) may not uniquely elucidate thrust evolution. That is, the MCT surface is defined on lithologic, not chronologic, criteria and juxtaposition of GHS and LHS rocks may have been diachronous along strike.

Assuming that the MCT at Annapurna and the LT at Langtang were active at the same time (Figure 4.24, t_1), the sequence of thrusting could have followed a number of progressions to obtain their current geometry. One possibility is that the thrust plane consistently cut upsection between Annapurna and Langtang, connected by a lateral ramp (Figure 4.24, t_2a), so that the thrust surfaces followed a sequence of progressive under-thrusting in both regions. This is consistent with the BT and ST in Annapurna being older structures than the LT in Langtang, presuming that the MT in the Annapurna region would be of similar age to the MCT at Langtang. A similar model suggests the same progression down to the MCT, but protracted MCT transport at Annapurna coincident with movement at Langtang (Figure 2.24, t_2b). Yet another alternative suggests concurrent movement of the MCT at Annapurna and LT at Langtang along non-continual thrust planes, and the initiation of a lateral ramp cutting down-section 16-17 Ma that

would juxtapose already cooled BT and ST sheets coeval with initial movement along the MCT at Langtang (Figure 2.24, t_2c).

As stated before, such large-scale diachroneity or out-of-sequence thrusting has not been reported before in the Himalaya, however our ability to resolve geological events has only recently progressed to the point that allows us to look at strain partitioning over million year timescales and potentially distinguish previously unrecognized spatial and temporal heterogeneity. The data show a complexity that does not lead to a concrete answer, but nonetheless, indicates that more work examining differences in strain partitioning on million-year or smaller timescales might elucidate previously unrecognized variabilities.

Despite differences in absolute ages, the similarities among the chemical systematics of monazite, peak P-T conditions, and thrust rates calculated for Langtang and Annapurna do, however, imply that strain measurements in one part of an orogen can be realistically extrapolated to another within a few hundred kilometers, although the timing of movement on discrete thrust surfaces may differ. This lateral predictability may only hold for geologically similar regions of the orogenic belt. With distance may come a change in boundary conditions (like rotation at the syntaxes) that would prevent long-distance extrapolation of strain estimates. Additional measurements from other parts of the orogen in India and Bhutan would be needed to verify whether these estimates could be applied to the orogen as a whole.
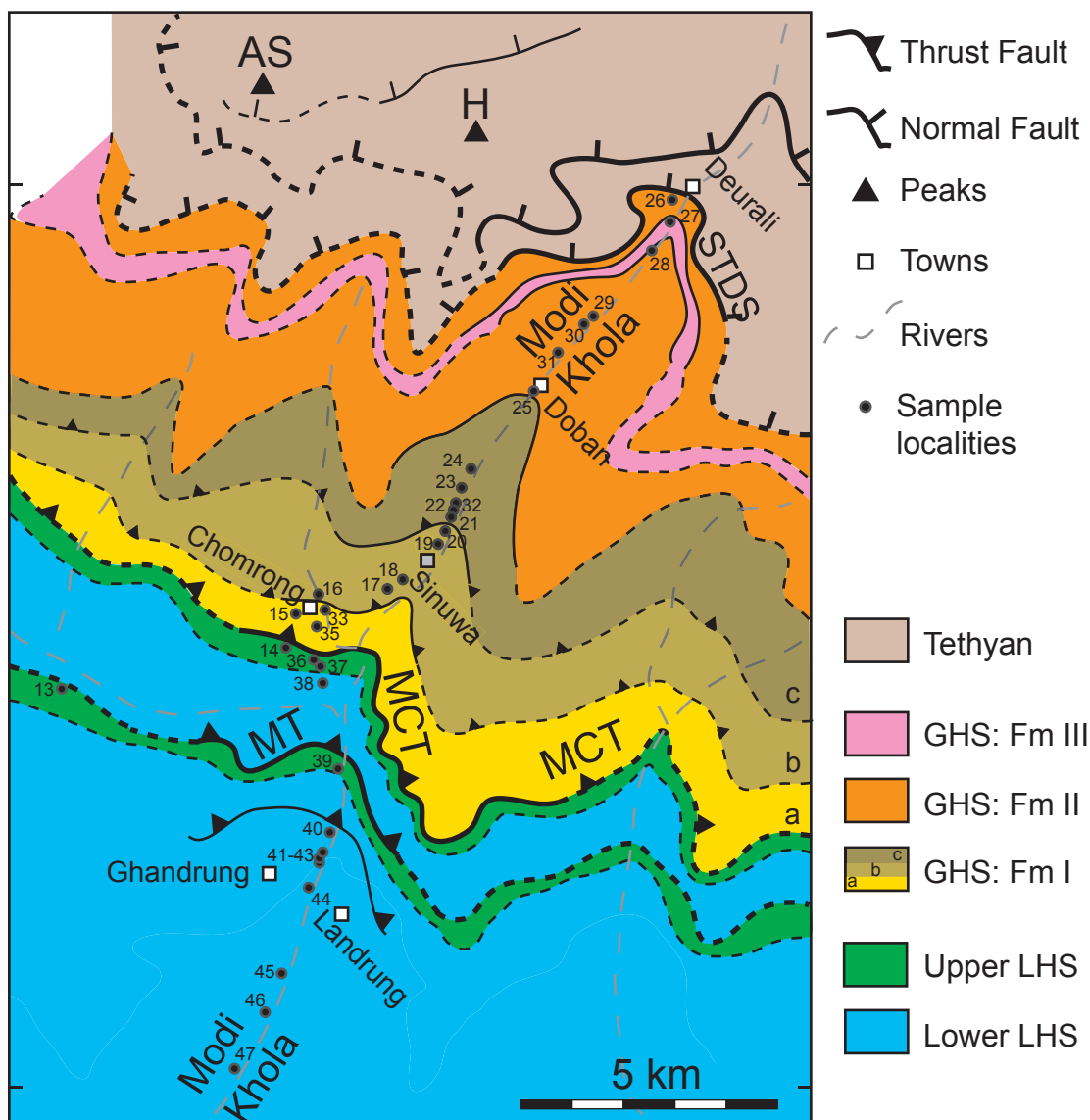
Figure 4.1. Geologic map of the Annapurna region along the Modi Khola. Geology after Colchen et al. (1986), Hodges et al. (1996), Pearson and DeCelles (2005), and Martin et al. (2007). Numbers for sample locations follow the pattern AS01-X. Barbed lines represent thrust faults: MT = Munsiari Thrust, MCT = Main Central Thrust, BT = Bhanuwa Thrust, ST = Sinuwa Thrust. Single dashed lines are normal faults: STDS = South Tibetan Detachment system. Labeled squares indicate towns. Black triangles are peaks: AS = Annapurna South, H = Hiunchuli.
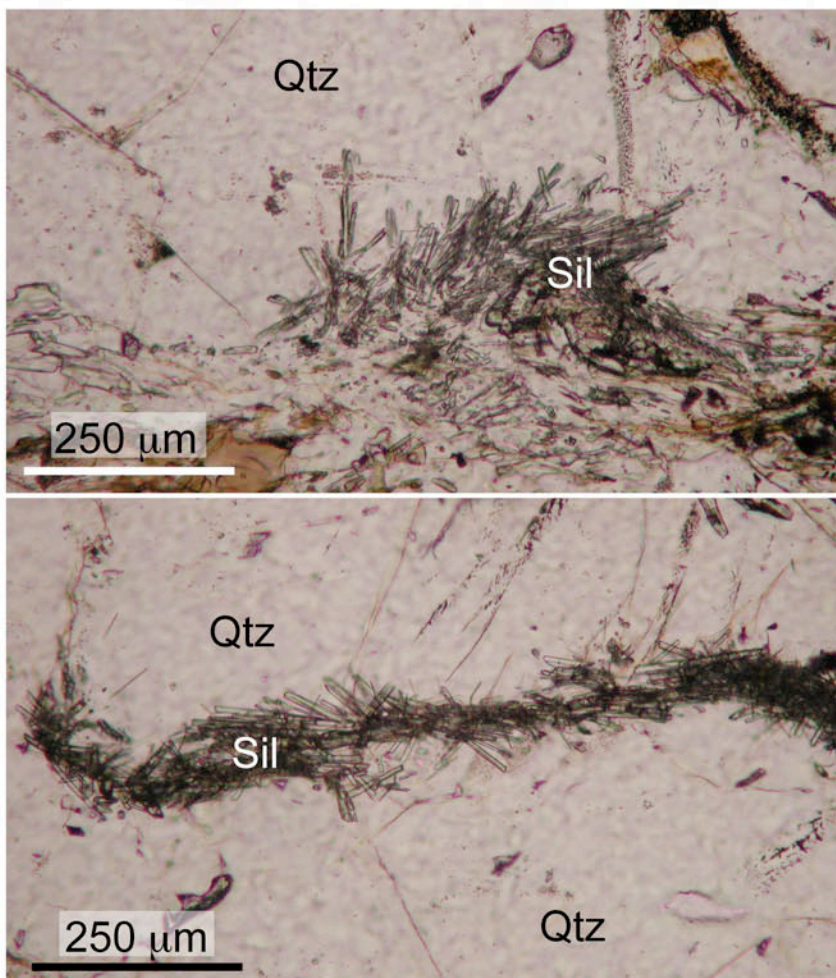
Figure 4.2 Photomicrograph of fibrolitic sillimanite from
sample AS01-22a. Image taken under plane-polarized light.
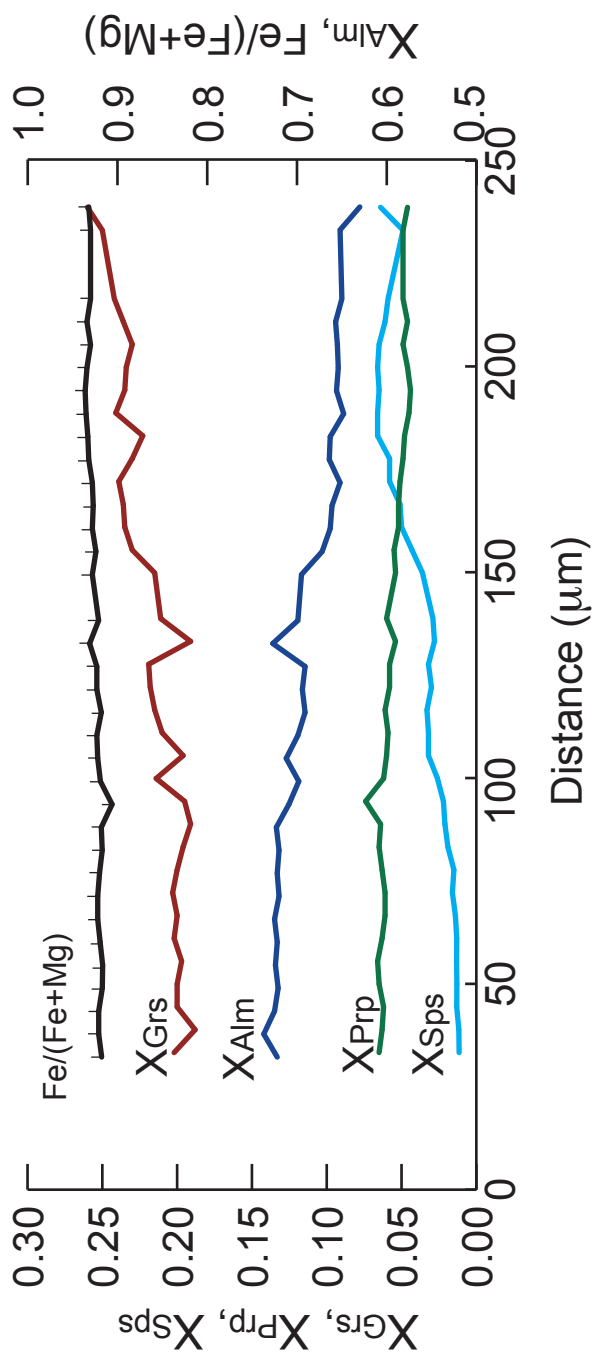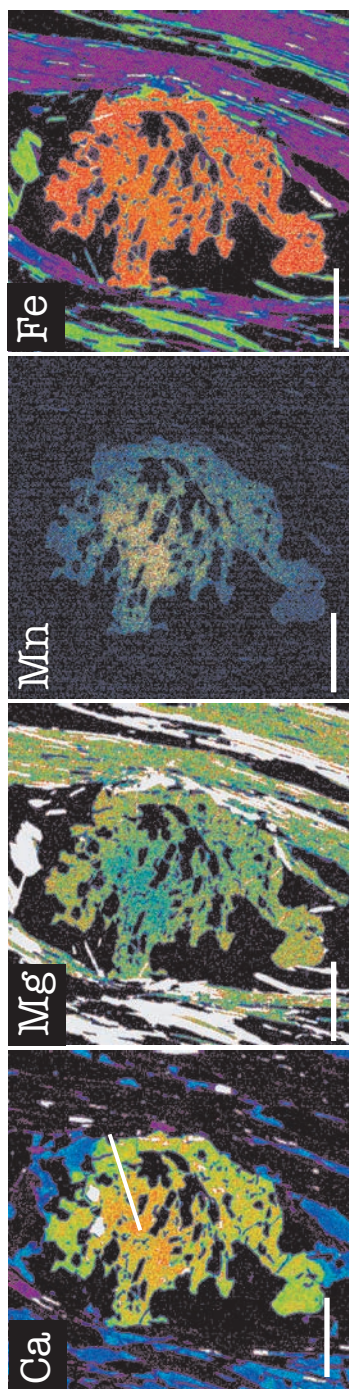
Figure 4.3. Lesser Himalayan Sequence AS01-38b garnet. White line is traverse across garnet from rim to core. Vertical tick marks on Fe/(Fe+Mg) indicate analysis points. Scale bars 200 microns.
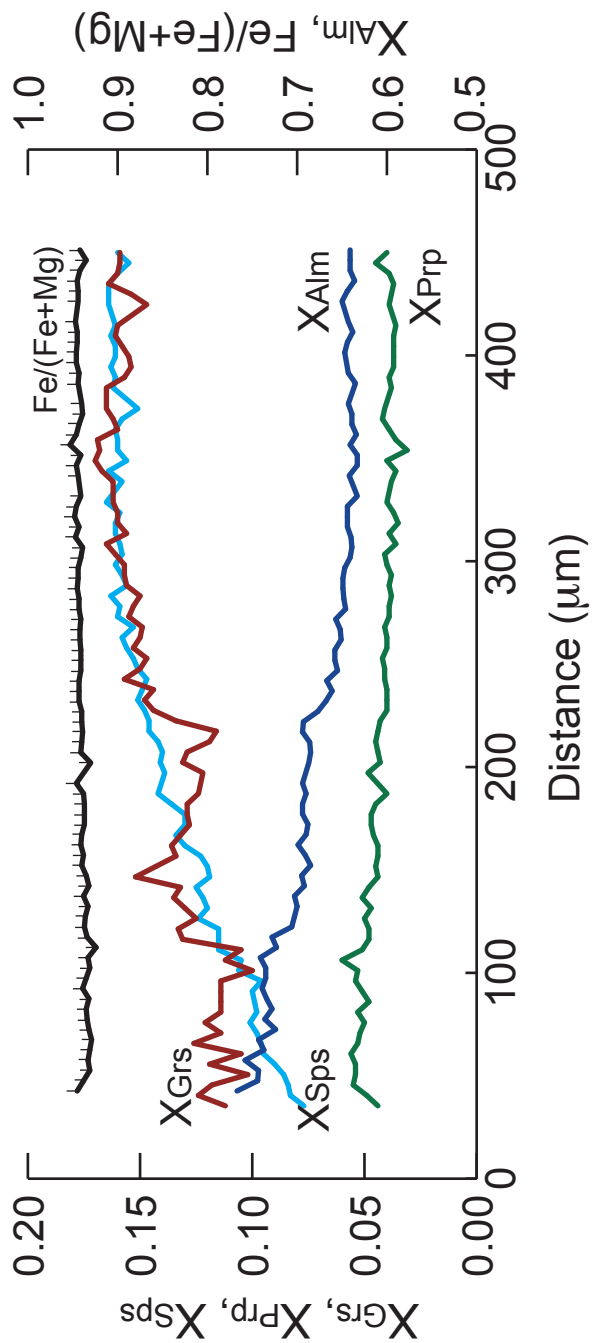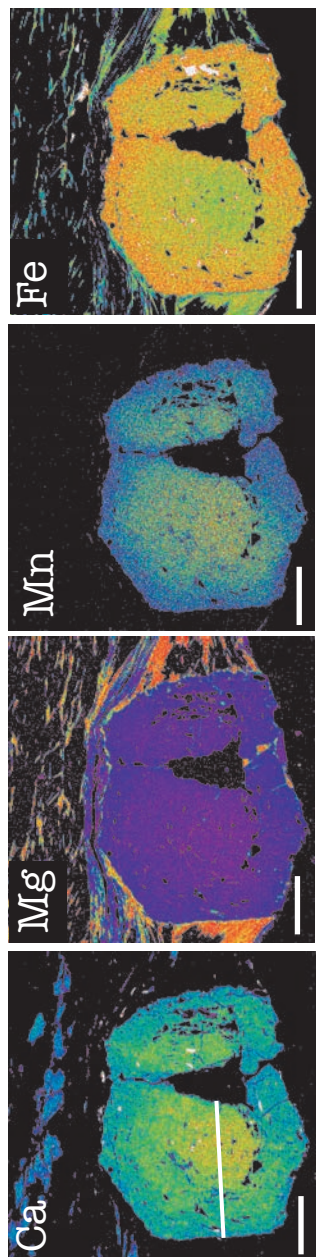
Figure 4.4. Lesser Himalayan Sequence AS01-40e garnet. White line is traverse across garnet from rim to core. Vertical tick marks on Fe/(Fe+Mg) indicate analysis points. Scale bars 200 microns.
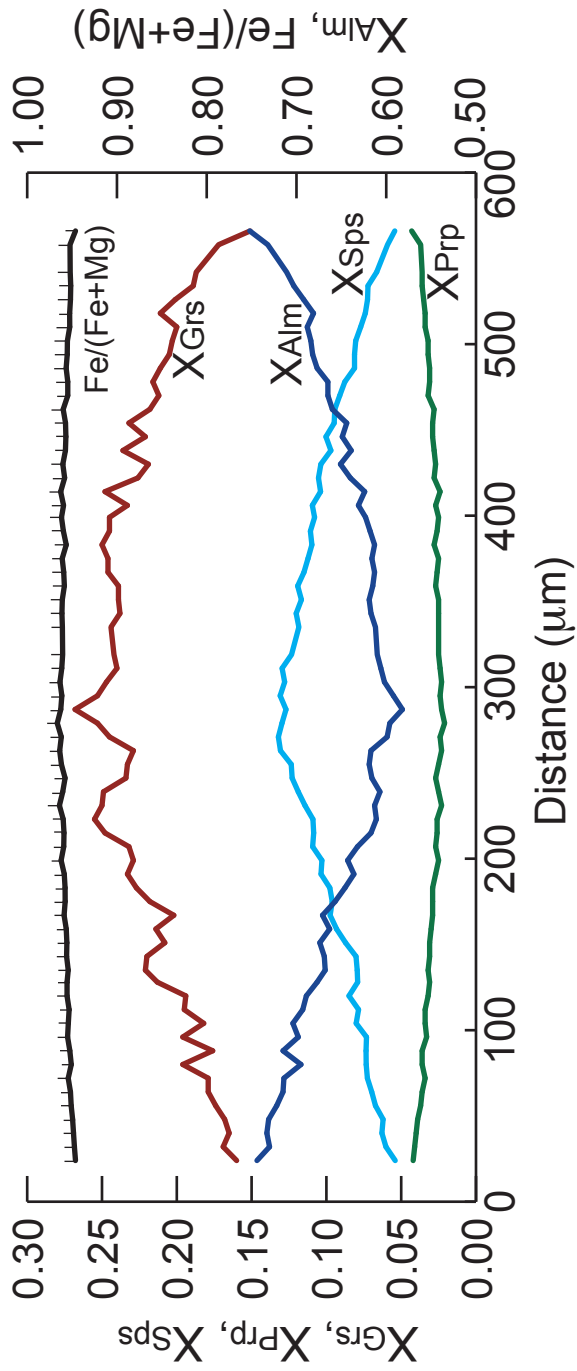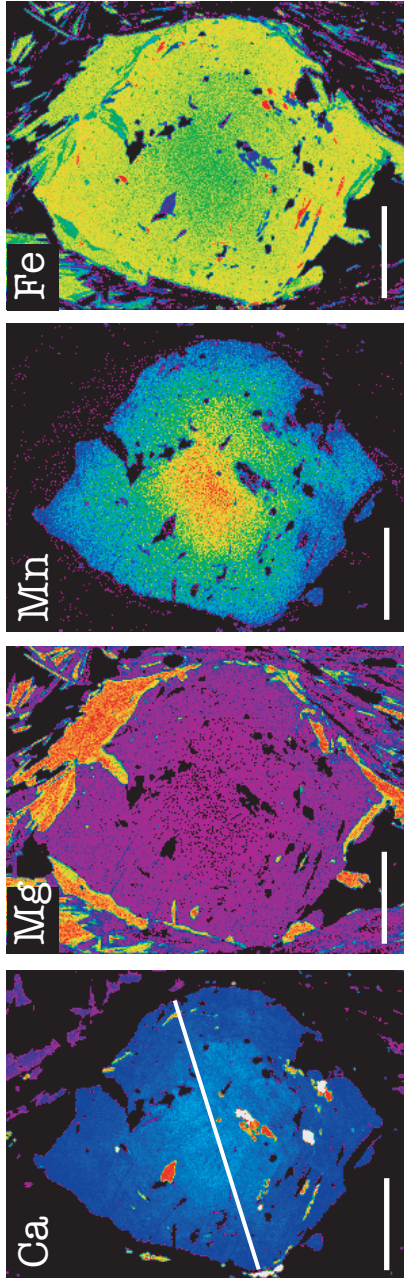
Figure 4.5. Lesser Himalayan Sequence AS01-46 garnet. White line is traverse across garnet from left to right. Vertical tick marks on Fe/(Fe+Mg) indicate analysis points. Scale bars 200 microns.
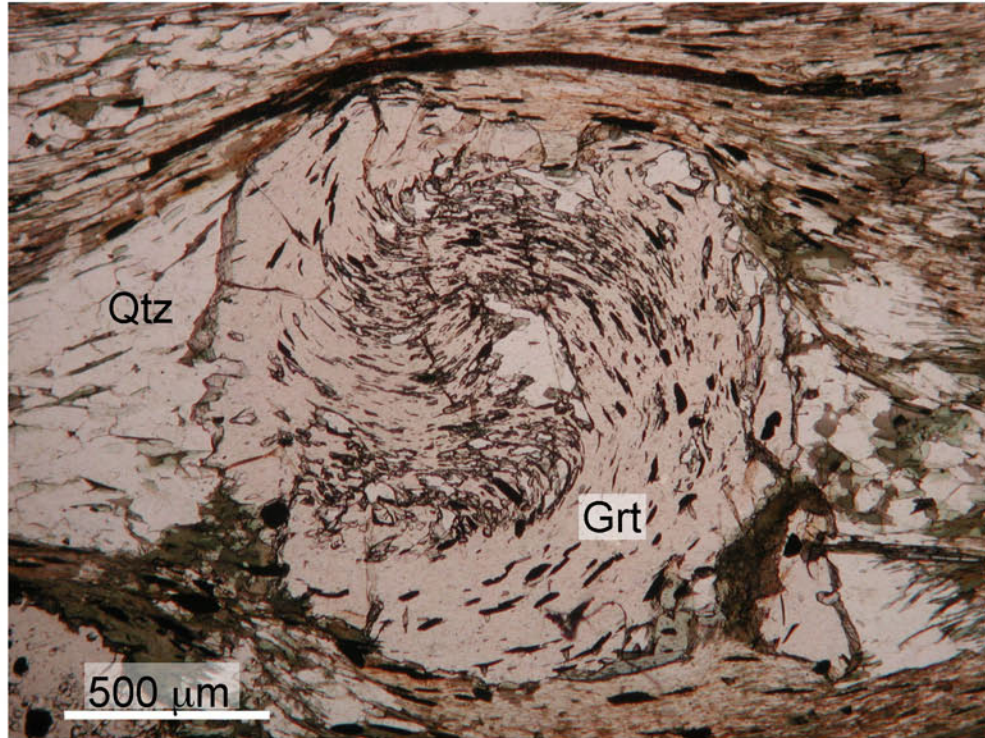
Figure 4.6. Garnet photomicrograph from sample AS01-41b exhibiting snowball inclusion textures due to rotation during crystal growth. Photomicrograph taken under plane-polarized light.
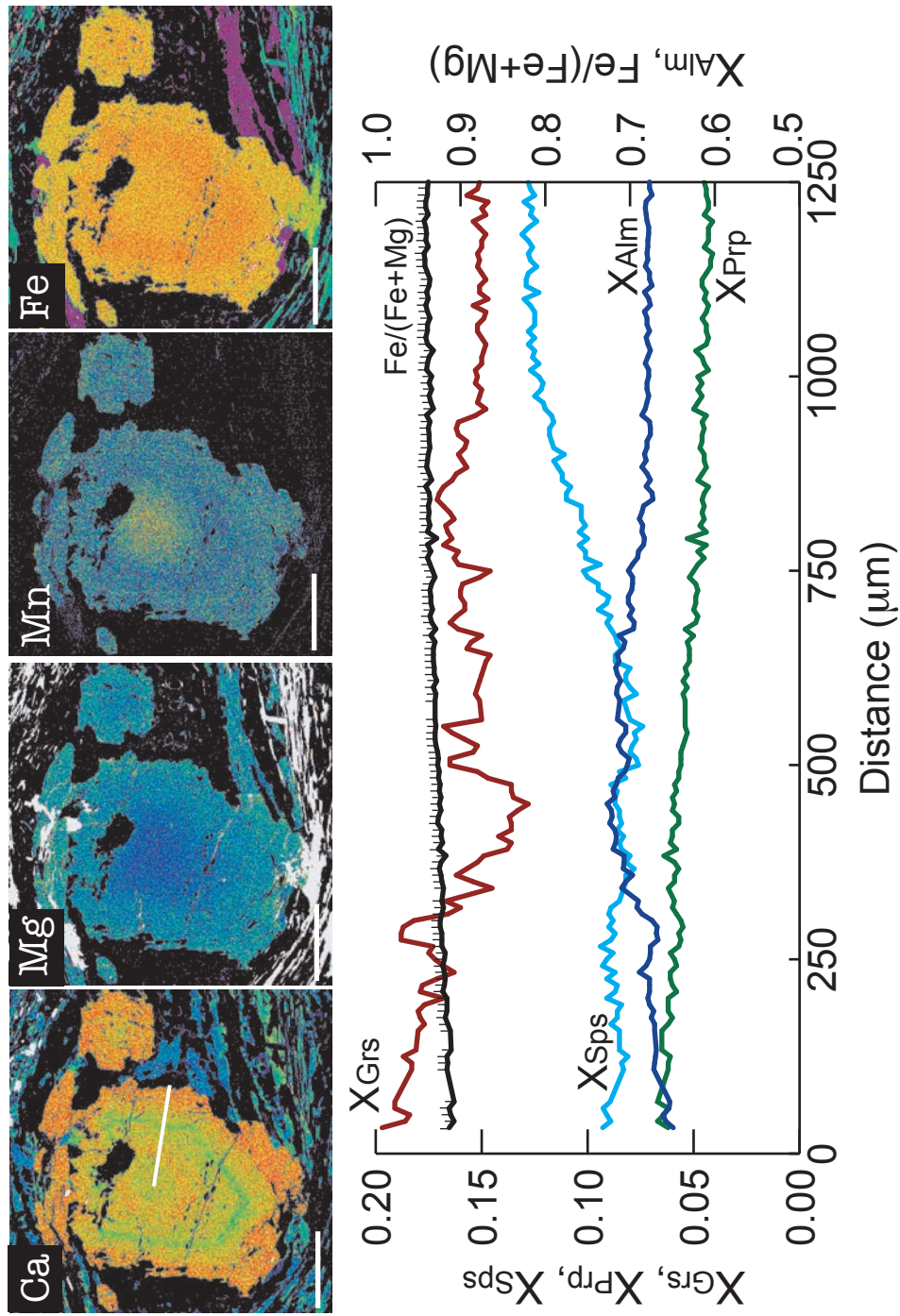
Figure 4.7. Lesser Himalayan Sequence AS01-36a garnet. White line is traverse across garnet from rim to core. Scale bars 1 mm. Vertical tic marks on Fe/(Fe+Mg) indicate analysis points.

Note oscillations and compositional reversal for Ca and Mn.
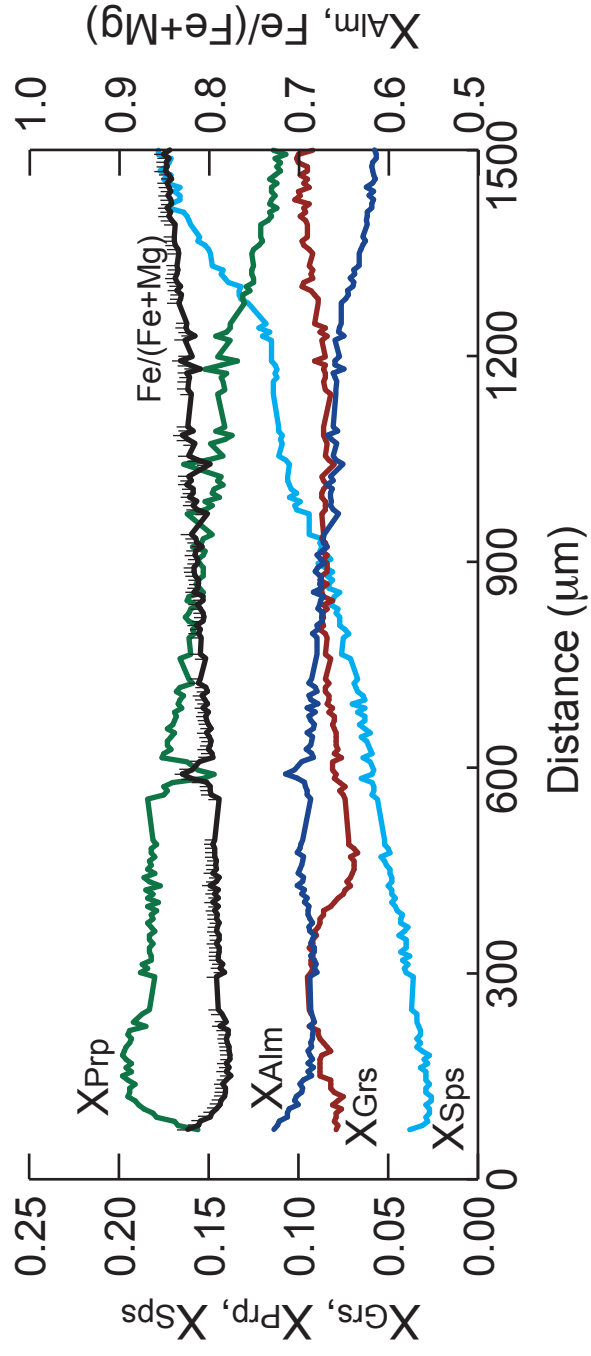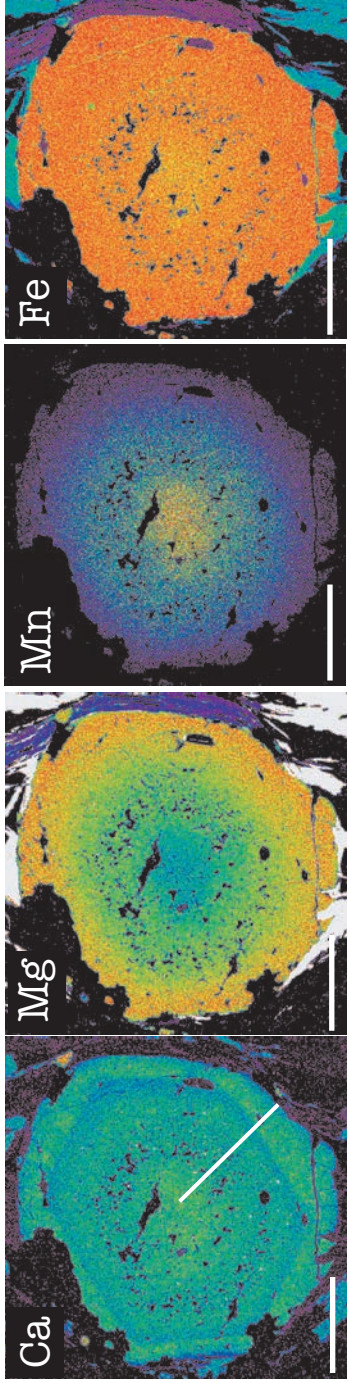
Figure 4.8. Greater Himalayan Sequence AS01-15c garnet. White line is traverse across garnet from rim to core. Vertical tick marks on Fe/(Fe+Mg) indicate analysis points. Scale bars 1 mm.
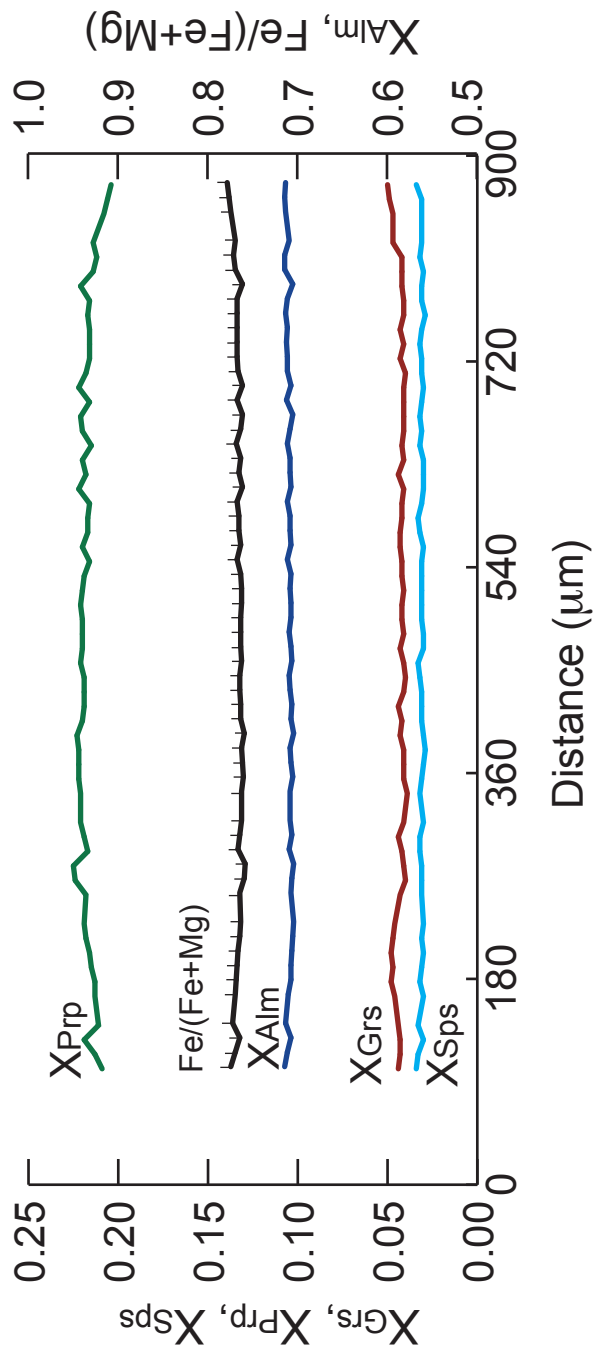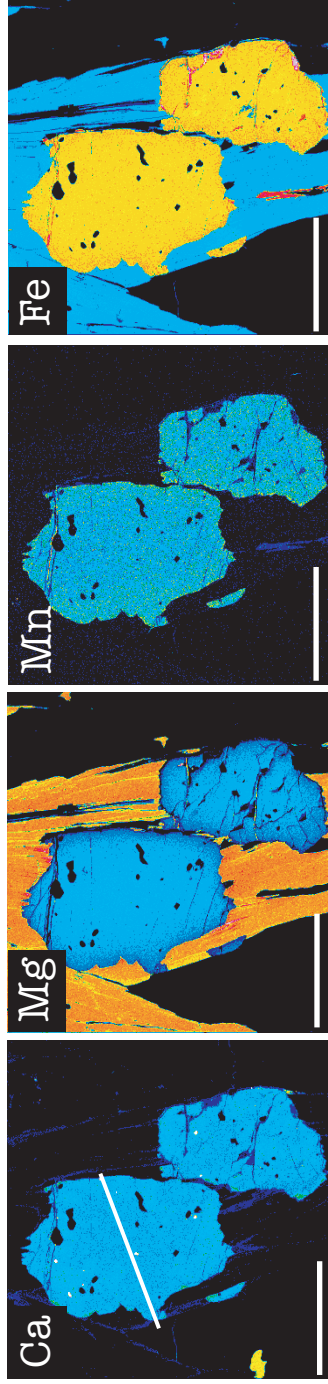
Figure 4.9. Greater Himalayan Sequence AS01-18d garnet. White line is traverse across garnet from left to right. Vertical tick marks on Fe/(Fe+Mg) indicate analysis points. Scale bars 500 microns.
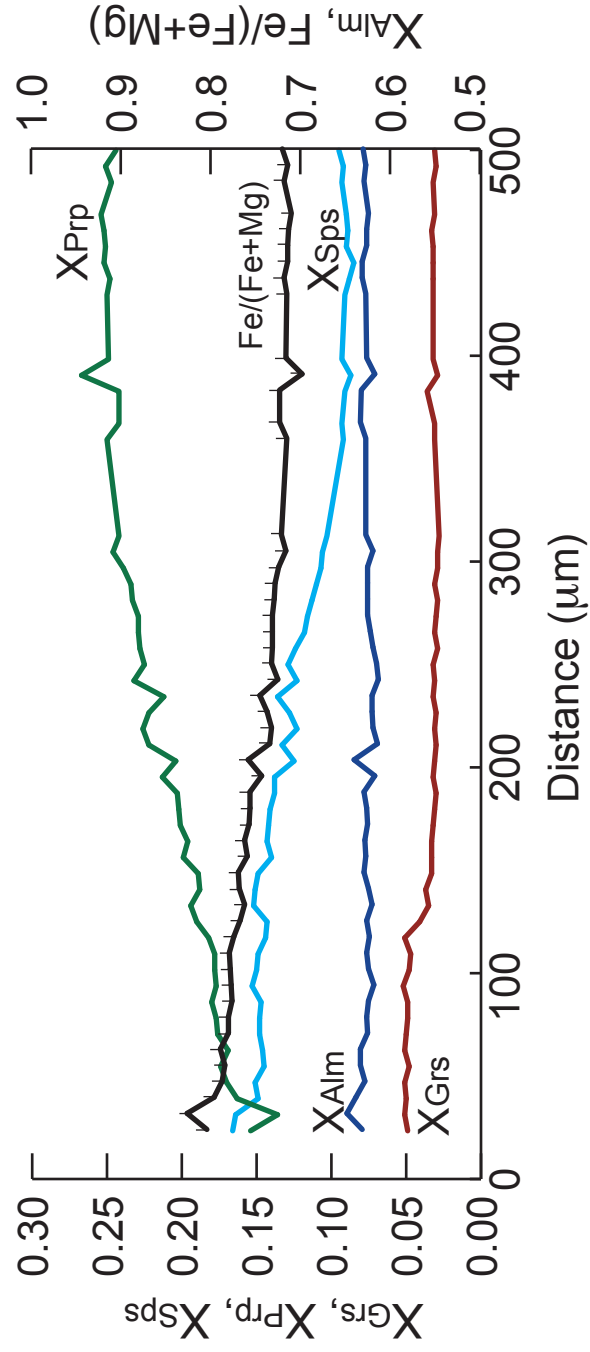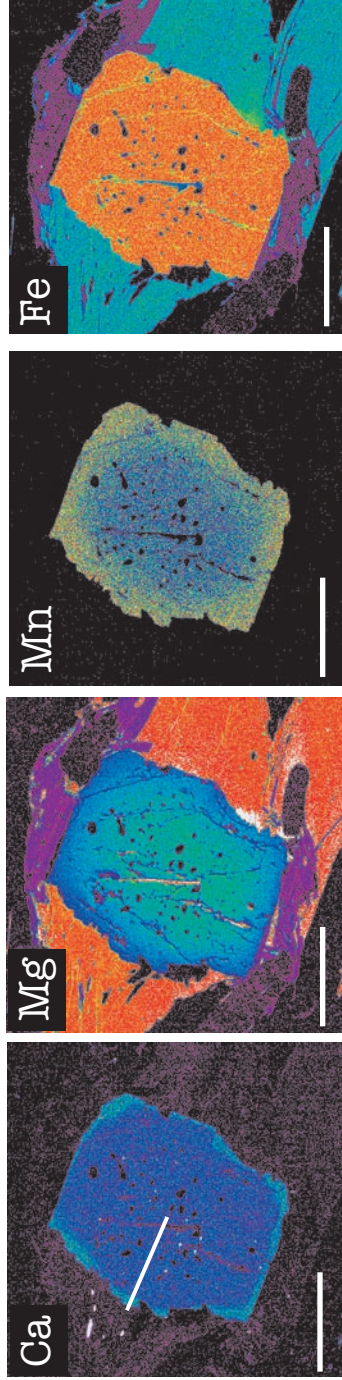
Figure 4.10. Greater Himalayan Sequence AS01-22a garnet. White line is traverse across garnet from rim to core. Vertical tick marks on Fe/(Fe+Mg) indicate analysis points. Scale bars 500 microns.
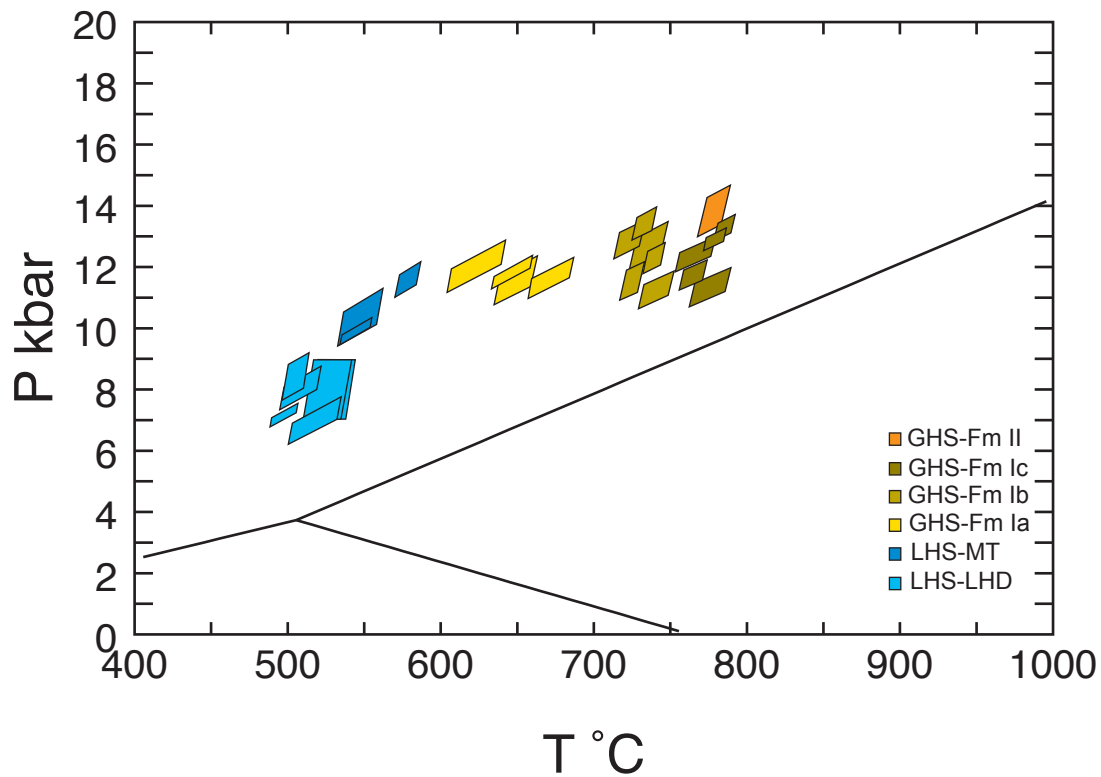
Figure 4.11. Pressure vs. temperatire plot for rocks collected along the Modi Khola. Thermobarometers are from Ferry and Spear (1978), Berman (1990), Dickenson and Hewitt (1986; modified in Laird, 1988; AS01-41b only), Koziol and Newton (1988), and Hoisch (1990).
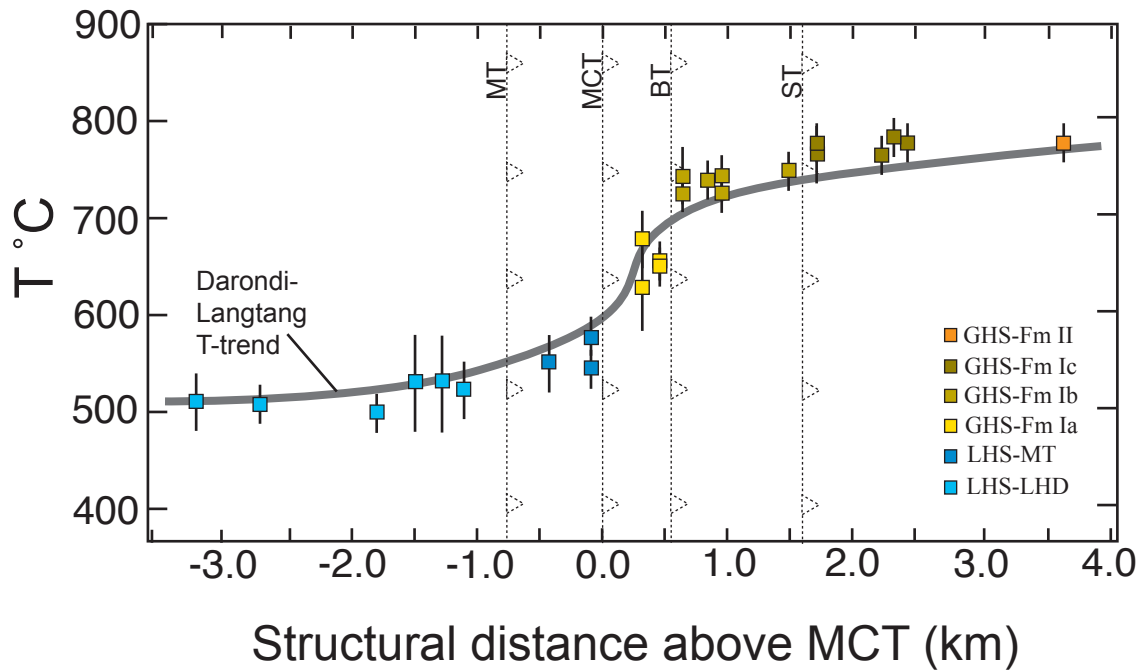
Figure 4.12. Temperature vs. structural distance from Main Central Thrust. Temperatures show a strong gradient across the MCT, then a gradual increase structurally upward. Heavy gray line represents T-distance trend from tansects across the MCT in the Langtang and Darondi regions of Nepal (Kohn et al., 2001; Kohn, 2008). The T profile from this study corresponds well with those collected elsewhere in Nepal.
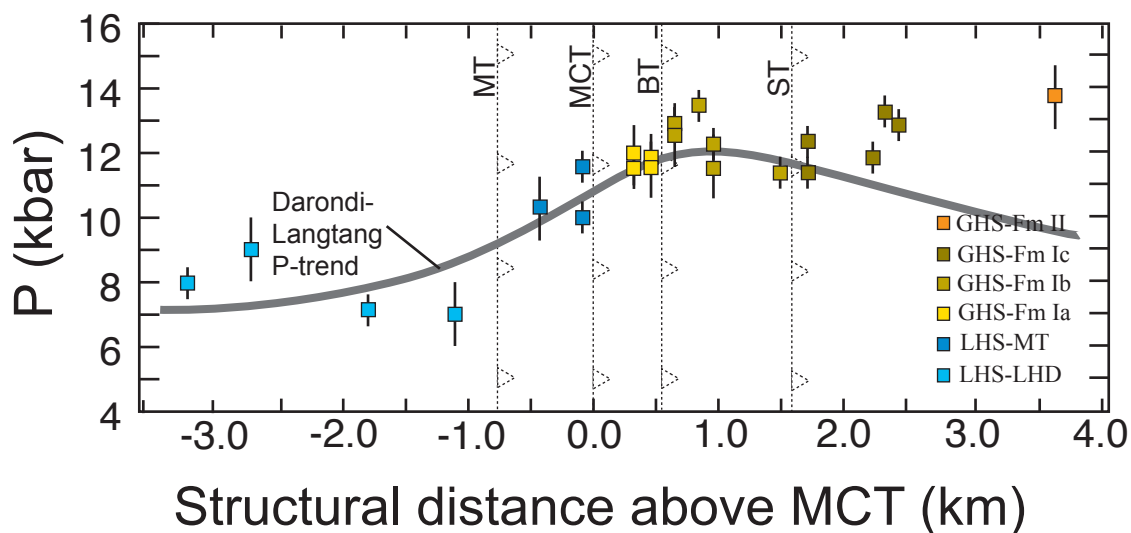
Figure 4.13. Pressure vs. structural distance from Main Central Thrust. Pressures are typically high, show a strong gradient across the MT and MCT, then a gradual increase structurally upward. Heavy gray line represents P-distance trend from tansects across the MCT in the Langtang and Darondi regions of Nepal (Kohn et al., 2001; Kohn, 2008). The P profile from this study does not show the decrease in pressures structurally upward as seen in Darondi and Langtang. One potential reason for this is the narrowness of the GHS in the Annapurna region versus the relatively wide GHS elsewhere in Nepal.
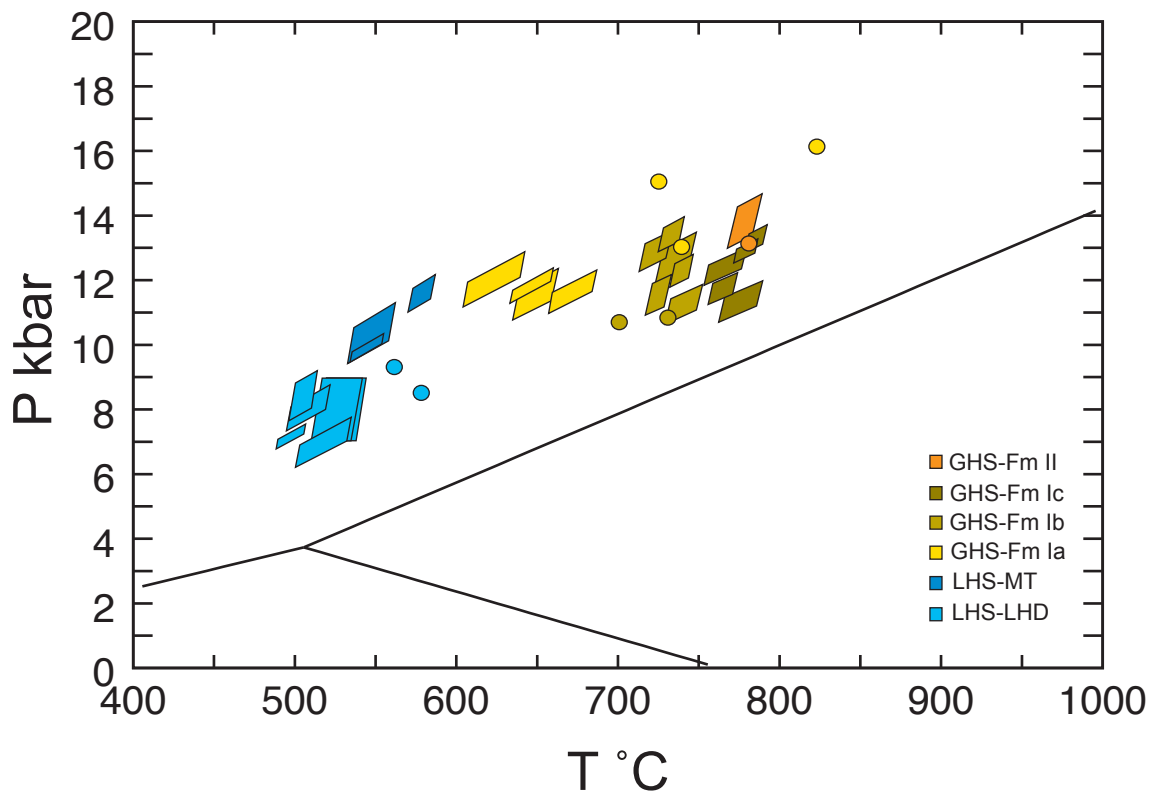
Figure 4.14. Pressure vs. temperature plot for rocks from the Annapurna region (boxes = this study; circles = Martin et al., 2010). Data from Martin et al. (2010) corresponds well with calculated P's and T's in this study with the exception of data from GHS Formation 1a.
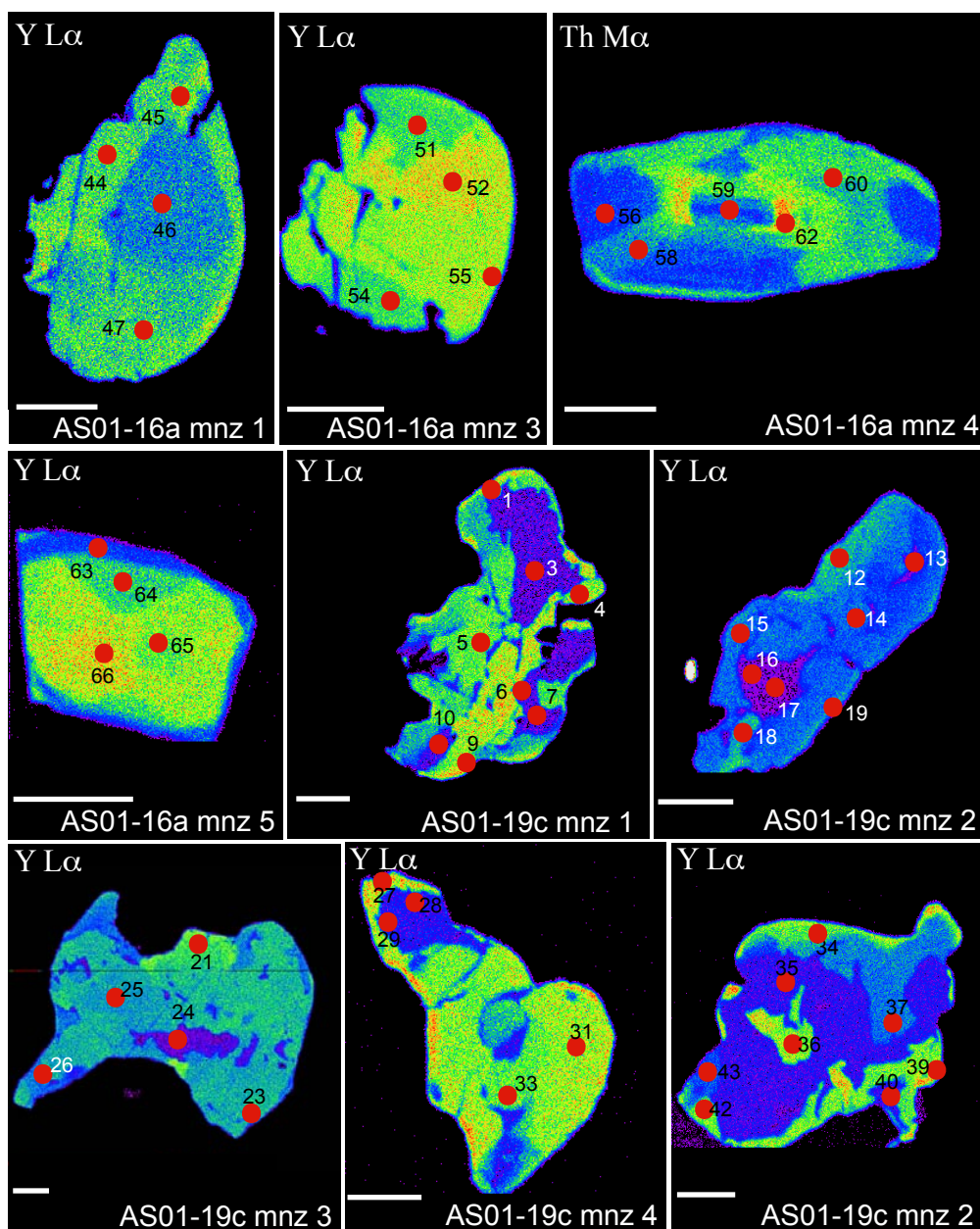
Figure 4.15. X-ray maps of monazite with quantitative chemical analysis locations. Analyses are from samples AS01-16a and AS01-19c. Red dots indicate spot locations for electron microprobe analyses (Tables 4.10 and 4.11). Numbers next to the red dots correspond to the analysis number in the tables. Warm colors indicate higher concentration of element, cool colors lower concentration. Scale bars are 50 μm.
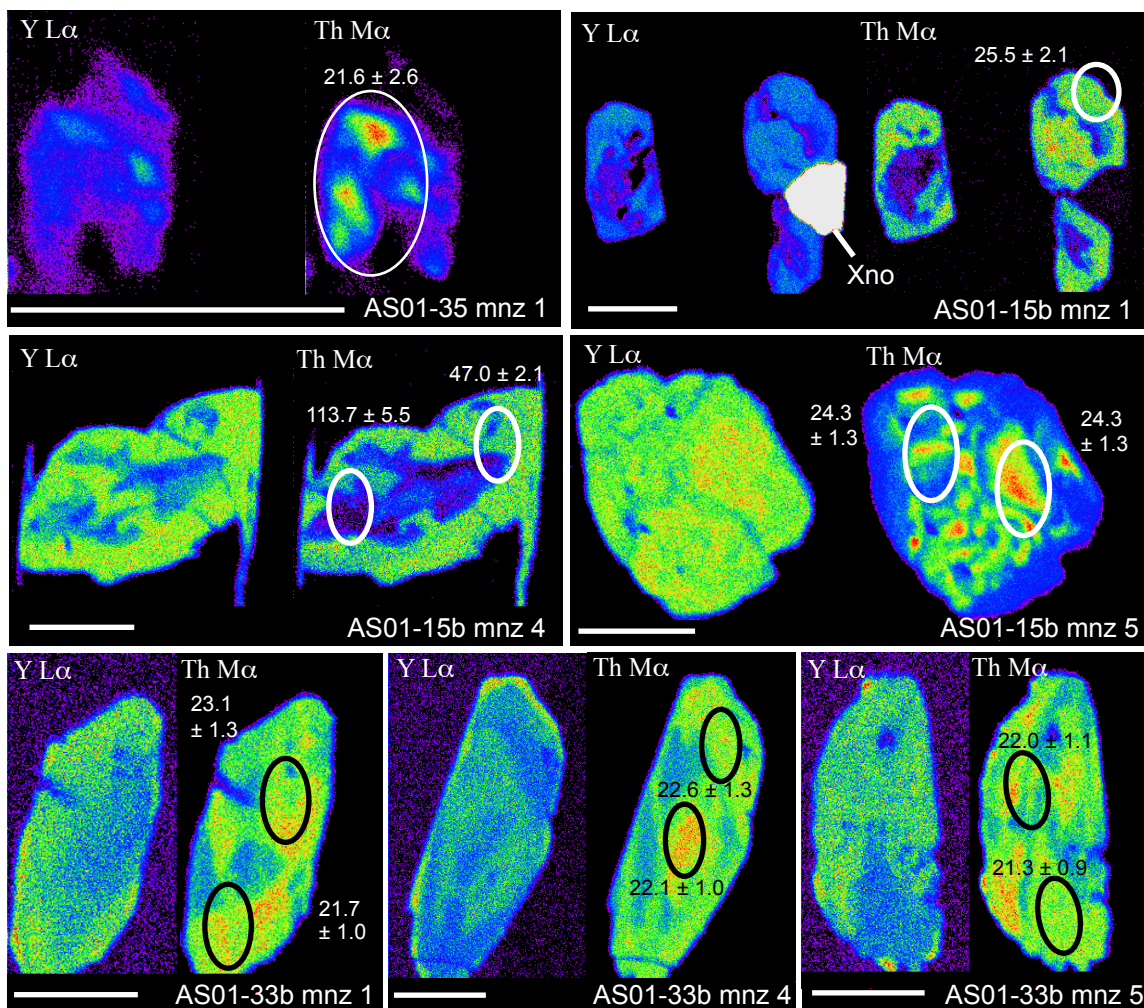
Figure 4.16. X-ray maps of monazite from Greater Himalayan Sequence Formation 1a with ion probe data. Ovals and their corresponding ages represent SIMS analysis spot locations. These monazites exhibit mottled Y and Th zoning patterns, except for two monazites from AS01-15b, which have low Th cores. Geochronologic analysis of this domain indicates an inherited component, yielding geologically meaningless ages. Uncertainties are 2σ; scale bars are 50 μm. Xno = xenotime.
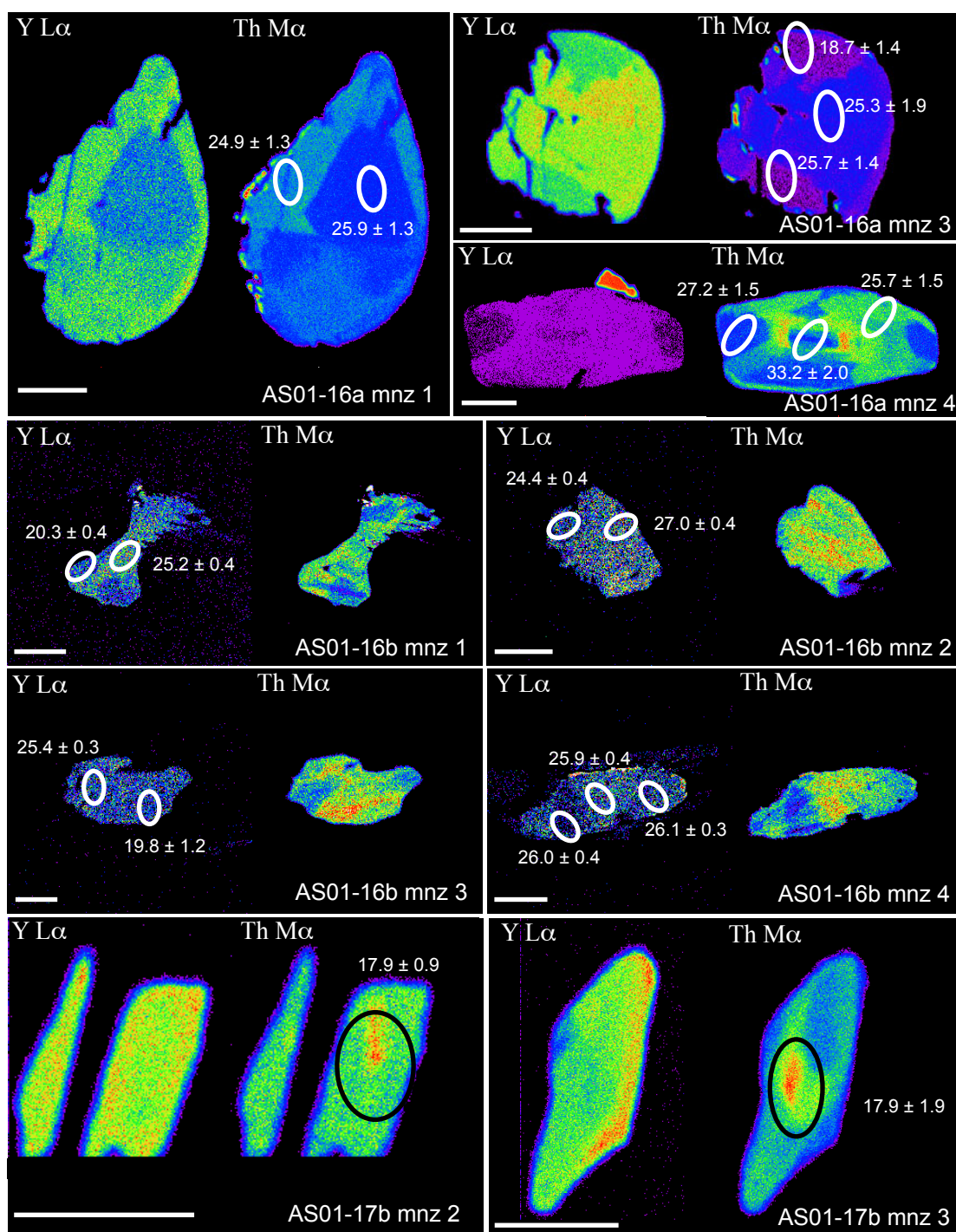
Figure 4.17. X-ray maps of monazite from Greater Himalayan Sequence Formation 1b
with ion probe data. Ovals and their corresponding ages represent SIMS analysis spot
locations. Monazites display distinct low-Y cores and high-Y rims, or an indistinct zoning
that is geochronologically inhomogeneous. Uncertainties are 2σ; scale bars are 50 μm.
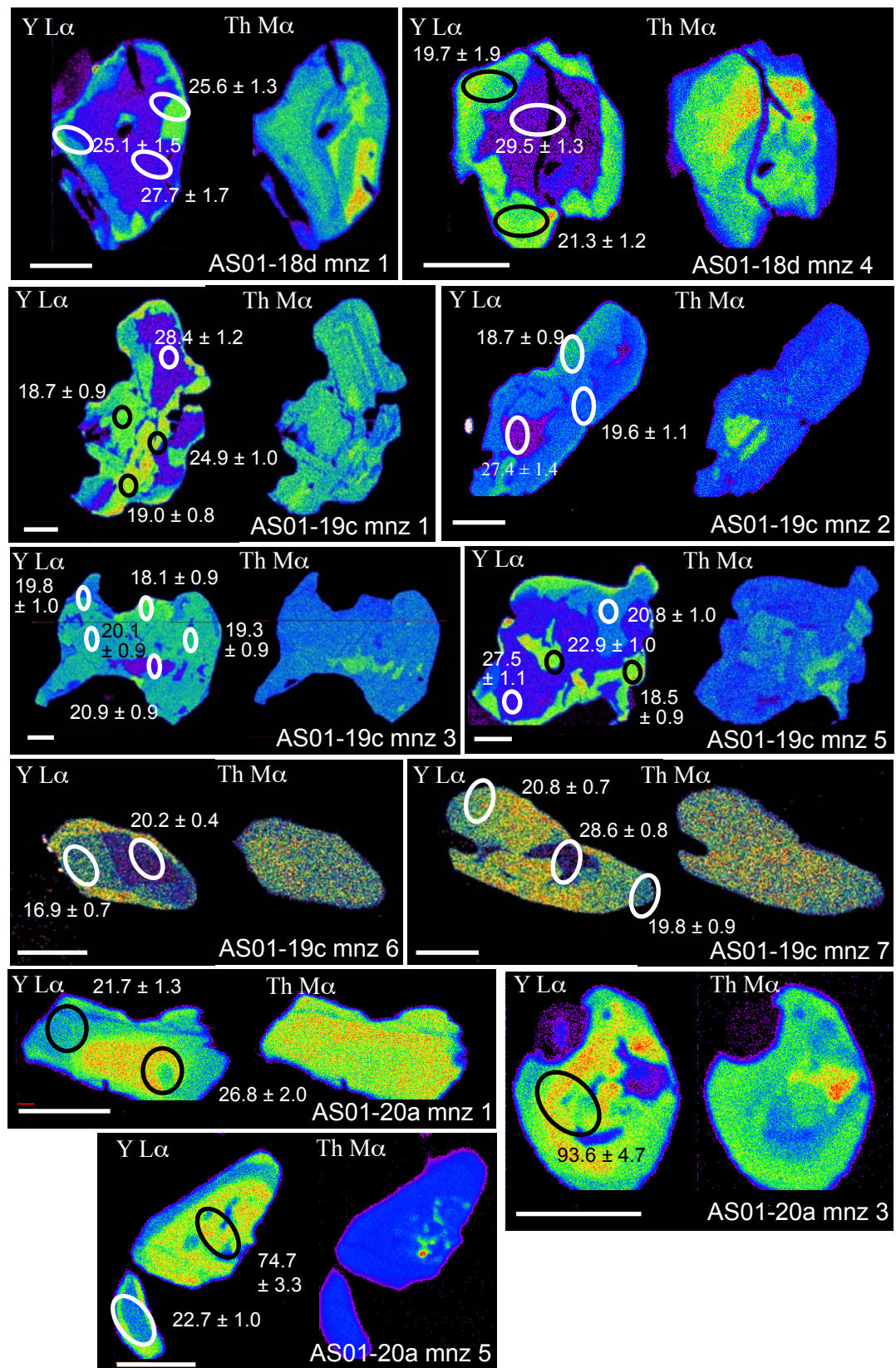
Figure 4.17 (continued).
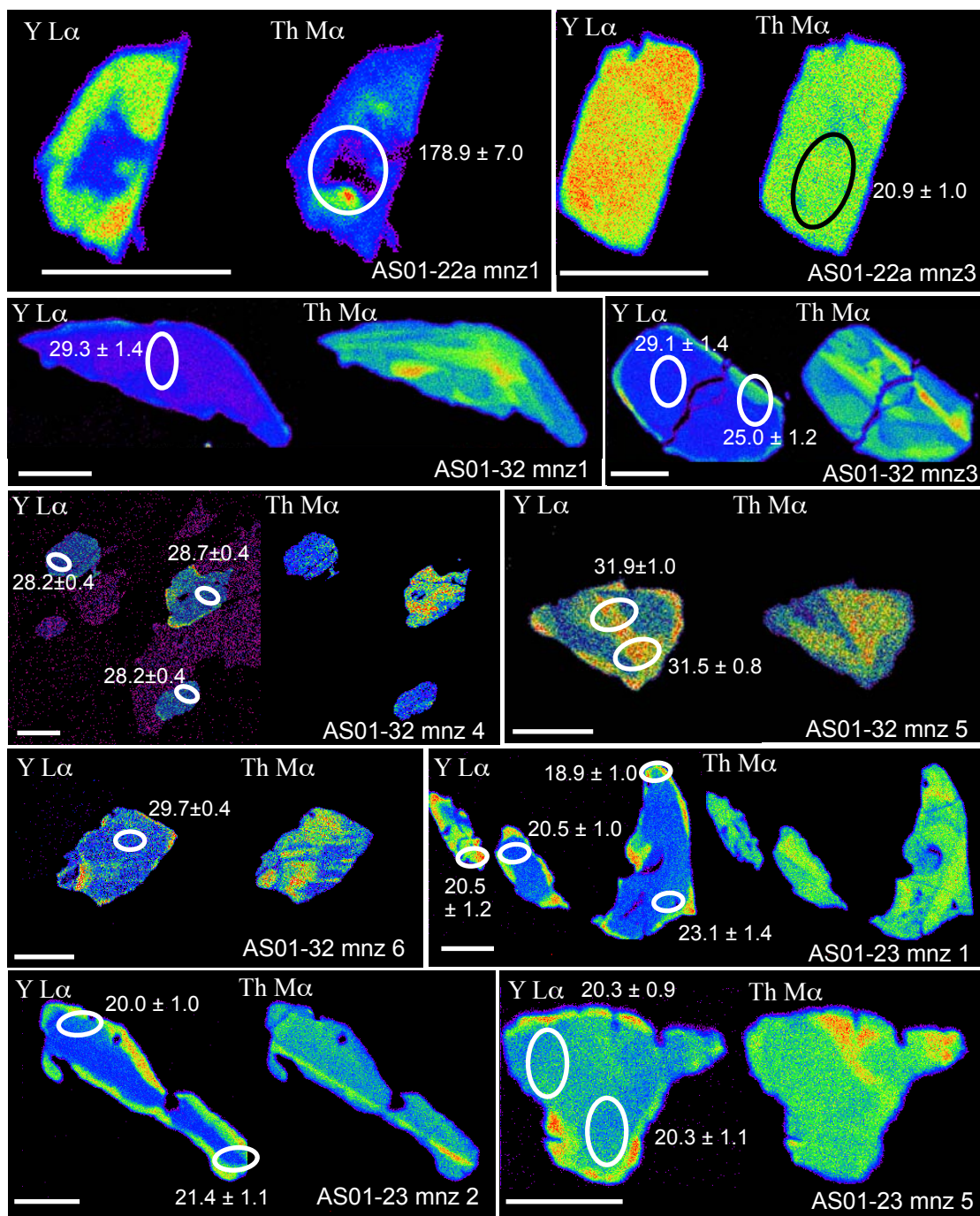
Figure 4.18. X-ray maps of monazite from Greater Himalayan Sequence Formation 1c with ion probe data. Ovals and their corresponding ages represent SIMS analysis spot locations. Monazites display distinct low-Y cores and high-Y rims, the product of prograde growth and post-anatectic cooling, respectively. Uncertainties are 2σ; scale bars are 50 μm.
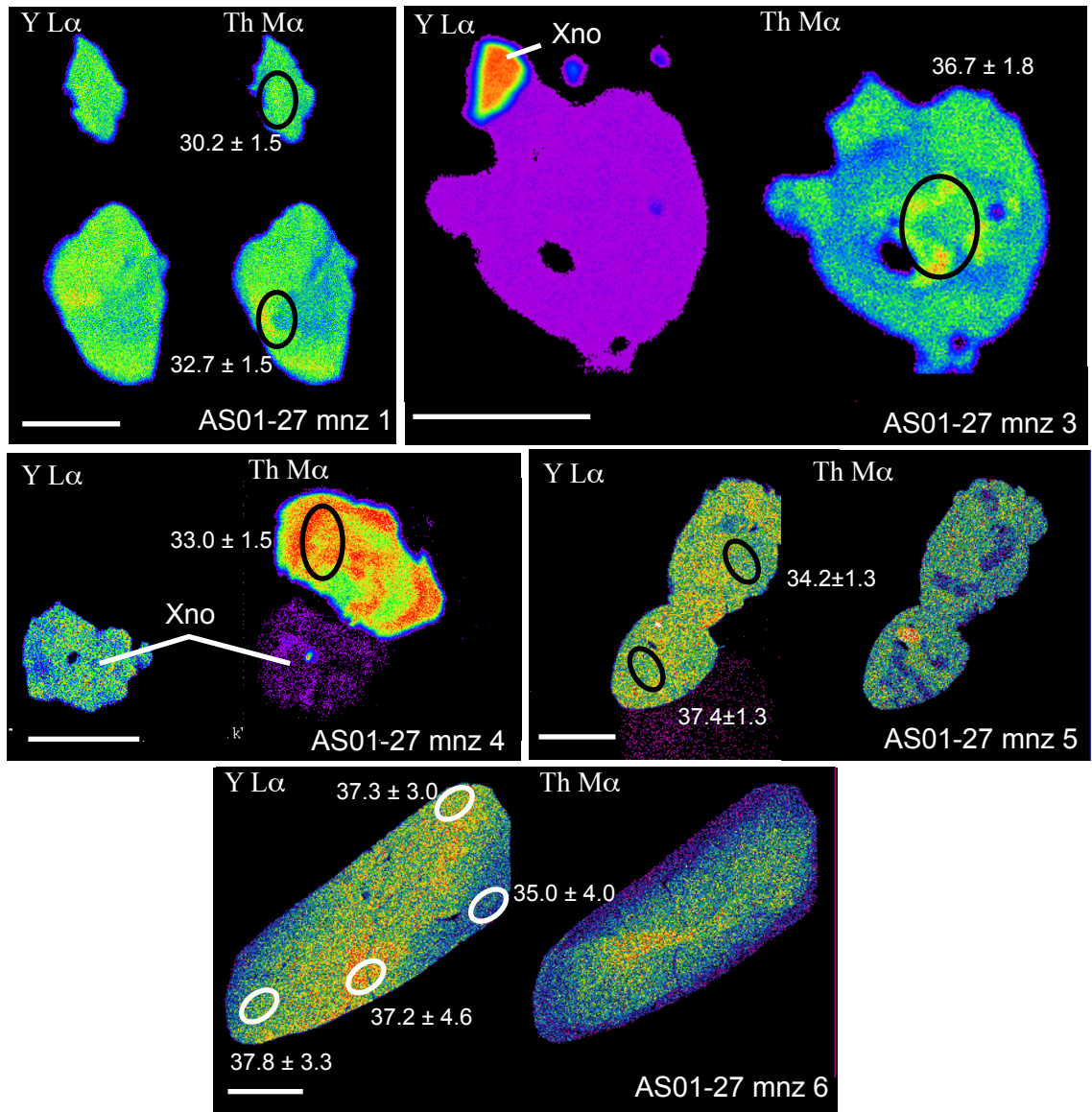
Figure 4.19. X-ray maps of monazite from Greater Himalayan Sequence Formation III with ion probe data. Ovals and their corresponding ages represent SIMS analysis spot locations. Monazites display mottled zoning patterns or slightly high-Th cores that decrease rimward. There is no evidence for rim growth associated with cooling after melting. Uncertainties are 2σ; scale bars are 50 μm. Xno = xenotime.

GHS Fm III

early prograde: 35-38 Ma
late prograde: 30-35 Ma

n = 10

GHS Fm 1c

early prograde: 31-32 Ma
late prograde: 27-30 Ma
cooling: 19-22 Ma

melting

n = 17

ST

GHS Fm 1b

melting

early prograde: 33 Ma
late prograde: 24-29 Ma
cooling: 17-22 Ma

n = 44

BT

GHS Fm 1a

early prograde: 24-26 Ma
late prograde: 21-23 Ma

Ms age

n = 10

MCT

Relative Probability (Arbitrary units)

10   15   20   25   30   35   40   45

Age (Ma)

Early prograde; mottled zoning
Late prograde; low-Y and/or low-Th cores
Cooling; high-Y, post-anatectic

Figure 4.20. Probability distributions of monazite ages, distinguished according to monazite chemistry. Red lines illustrate timing of peak metamorphism. Arrow in GHS Fm 1a box shows a published Ar/Ar muscovite age from the same structural level (Vannay and Hodges, 1996).
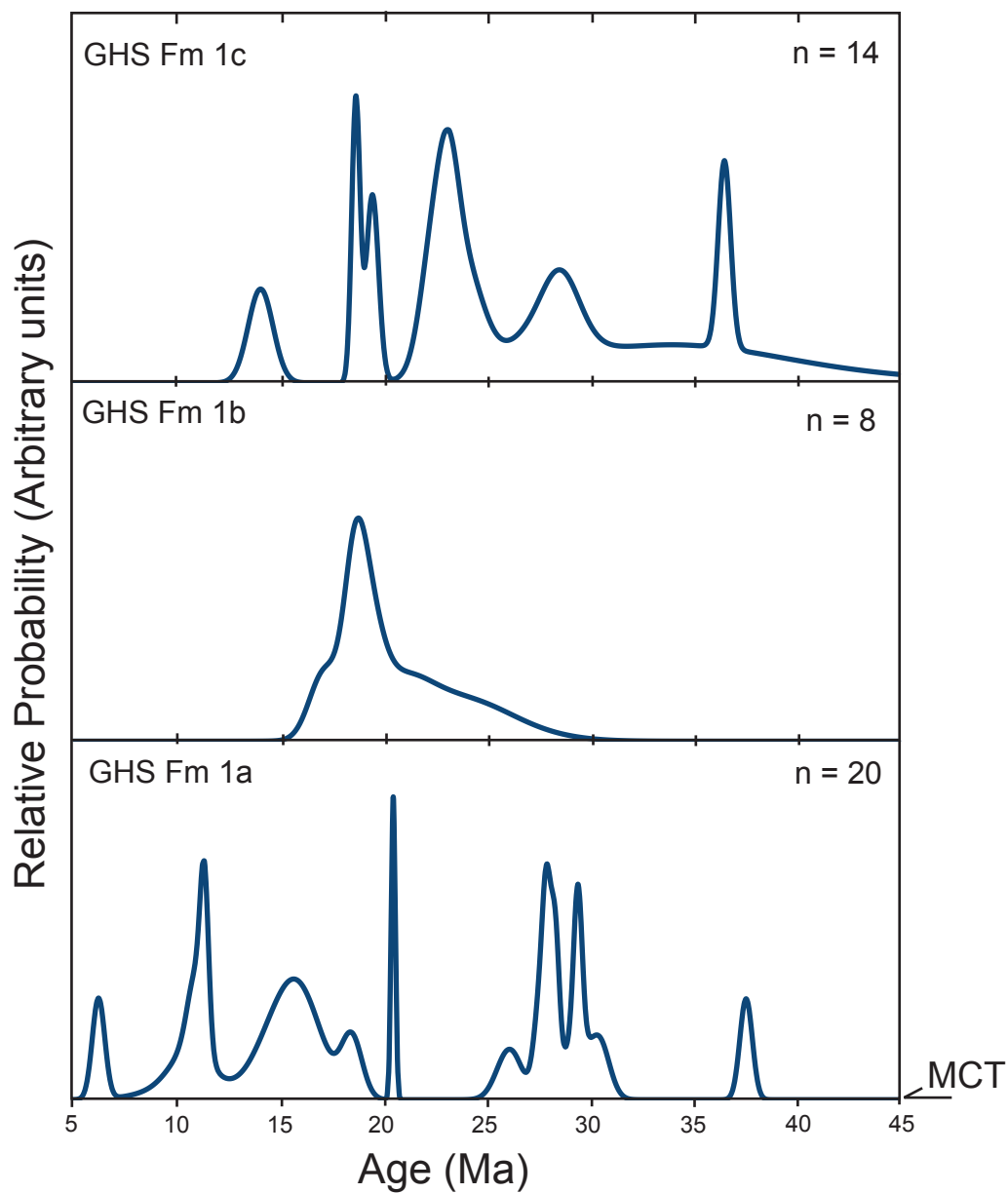
Figure 4.21. Probability distributions of monazite ages. Data from Catlos et al. (2001) Greater Himalayan Sequence Formation I samples. Further division into Formation 1a, 1b, and 1c for comparison to this study is based upon petrology (e.g., mineral assemblages and degree of migmatization).
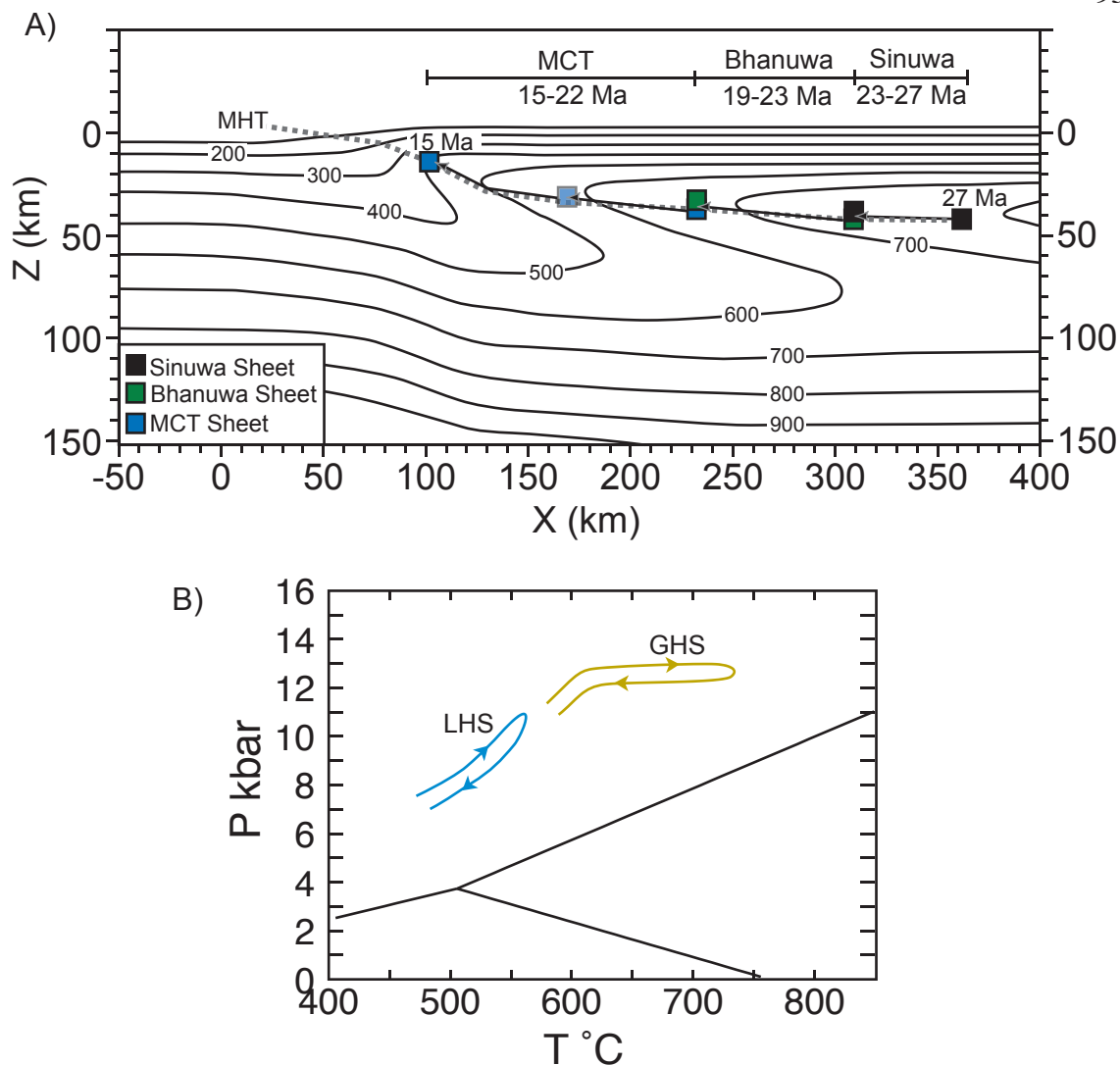
Figure 4.22. A) Schematic illustration of the displacements of different thrust packages in the context of the modern Main Himalayan Thrust and thermal models for the Himalaya (Henry et al., 1997). The location and timing of each spot is constrained by the thermobarometric calculations, the thermal structure, and cooling ages determined by monazite or muscovite geochronology. B) Pressure-temperature diagram with predicted P-T paths based on thermal model in (A) and average peak P-T conditions in GHS and LHS. Critical taper models predict nearly isobaric heating and cooling P-T paths for GHS rocks and 'hairpin' P-T paths for LHS rocks (Kohn, 2008).
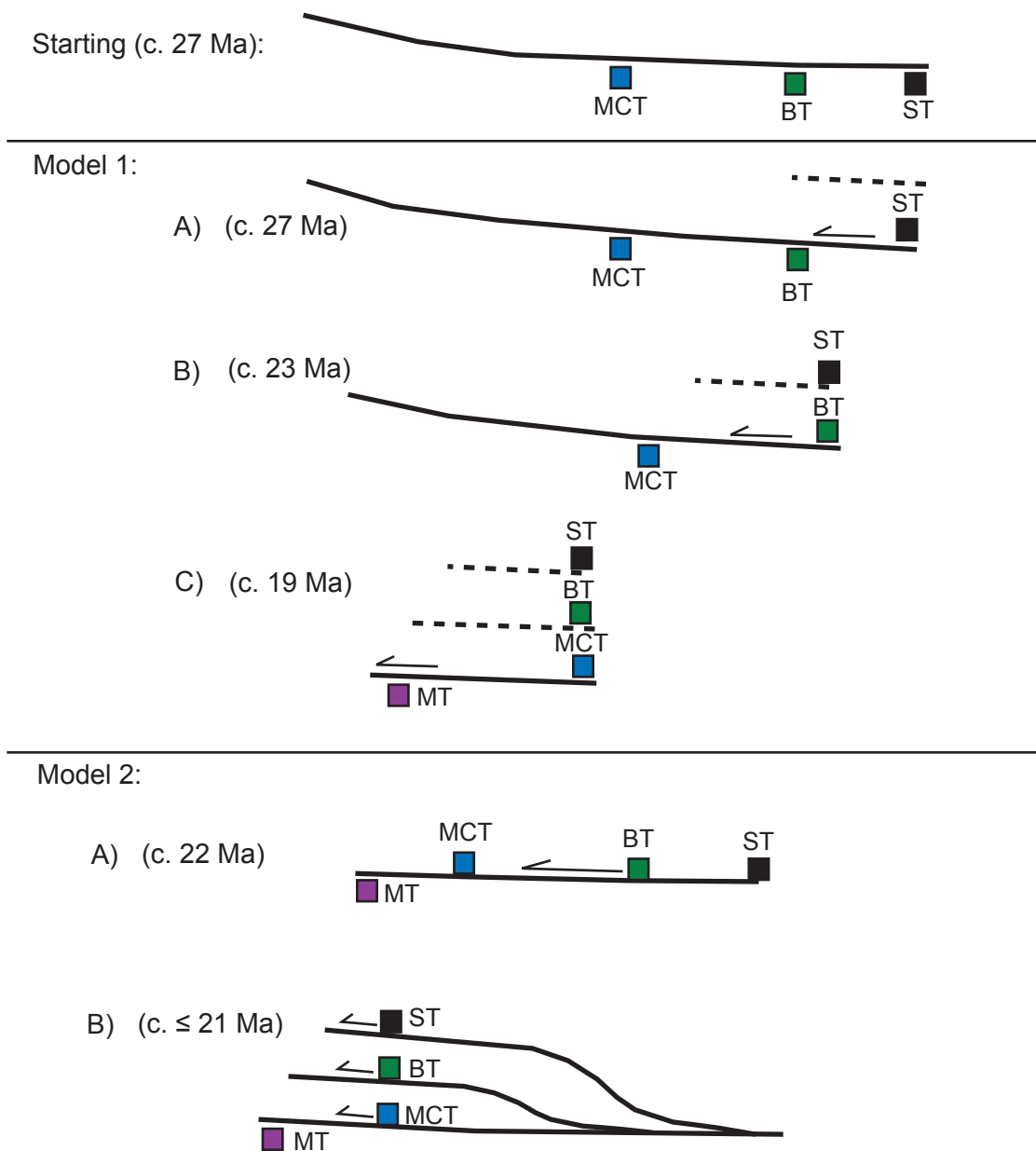
Figure 4.23. Schematic diagram showing two end-member models of thrust development. Model 1 exhibits in-sequence thrusting as the thrust plane cuts down section. Model 2 describes out-of-sequence thrusting initial cooling of all three thrust packages at ~22 Ma. This involves transport and cooling of each thrust package along the same basal thrust surface (the MCT) and later juxtaposition of the BT and ST. MCT = Main Central Thrust; MT = Munsiari Thrust; BT = Bhanuwa Thrust, ST = Sinuwa Thrust.

t₁ (19-20 Ma):

Annapurna   Langtang
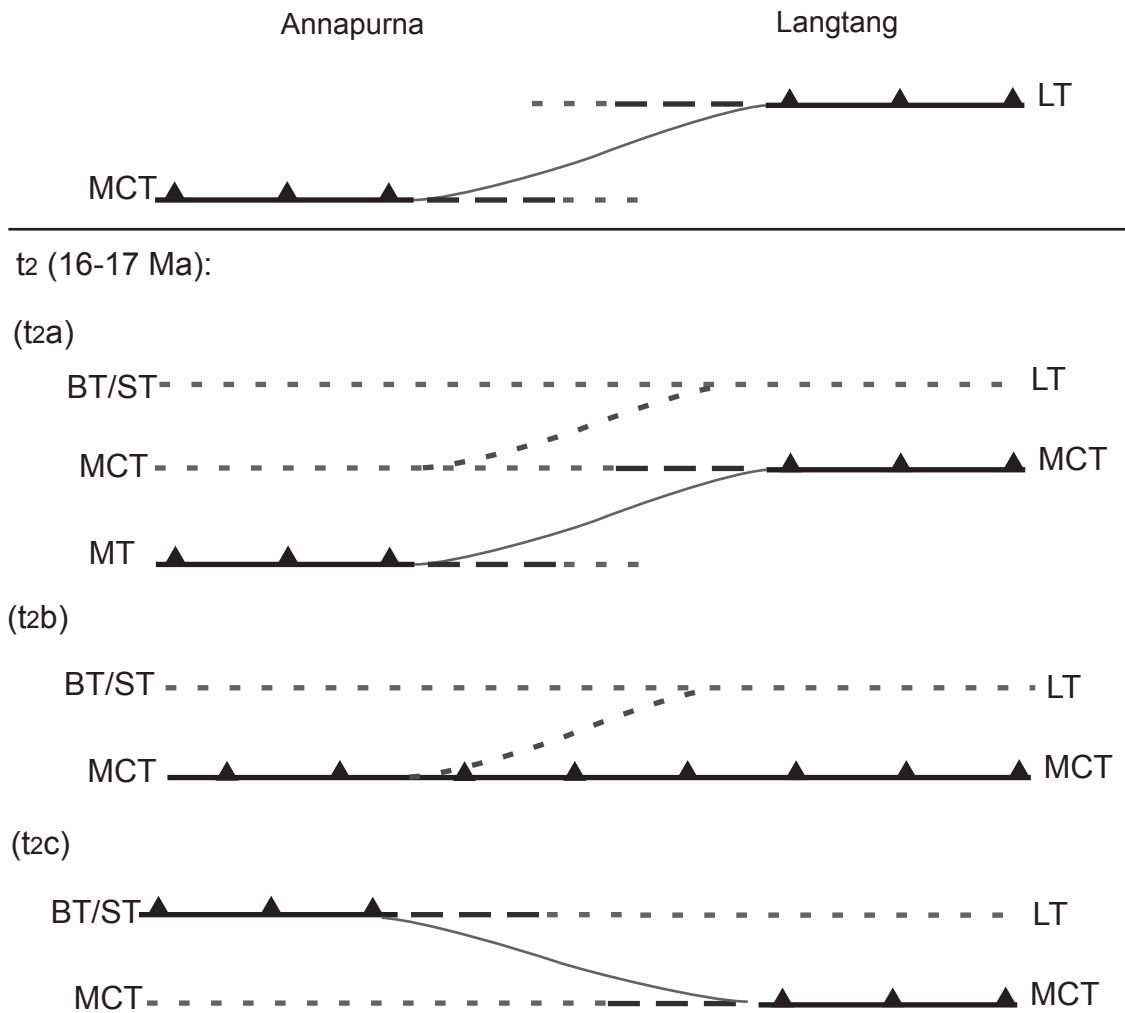
Figure 4.24. Schematic diagram of potential thrust development. t₁ represents an initial thrust structure at 19-20 Ma in which the two thrusts either die out along strike, or have a lateral ramp connecting the Annapurna and Langtang regions. Potential progressions include continued under-thrusting preserving the lateral ramp (t₂a), prolonged MCT transport at Annapurna allowing the MCT at Langtang to catch up (t₂b), or the development of a lateral ramp accomodating synchronous movement of cooled BT and ST thrust sheets at Annapurna and a hot MCT sheet at Langtang. BT = Bhanuwa Thrust; MCT = Main Central Thrust; MT = Munsiari Thrust; ST = Sinuwa Thrust.

Table 4.1 Mineral Assemblages For Rocks from the Lesser Himalayan Sequence, Annapurna Region.

Sample	Rock Unit	Rock Type	Pl	Bt	Grt	Ms	Hbl	Chl	Ky/Sil	Rut	Mnz	Ilm	Ttn	Tur	Other
AS01-47	LLHS Kuncha	qtzite/phyllite	X	X		X		X							aln
AS01-46	LLHS Kuncha	phyllite	X	X	X	X		X							aln, zrm
AS01-45a	LLHS Kuncha	quartzite	X	X	X	X		X				X			aln, zrm
AS01-45c	LLHS Kuncha	schist	X	X		X								X	
AS01-45d	LLHS Kuncha	schist	X	X				X							
AS01-44a	LLHS Kuncha	schist	X	X	X	X		X						X	zrm
AS01-44b	LLHS Kuncha	quartzite	X	X	X	X		X							
AS01-43a	LLHS Kuncha	schist		X	X	X		X				X		X	aln
AS01-43b	LLHS Kuncha	schist		X		X						X		X	
AS01-42	LLHS Ulleri	gneiss	X	X		X									
AS01-42b	LLHS Ulleri	gneiss	X	X		X					Xh				aln
AS01-41a	LLHS Kuncha	schist			X	X		X				X			cld
AS01-41b	LLHS Kuncha	schist			X	X		X				X			cld
AS01-40a	LLHS Kuncha	schist		X		X		X				X			
AS01-40b	LLHS Kuncha	amphibolite	X	X			X	X				X			zrm
AS01-40c	LLHS Kuncha	amphibolite	X	X			X	X				X			zrm
AS01-40d	LLHS Kuncha	quartzite				X									
AS01-40e	LLHS Kuncha	schist	X	X	X	X		X			Xh	X			
AS01-40f	LLHS Kuncha	schist	X	X	X	X		X				X		X	
AS01-39	ULHS Dhading	marble				X									cal, ep
AS01-38a	LLHS Kuncha	schist	X	X	X							X		X	aln
AS01-38b	LLHS Kuncha	schist	X	X	X	X						X		X	
AS01-37a	ULHS Dhading	quartzite	X			X								X	cal
AS01-37b	ULHS Dhading	phyllite				X									cal
AS01-37c	ULHS Dhading	schist	X	X		X						X		X	aln, zrm
AS01-14a	ULHS Benighat	schist		X	X	X								X	aln, zrm
AS01-36a	ULHS Malekhu	schist	X	X	X	X						X		X	aln, xno, zrm
AS01-36b	ULHS Malekhu	schist	X	X	X	X						X			

Note: samples are ordered from lowest structural level to highest; all samples contain quartz and apatite
Xh: monazite is not prograde, but rather a product of hydrothermal alteration
LLHS: Lower Lesser Himalayan Sequence; ULHS: Upper Lesser Himalayan Sequence

Table 4.2. Mineral Assemblages for Rocks from the Greater Himalayan Sequence, Annapurna Region.

#	Unit	Rock Type	Pl	Bt	Grt	Ms	Hbl	Chl	Ky/Sil	Rut	Mnz	Ilm	Ttn	Tur	Other
35	Fm Ia	schist	X	X		X					X				zrn
15a	Fm Ia	schist	X	X	X		X			X					ep
15b	Fm Ia	schist	X	X					ky	X	X			X	xno, zrn
15c	Fm Ia	quartzite	X	X	X	X				X					
33a	Fm Ia	quartzite	X	X	X	X									czo
33b	Fm Ia	schist	X	X	X	X				X	X				zrn
16a	Fm Ib	gneiss	X	X	X	X				X	X				par, xno
16b	Fm Ib	gneiss	X	X	X	X				X	X				par, zrn
16c	Fm Ib	gneiss	X	X	X	X			ky	X	X			X	st
17a	Fm Ib	quartzite	X	X	X							X			aln, zrn
17b	Fm Ib	schist	X	X	X	X					X	X			
18a	Fm Ib	schist	X	X	X	X			ky		X			X	
18b	Fm Ib	schist	X	X	X	X				X	X				zrn
18d	Fm Ib	gneiss	X	X	X				ky	X	X				xno, zrn
19a	Fm Ib	calc-silicate		X	X			X						X	cpx, czo
19b	Fm Ib	quartzite	X	X		X					X			X	ksp, zrn
19c	Fm Ib	gneiss	X	X	X	X				X	X				st, zrn
20a	Fm Ic	gneiss	X	X	X				ky	X	X				st, zrn
20b	Fm Ic	leucosome	X	X	X				ky	X		X			
20c	Fm Ic	gneiss	X	X	X	X			ky	X					
21	Fm Ic	gneiss	X	X	X	X									
22a	Fm Ic	schist	X	X	X	X			ky		X				zrn
22b	Fm Ic	schist	X	X					ky+sil*						
22c	Fm Ic	schist	X	X					ky		X			X	
32	Fm Ic	gneiss	X	X	X				ky	X	X			X	zrn
23	Fm Ic	quartzite	X	X	X	X					X				
24a	Fm Ic	gneiss	X	X	X	X									ep, zrn
24b	Fm Ic	quartzite	X	X	X	X									zrn
24c	Fm Ic	quartzite	X	X	X	X									zrn
25a	Fm II	leucogranite	X	X	X	X									ksp, zrn
25b	Fm II	amphibolite	X		X		X					X	X		cpx, zrn
25c	Fm II	quartzite	X			X									
25	Fm II	amphibolite	X		X		X						X		cpx
25e	Fm II	amphibolite	X		X		X	X							cpx, ep, zrn
25f	Fm II	amphibolite	X				X						X		cpx
31a	Fm II	quartzite	X	X	X	X	X				X	X			ep, ksp, zrn
31b	Fm II	calc-silicate	X	X	X		X						X		cal, cpx, ksp, zrn
31c	Fm II	calc-silicate	X	X			X						X		cal, cpx, zrn
30a	Fm II	calc-silicate	X	X			X						X		cal, cpx, ep, ksp, zrn
30b	Fm II	calc-silicate	X				X						X		cal, cpx, ep, ksp, zrn
29	Fm II	calc-silicate	X	X			X						X		cal, cpx, czo
29-1	Fm II	calc-silicate	X	X	X		X						X		cal, cpx, czo
28	Fm II	quartzite	X	X						X	X			X	zrn
27	Fm III	orthogneiss	X	X		X					X				xno, zrn
26a	Fm II	marble		X									X		cal, cpx, zrn
26b	Fm II	marble		X									X		cal, cpx, zrn

Note: samples are ordered from lowest structural level to highest; all samples contain quartz and apatite
Sample numbers follow the format AS01-xx
*: sillimanite is locally developed on plagioclase rims, and not a regional feature

Table 4.3 Mineral Compositions from the Lesser Himalayan Duplex

Garnet

Sample	46	46	46	45a	45a	45a	44a	44a	43a	43a	43a	41b	41b	41b	40e	40e	40e	40e
Garnet	3	3	1	4	1	1	1	2	1	1	1	4	4	4	2	2	3	3
Traverse	1	2	1	1	1	1	1	1	1	1	1	1	1	1	1	1	1	1
Analysis	2	2	2	3	5	6	9	86	6	7	147	141	142	143	134	135	222	224
Si	2.992	2.949	3.025	2.982	2.974	2.949	2.977	2.987	2.940	2.939	2.937	2.965	2.996	2.994	2.957	2.961	2.962	2.976
Ti	0.005	0.020	0.002	0.007	0.025	0.017	0.004	0.003	0.004	0.004	0.004	0.002	0.006	0.008	0.004	0.006	0.003	0.003
Al	1.994	1.994	1.967	2.041	2.073	2.079	2.000	2.020	2.058	2.068	2.012	2.044	2.016	2.023	2.024	2.026	2.029	2.046
Mg	0.124	0.130	0.118	0.114	0.120	0.126	0.111	0.108	0.097	0.097	0.112	0.176	0.174	0.165	0.149	0.166	0.166	0.161
Ca	0.455	0.491	0.471	0.718	0.530	0.575	0.464	0.489	0.532	0.553	0.462	0.417	0.447	0.438	0.376	0.358	0.322	0.320
Mn	0.151	0.166	0.136	0.451	0.399	0.408	0.157	0.191	0.130	0.141	0.164	0.108	0.108	0.100	0.252	0.253	0.217	0.228
Fe	2.281	2.280	2.261	1.676	1.842	1.836	2.306	2.199	2.267	2.222	2.357	2.298	2.242	2.256	2.263	2.248	2.321	2.263
Na	0.000	0.006	0.018	0.001	0.005	0.012	-	0.003	-	-	0.008	0.002	-	0.002	0.001	0.003	0.001	0.001
K	0.007	0.002	0.001	0.001	0.001	0.002	-	-	-	0.001	0.001	-	-	-	-	-	-	-
Wt% Total	101.28	99.44	99.86	99.48	100.76	99.65	100.68	99.43	100.84	100.65	99.24	98.42	99.55	99.01	99.76	100.48	100.09	100.80
Alm	0.758	0.744	0.757	0.566	0.637	0.624	0.759	0.736	0.749	0.737	0.762	0.766	0.755	0.762	0.744	0.743	0.767	0.761
Grs	0.151	0.160	0.158	0.243	0.183	0.195	0.153	0.164	0.176	0.183	0.149	0.139	0.150	0.148	0.124	0.118	0.106	0.108
Prp	0.041	0.042	0.040	0.038	0.041	0.043	0.037	0.036	0.032	0.032	0.036	0.059	0.059	0.056	0.049	0.055	0.055	0.054
Sps	0.050	0.054	0.045	0.152	0.138	0.139	0.052	0.064	0.043	0.047	0.053	0.036	0.036	0.034	0.083	0.084	0.072	0.077
Fe/(Fe+Mg)	0.948	0.946	0.950	0.936	0.939	0.936	0.954	0.953	0.959	0.958	0.955	0.929	0.928	0.932	0.938	0.931	0.933	0.934

Cations are normalized to an anhydrous basis of 12 oxygens.

Plagioclase

Sample	46	46	46	45a	45a	45a	44a	44a	44a	40e	40e	40e
Analysis	167	169	173	30	32	36	31	16	32	29	31	44
X_{An}(%)	16.6	15.9	17.4	14.6	17.5	17.7	18.2	18.3	18.7	18.2	17.7	17.7
Wt% Total	101.81	99.17	100.65	100.40	100.38	100.65	100.32	100.46	99.82	99.53	99.63	99.03

Table 4.3 Continued
Other Major Silicate Minerals

Sample	46	46	46	46	46	46	45a	45a	45a	45a	45a	45a	44a	44a	44a	44a	44a	44a	44a
Mineral	Bt	Bt	Ms	Ms	Chl	Chl	Bt	Bt	Bt	Bt	Ms	Chl	Bt	Bt	Bt	Bt	Ms	Ms	Chl
Analysis	146	159	47	64	61	62	24	25	29	36	35	28	12	13	14	22	4	5	18
Si	2.793	2.710	3.142	0.828	5.503	5.195	2.750	2.779	2.795	2.778	3.077	6.305	2.708	2.719	2.699	2.729	3.124	3.071	5.128
Ti	0.107	0.075	0.016	2.765	0.052	0.016	0.119	0.122	0.138	0.131	0.055	0.114	0.111	0.113	0.057	0.101	0.012	0.019	0.010
Al	1.654	1.694	2.668	0.011	5.591	5.803	1.639	1.605	1.580	1.558	2.731	4.794	1.652	1.655	1.732	1.657	2.683	2.802	5.769
Mg	0.782	0.828	0.084	0.001	2.965	3.194	0.926	0.935	0.915	0.949	0.061	2.823	0.789	0.762	0.784	0.766	0.099	0.055	2.975
Ca	0.003	0.003	-	3.068	0.001	0.002	0.006	0.001	0.001	0.006	-	0.027	0.004	0.007	0.006	0.004	-	0.000	0.007
Mn	0.004	0.009	-	0.156	0.016	0.017	0.008	0.008	0.007	0.007	-	0.033	0.007	0.006	0.008	0.005	0.000	-	0.016
Fe	1.493	1.589	0.107	0.079	5.346	5.657	1.384	1.371	1.382	1.414	0.096	4.646	1.615	1.613	1.606	1.608	0.105	0.078	6.070
Na	0.012	0.008	0.097	0.120	0.012	-	0.032	0.015	0.024	0.021	0.062	0.002	0.018	0.014	0.023	0.014	0.105	0.104	-
K	0.860	0.912	0.886	0.002	0.340	0.007	0.925	0.938	0.892	0.917	0.903	0.882	0.920	0.915	0.949	0.932	0.890	0.863	0.005
Wt% Total	94.57	93.49	94.11	94.78	87.69	86.32	93.45	93.38	94.36	93.99	94.58	88.30	95.06	95.68	94.44	95.56	95.45	95.15	87.96
Fe/(Fe+Mg)	0.656	0.657	0.561	0.602	0.643	0.639	0.599	0.594	0.601	0.598	0.614	0.622	0.672	0.679	0.672	0.677	0.516	0.588	0.671

Sample	43a	43a	43a	43a	43a	41b	41b	41b	41b	41b	41b	41b	40e	40e	40e	40e	40e	40e	40e
Mineral	Bt	Bt	Bt	Bt	Ms	Ms	Ms	Chl	Chl	Chl	Ctd	Ctd	Bt	Bt	Bt	Ms	Ms	Chl	Chl
Analysis	38	51	52	53	39	39	40	8	11	17	2	35	9	21	22	27	38	20	36
Si	2.722	2.695	2.722	2.729	3.068	3.067	3.071	5.251	5.146	5.232	2.029	2.015	2.718	2.711	2.711	3.119	3.092	5.254	5.254
Ti	0.113	0.111	0.110	0.112	0.012	0.013	0.008	0.012	0.013	0.012	0.001	0.002	0.083	0.104	0.096	0.013	0.014	0.012	0.034
Al	1.647	1.666	1.658	1.694	2.796	2.814	2.811	5.924	5.960	5.906	3.953	3.924	1.680	1.691	1.669	2.679	2.731	5.676	5.675
Mg	0.691	0.679	0.686	0.662	0.060	0.055	0.059	3.589	3.725	3.680	0.256	0.286	0.906	0.881	0.891	0.111	0.092	3.326	3.184
Ca	0.005	0.000	0.003	0.001	0.002	0.003	0.001	0.012	0.004	0.003	0.001	0.002	0.004	0.002	0.006	-	-	0.005	0.007
Mn	0.005	0.007	0.004	0.004	0.002	-	-	0.016	0.024	0.018	0.023	0.029	0.007	0.006	0.003	0.001	0.001	0.035	0.027
Fe	1.681	1.720	1.682	1.637	0.109	0.081	0.077	4.901	4.983	4.950	1.731	1.760	1.503	1.492	1.523	0.104	0.104	5.582	5.602
Na	0.006	0.010	0.016	0.010	0.112	0.223	0.229	0.112	0.003	-	-	0.003	0.018	0.016	0.030	0.115	0.179	0.014	0.023
K	0.953	0.956	0.933	0.938	0.836	0.738	0.750	0.032	0.007	-	0.001	0.001	0.894	0.890	0.889	0.861	0.814	0.000	0.157
Wt% Total	93.16	93.82	94.79	94.75	95.15	94.24	93.97	85.50	84.57	84.55	92.26	93.13	95.71	95.60	94.44	95.18	94.52	88.63	88.97
Fe/(Fe+Mg)	0.709	0.717	0.710	0.712	0.644	0.596	0.567	0.577	0.572	0.574	0.871	0.860	0.624	0.629	0.631	0.508	0.531	0.627	0.638

Cations normalized to an anhydrous 11 (muscovite and biotite), 28 (chlorite), or 12 (chloritoid) oxygens

Table 4.4 Mineral Compositions of Rocks from the Lesser Himalayan Sequence, Munsiari Thrust.

Garnet

Sample	38b	38b	38b	38b	36a	36a	36a	36b	36b
Garnet	1	1	2	2	2	2	2	1	1
Traverse	1	1	1	1	1	1	1	1	1
Analysis	11	12	53	57	325	328	336	2	3
Si	2.925	2.942	2.950	2.965	2.952	2.958	2.907	2.989	2.967
Ti	0.006	0.006	0.002	0.004	0.003	0.005	0.002	0.002	0.002
Al	2.078	2.078	2.070	2.054	2.049	2.065	2.029	2.089	2.050
Mg	0.199	0.189	0.182	0.198	0.202	0.198	0.204	0.276	0.288
Ca	0.595	0.602	0.623	0.586	0.562	0.570	0.568	0.404	0.422
Mn	0.040	0.039	0.026	0.027	0.269	0.266	0.266	0.015	0.022
Fe	2.185	2.154	2.158	2.169	1.985	1.943	2.099	2.183	2.250
Na	0.006	0.008	0.003	0.001	-	-	0.001	0.011	0.010
K	-	-	-	-	-	-	-	0.003	0.001
Wt% Total	99.74	98.73	100.11	99.95	101.96	101.67	98.93	101.63	100.04
Alm	0.724	0.722	0.722	0.728	0.658	0.653	0.669	0.759	0.754
Grs	0.197	0.202	0.208	0.197	0.186	0.191	0.181	0.140	0.142
Prp	0.066	0.063	0.061	0.066	0.067	0.067	0.065	0.096	0.097
Sps	0.013	0.013	0.009	0.009	0.089	0.089	0.085	0.005	0.007
Fe/(Fe+Mg)	0.917	0.919	0.922	0.916	0.908	0.908	0.911	0.888	0.886

Cations are normalized to an anhydrous basis of 12 oxygens.

Plagioclase

Sample	38b	38b	38b	36a	36a	36b	36b	36b
Analysis	65	66	67	48	50	12	13	14
X_{An}(%)	17.0	17.3	14.6	15.6	16.2	14.5	14.1	13.4
Wt% Total	102.63	102.83	101.68	102.38	101.80	99.95	100.00	99.19

Table 4.4 Continued
Other Major Silicate Minerals

Sample	38b	38b	38b	38b	38b	38b	36a	36a	36a	36a	36a	36b	36b	36b	36b	36b
Mineral	Bt	Bt	Bt	Bt	Ms	Ms	Bt	Bt	Bt	Ms	Ms	Bt	Bt	Bt	Ms	Ms
Analysis	53	55	56	57	64	79	40	41	42	43	34	1	5	10	2	4
Si	2.748	2.748	2.737	2.759	3.130	3.133	2.757	2.747	2.734	2.738	3.153	2.749	2.752	2.741	3.083	3.074
Ti	0.110	0.113	0.105	0.115	0.023	0.021	0.104	0.095	0.103	0.116	0.024	0.115	0.121	0.115	0.018	0.023
Al	1.682	1.687	1.607	1.629	2.652	2.646	1.667	1.653	1.645	1.645	2.597	1.653	1.637	1.660	2.743	2.766
Mg	1.020	1.005	1.075	1.044	0.131	0.140	1.066	1.094	1.118	1.088	0.150	1.135	1.156	1.143	0.114	0.104
Ca	0.002	0.002	0.006	0.006	0.001	0.001	-	0.002	0.001	0.004	-	0.001	0.000	0.004	0.001	0.001
Mn	0.002	0.002	-	0.006	-	0.002	0.008	0.009	0.006	0.011	0.002	0.006	0.004	0.005	0.000	0.000
Fe	1.278	1.280	1.380	1.320	0.103	0.109	1.256	1.278	1.282	1.271	0.116	1.189	1.181	1.199	0.090	0.081
Na	0.014	0.014	0.013	0.015	0.102	0.093	0.008	0.013	0.011	0.015	0.063	0.016	0.020	0.015	0.126	0.157
K	0.906	0.908	0.875	0.853	0.864	0.853	0.888	0.896	0.890	0.889	0.902	0.906	0.895	0.880	0.833	0.786
Wt% Total	96.79	97.41	97.14	97.38	96.54	96.50	97.61	97.26	97.16	97.55	95.81	93.39	93.39	93.23	93.62	93.23
Fe/ (Fe+Mg)	0.556	0.560	0.562	0.558	0.439	0.438	0.541	0.539	0.534	0.539	0.434	0.512	0.505	0.512	0.442	0.440

Cations normalized to an anhydrous 11 oxygens

Table 4.5 Mineral Compositions of Rocks from the Greater Himalayan Sequence Formation 1a.

Garnet

Sample	15a	15a	15a	15a	15c	15c	15c	33a	33a	33a	33b	33b	33b
Garnet	1	2	2	2	1	1	2	1	1	1	1	2	3
Traverse	1	1	1	2	1	1	1	1	1	1	1	1	1
Analysis	4	12	13	13	7	8	116	3	4	6	8	10	8
Si	3.011	3.009	2.998	3.010	2.958	2.973	2.968	2.946	2.934	2.942	3.015	3.023	3.022
Ti	-	-	0.002	0.001	-	-	0.001	0.003	0.004	0.003	-	0.001	0.001
Al	1.985	1.975	1.983	1.976	2.026	2.005	2.041	2.040	2.057	2.042	1.945	1.933	1.923
Mg	0.567	0.528	0.530	0.533	0.529	0.535	0.537	0.239	0.231	0.244	0.591	0.595	0.593
Ca	0.573	0.779	0.780	0.748	0.231	0.240	0.238	1.218	1.228	1.222	0.176	0.160	0.182
Mn	0.175	0.144	0.151	0.162	0.098	0.098	0.086	0.230	0.237	0.236	0.067	0.086	0.076
Fe	1.684	1.566	1.567	1.569	2.186	2.173	2.139	1.352	1.339	1.342	2.216	2.209	2.214
Na	0.005	0.001	0.000	0.005	-	-	-	0.004	0.008	0.006	0.005	0.004	0.010
K	-	0.003	-	0.001	-	-	-	0.001	0.002	0.003	0.001	-	0.002
Wt% Total	101.34	101.25	101.64	101.71	101.09	100.65	100.17	100.74	99.91	100.30	100.76	101.34	101.08
Alm	0.561	0.519	0.518	0.521	0.718	0.713	0.713	0.445	0.441	0.441	0.727	0.724	0.722
Grs	0.191	0.258	0.258	0.248	0.076	0.079	0.079	0.401	0.405	0.402	0.058	0.052	0.059
Prp	0.189	0.175	0.175	0.177	0.174	0.176	0.179	0.079	0.076	0.080	0.194	0.195	0.193
Sps	0.058	0.048	0.050	0.054	0.032	0.032	0.029	0.076	0.078	0.078	0.022	0.028	0.025
Fe/(Fe+Mg)	0.748	0.748	0.747	0.746	0.805	0.802	0.799	0.850	0.853	0.846	0.789	0.788	0.789

Cations are normalized to an anhydrous basis of 12 oxygens.

Plagioclase

Sample	15a	15a	15a	15a	15c	15c	15c	15c	33a	33a	33a	33b	33b	33b
Analysis	191	194	198	199	25	26	44	45	48	50	52	266	267	269
X_{An}(%)	27.3	29.0	27.4	26.6	13.9	14.2	14.8	14.6	26.6	25.7	25.0	9.7	9.4	10.0
Wt% Total	99.76	99.76	101.30	101.64	99.00	99.16	98.52	98.69	100.50	100.72	100.96	100.97	100.83	99.95

Table 4.5 Continued.
Other Major Silicate Minerals

Sample	15a	15a	15a	15a	15a	15a	15a	15c	15c	15c	15c
Mineral	Bt	Bt	Bt	Bt	Hbl	Hbl	Hbl	Bt	Bt	Bt	Bt
Analysis	235	236	237	242	295	296	297	20	21	23	37
Si	2.790	2.777	2.808	2.805	6.328	6.433	6.364	2.763	2.789	2.803	2.783
Ti	0.070	0.066	0.081	0.049	0.082	0.061	0.072	0.090	0.095	0.094	0.110
Al	1.524	1.505	1.470	1.530	2.694	2.612	2.624	1.636	1.678	1.574	1.612
Mg	1.801	1.827	1.789	1.790	2.581	2.633	2.638	1.321	1.253	1.338	1.304
Ca	-	0.001	0.003	0.003	1.784	1.704	1.785	-	0.006	0.003	-
Mn	0.003	0.003	0.006	0.006	0.021	0.019	0.025	0.003	0.000	-	-
Fe	0.766	0.804	0.791	0.768	1.412	1.416	1.416	1.060	0.993	1.051	1.032
Na	0.070	0.055	0.045	0.056	0.547	0.563	0.563	0.058	0.063	0.041	0.047
K	0.783	0.786	0.816	0.802	0.137	0.081	0.096	0.853	0.866	0.864	0.876
Wt% Total	93.03	92.91	93.13	92.73	97.20	96.60	97.03	94.79	93.06	93.11	94.14
Fe/(Fe+Mg)	0.298	0.305	0.306	0.300	0.354	0.350	0.349	0.445	0.442	0.440	0.442

Sample	15c	15c	33a	33a	33a	33a	33b	33b	33b	33b
Mineral	Ms	Ms	Bt	Bt	Bt	Ms	Bt	Bt	Bt	Ms
Analysis	40	42	42	43	46	45	246	253	255	285
Si	3.091	3.093	2.797	2.791	2.767	3.162	2.759	2.760	2.752	3.110
Ti	0.044	0.037	0.152	0.143	0.139	0.035	0.097	0.086	0.094	0.046
Al	2.690	2.714	1.566	1.567	1.589	2.532	1.600	1.618	1.570	2.666
Mg	0.113	0.098	1.225	1.243	1.250	0.203	1.410	1.438	1.441	0.128
Ca	0.002	-	0.001	0.009	0.000	0.001	-	-	0.002	0.002
Mn	0.000	-	0.014	0.015	0.017	0.001	0.005	0.001	0.004	0.000
Fe	0.079	0.081	1.053	1.052	1.067	0.117	1.026	1.000	1.054	0.077
Na	0.232	0.231	0.021	0.034	0.023	0.048	0.055	0.036	0.047	0.232
K	0.769	0.746	0.901	0.889	0.918	0.924	0.839	0.855	0.855	0.730
Wt% Total	94.32	95.02	94.85	93.26	94.31	93.26	94.05	93.88	93.14	93.39
Fe/(Fe+Mg)	0.412	0.450	0.462	0.458	0.460	0.366	0.421	0.410	0.422	0.375

Cations normalized to an anhydrous 11 (biotite and muscovite) or 23 (hornblende) oxygens

Table 4.6 Mineral Compositions of Rocks from the Greater Himalayan Sequence Formation 1b.

Garnet

Sample	16a	16a	16a	16b	16b	17b	17b	17b	18b	18b	18b	18d	18d	18d	19c	19c	19c
Garnet	2	2	2	2	2	1	1	1	1	1	1	1	1	1	1	1	1
Traverse	1	1	1	1	1	1	1	1	1	1	1	1	1	1	1	1	1
Analysis	3	4	5	7	9	16	18	22	14	16	56	22	23	32	51	54	57
Si	3.009	2.985	2.992	2.971	2.968	2.958	2.942	2.928	2.954	2.956	2.943	2.913	2.934	2.910	2.920	2.921	2.918
Ti	0.000	0.001	0.000	0.002	0.002	-	0.000	0.000	0.001	0.000	0.001	-	-	-	0.000	0.001	-
Al	2.003	2.009	2.000	2.053	2.061	2.069	2.049	2.048	2.047	2.041	2.047	2.072	2.059	2.080	2.082	2.056	2.060
Mg	0.651	0.650	0.650	0.691	0.694	0.607	0.611	0.622	0.492	0.502	0.493	0.686	0.684	0.683	0.690	0.692	0.695
Ca	0.187	0.184	0.181	0.183	0.183	0.329	0.341	0.332	0.434	0.410	0.437	0.122	0.123	0.130	0.168	0.170	0.158
Mn	0.165	0.173	0.178	0.055	0.060	0.131	0.131	0.128	0.149	0.158	0.165	0.095	0.094	0.092	0.096	0.098	0.095
Fe	1.964	1.997	2.000	2.045	2.030	1.909	1.952	1.984	1.941	1.953	1.945	2.162	2.140	2.154	2.082	2.111	2.122
Na	0.018	0.018	0.011	0.001	0.003	0.009	0.010	0.010	0.006	0.005	0.004	0.001	0.004	0.003	0.003	0.001	0.006
K	0.003	0.003	0.002	0.002	0.001	-	0.001	-	-	0.001	0.001	-	0.001	0.001	0.001	0.001	-
Wt%																	
Total	100.23	102.25	101.39	99.48	99.52	101.62	100.17	100.00	100.57	100.46	100.16	99.22	98.54	99.11	98.32	98.55	98.74
Alm	0.662	0.665	0.665	0.688	0.684	0.641	0.643	0.647	0.644	0.646	0.640	0.706	0.704	0.704	0.686	0.687	0.691
Grs	0.063	0.061	0.060	0.061	0.062	0.111	0.112	0.108	0.144	0.136	0.144	0.040	0.041	0.043	0.055	0.055	0.051
Prp	0.219	0.216	0.216	0.232	0.234	0.204	0.201	0.203	0.163	0.166	0.162	0.224	0.225	0.223	0.227	0.225	0.226
Sps	0.056	0.058	0.059	0.019	0.020	0.044	0.043	0.042	0.049	0.052	0.054	0.031	0.031	0.030	0.032	0.032	0.031
Fe/(Fe+Mg)	0.751	0.754	0.755	0.747	0.745	0.759	0.762	0.761	0.798	0.795	0.798	0.759	0.758	0.759	0.751	0.753	0.753

Cations are normalized to an anhydrous basis of 12 oxygens.

Plagioclase

Sample	16a	16a	16a	16b	16b	16b	17b	17b	17b	18b	18b	18d	18d	18d	19c	19c	19c
Analysis	3	6	7	56	131	136	15	17	18	30	35	66	68	72	84	92	93
X_{An}(%)	12.2	14.1	12.3	12.3	12.5	13.3	20.3	19.3	20.7	30.4	28.3	14.0	15.4	13.6	17.2	15.9	16.9
Wt%																	
Total	100.55	99.65	100.83	100.94	101.03	100.69	99.67	99.19	100.85	100.60	100.95	98.90	99.50	99.39	100.73	100.96	101.01

Table 4.6. Continued
Other Major Silicate Minerals

Sample	16a	16a	16a	16a	16a	16b	16b	16b	16b	16b	16b	17b	17b	17b	17b	17b
Mineral	Bt	Bt	Bt	Ms	Par	Bt	Bt	Bt	Bt	Ms	Par	Bt	Bt	Bt	Ms	Ms
Analysis	11	15	20	17	19	39*	47*	101*	107*	123	42	3	13	57	6	56
Si	2.794	2.814	2.799	3.107	2.994	2.789	2.783	2.768	2.776	2.903	2.942	2.735	2.755	2.775	3.063	3.102
Ti	0.093	0.090	0.088	0.031	0.011	0.078	0.096	0.056	0.084	0.081	0.013	0.107	0.116	0.117	0.024	0.041
Al	1.564	1.561	1.583	2.659	2.937	1.645	1.637	1.633	1.656	2.299	3.021	1.662	1.684	1.625	2.771	2.698
Mg	1.386	1.393	1.385	0.094	0.011	1.421	1.402	1.456	1.456	0.580	0.016	1.398	1.355	1.372	0.115	0.114
Ca	0.001	-	0.002	0.001	0.020	0.002	0.002	0.004	0.001	0.016	0.017	0.007	0.002	0.001	0.001	-
Mn	0.005	0.002	0.004	-	0.000	0.006	0.003	0.008	0.004	0.004	0.000	0.004	0.005	0.003	0.002	-
Fe	1.027	0.996	1.003	0.146	0.050	0.944	0.952	1.029	0.979	0.514	0.039	0.959	0.934	0.950	0.074	0.068
Na	0.045	0.042	0.047	0.331	0.894	0.046	0.041	0.026	0.039	0.402	0.810	0.033	0.027	0.036	0.124	0.113
K	0.879	0.874	0.868	0.659	0.108	0.853	0.866	0.761	0.847	0.539	0.161	0.876	0.848	0.868	0.834	0.857
Wt% Total	94.83	94.76	94.89	95.04	95.41	94.19	93.37	93.55	93.92	94.01	94.95	93.47	93.32	93.81	93.16	93.22
Fe/(Fe+Mg)	0.426	0.417	0.420	0.607	0.816	0.399	0.404	0.414	0.402	0.470	0.712	0.407	0.408	0.409	0.393	0.373
Original Bt																
Fe/(Fe+Mg)						0.417	0.422	0.430	0.419							

Sample	18b	18b	18b	18b	18d	18d	18d	18d	18d	19c	19c	19c	19c	19c	19c
Mineral	Bt	Bt	Bt	Ms	Bt	Bt	Bt	Ms	Ms	Bt	Bt	Bt	Bt	Ms	Ms
Analysis	21*	23*	26*	22	42*	44*	45*	46	69	39*	40*	82*	83*	77	81
Si	2.775	2.759	2.770	3.076	2.767	2.766	2.758	3.088	3.114	2.726	2.727	2.761	2.774	3.132	3.102
Ti	0.145	0.150	0.158	0.059	0.175	0.153	0.151	0.041	0.025	0.124	0.119	0.121	0.115	0.062	0.061
Al	1.615	1.625	1.619	2.705	1.586	1.607	1.631	2.744	2.770	1.669	1.683	1.678	1.637	2.674	2.679
Mg	1.245	1.243	1.238	0.120	1.310	1.320	1.317	0.083	0.076	1.350	1.333	1.297	1.327	0.104	0.114
Ca	0.008	0.005	0.001	0.002	-	-	0.000	-	-	0.001	0.001	0.002	0.002	0.002	0.002
Mn	0.002	0.004	0.004	0.000	0.002	-	0.001	-	0.002	0.000	0.005	0.007	0.002	0.000	0.000
Fe	1.045	1.053	1.031	0.076	0.993	0.998	0.984	0.062	0.057	1.001	0.994	0.982	1.013	0.056	0.064
Na	0.032	0.034	0.024	0.120	0.055	0.056	0.065	0.255	0.161	0.043	0.050	0.044	0.039	0.161	0.168
K	0.857	0.860	0.869	0.828	0.823	0.824	0.809	0.706	0.705	0.867	0.864	0.828	0.817	0.759	0.805
Wt% Total	94.07	94.71	94.30	94.51	94.06	93.26	93.92	94.19	93.83	94.90	95.13	95.48	95.46	94.98	94.19
Fe/(Fe+Mg)	0.456	0.459	0.454	0.390	0.431	0.431	0.428	0.425	0.425	0.426	0.427	0.431	0.433	0.399	0.382
Original Bt															
Fe/(Fe+Mg)	0.460	0.462	0.458		0.436	0.436	0.433			0.430	0.431	0.437	0.435		

Cations normalized to an anhydrous 11 oxygens
* Biotite composition corrected for ReNTR's

Table 4.7 Mineral Compositions of Rocks from the Greater Himalayan Sequence Formation 1c.

Garnet

Sample	20a	20a	20a	20c	20c	20c	20c	32	32	32	32	23	23	23	24a	24a	24a
Garnet	2	2	2	2	2	2	2	1	1	1	2	1	1	1	1	1	1
Traverse	1	1	1	1	1	1	1	1	1	1	1	1	1	1	1	1	1
Analysis	86	89	90	15	16	31	35	29	68	31	86	22	23	25	25	26	27
Si	2.972	2.978	2.901	2.924	2.926	2.956	2.954	2.969	2.936	2.934	2.940	2.912	2.908	2.919	2.942	2.954	2.950
Ti	-	-	-	0.000	0.000	0.001	-	-	0.001	0.000	-	0.001	0.001	0.001	0.001	0.001	0.001
Al	2.068	2.064	2.131	2.028	2.027	2.045	2.040	2.037	2.068	2.056	2.044	2.059	2.072	2.069	2.053	2.050	2.049
Mg	1.004	1.011	1.039	0.669	0.670	0.663	0.661	0.882	0.894	0.905	0.907	0.495	0.497	0.497	0.517	0.511	0.517
Ca	0.103	0.091	0.087	0.252	0.258	0.213	0.216	0.152	0.142	0.153	0.148	0.419	0.410	0.400	0.471	0.470	0.473
Mn	0.035	0.038	0.036	0.123	0.114	0.112	0.111	0.055	0.055	0.054	0.059	0.154	0.154	0.157	0.174	0.174	0.167
Fe	1.808	1.803	1.830	2.066	2.065	2.028	2.040	1.917	1.928	1.936	1.938	2.017	2.013	2.001	1.873	1.860	1.868
Na	0.009	0.008	0.018	0.002	-	0.005	0.005	0.001	0.009	-	-	0.001	0.001	0.002	0.000	0.002	-
K	0.001	0.001	0.002	0.002	-	0.001	-	-	-	0.001	0.002	-	0.002	0.000	-	0.000	0.000
Wt%																	
Total	101.24	101.76	100.00	98.61	98.64	99.97	99.90	99.18	99.28	99.03	99.22	98.61	99.04	98.69	99.86	99.98	99.84
Alm	0.613	0.613	0.612	0.664	0.665	0.672	0.674	0.638	0.639	0.635	0.635	0.654	0.655	0.655	0.617	0.617	0.617
Grs	0.035	0.031	0.029	0.081	0.083	0.071	0.071	0.051	0.047	0.050	0.048	0.136	0.133	0.131	0.155	0.156	0.156
Prp	0.340	0.344	0.347	0.215	0.215	0.220	0.218	0.293	0.296	0.297	0.297	0.160	0.162	0.163	0.170	0.170	0.171
Sps	0.012	0.013	0.012	0.039	0.037	0.037	0.037	0.018	0.018	0.018	0.019	0.050	0.050	0.051	0.057	0.058	0.055
Fe/ (Fe+Mg)	0.643	0.641	0.638	0.755	0.755	0.754	0.755	0.685	0.683	0.681	0.681	0.803	0.802	0.801	0.784	0.784	0.783

Cations are normalized to an anhydrous basis of 12 oxygens.

Plagioclase

Sample	20a	20a	20a	20c	20c	20c	32	32	23	23	24a	24a	24a	24a
Analysis	31	32	33	69	73	44	46	23	23	33	14	15	16	18
X_{An}(%)	16.5	16.9	17.3	22.5	23.6	18.9	20.0	27.0	28.8	27.2	33.7	34.2	35.0	33.3
Wt% Total	99.80	100.77	100.21	100.36	100.74	99.05	98.55	98.12	99.18	99.26	100.60	100.01	100.63	99.90

Table 4.7. Continued
Other Major Silicate Minerals

Sample	20a	20a	20a	20a	20c	20c	20c	20c	20c	32	32	32
Mineral	Bt	Bt	Bt	Bt	Bt	Bt	Bt	Ms	Ms	Bt	Bt	Bt
Analysis	25*	27*	28*	29*	54*	60*	61*	59	62	38*	41*	51*
Si	2.641	2.802	2.803	2.779	2.731	2.730	2.746	3.105	3.085	2.715	2.745	2.738
Ti	0.060	0.090	0.082	0.074	0.162	0.169	0.138	0.071	0.066	0.105	0.128	0.119
Al	1.728	1.591	1.593	1.579	1.668	1.656	1.652	2.647	2.681	1.709	1.686	1.664
Mg	1.800	1.607	1.631	1.689	1.304	1.278	1.337	0.129	0.127	1.505	1.448	1.499
Ca	0.007	0.001	0.008	0.017	0.002	0.015	0.002	0.001	0.001	0.001	-	0.000
Mn	0.004	0.001	0.004	0.004	0.000	0.005	0.004	-	-	0.001	0.004	0.004
Fe	0.885	0.797	0.819	0.856	1.001	0.958	0.998	0.071	0.070	0.851	0.824	0.841
Na	0.047	0.078	0.073	0.059	0.052	0.061	0.041	0.133	0.141	0.069	0.060	0.059
K	0.589	0.787	0.745	0.714	0.842	0.819	0.857	0.817	0.820	0.789	0.835	0.854
Wt% Total	93.27	95.33	93.80	93.40	95.13	93.69	93.53	94.58	94.77	93.28	93.38	94.40
Fe/(Fe+Mg)	0.330	0.332	0.334	0.336	0.434	0.428	0.428	0.356	0.353	0.361	0.363	0.359
Original												
Fe/(Fe+Mg)	0.337	0.340	0.343	0.344	0.457	0.451	0.450			0.369	0.371	0.368

Sample	23	23	23	23	24a	24a	24a	24a	24a	24a
Mineral	Bt	Bt	Bt	Ms	Bt	Bt	Bt	Bt	Ms	Ms
Analysis	10*	12*	13*	2	3*	5*	9*	12*	7	11
Si	2.711	2.707	2.706	3.130	2.717	2.720	2.757	2.720	3.070	3.084
Ti	0.193	0.187	0.181	0.053	0.155	0.156	0.137	0.143	0.039	0.034
Al	1.643	1.660	1.664	2.628	1.650	1.700	1.654	1.700	2.724	2.723
Mg	1.162	1.149	1.135	0.126	1.250	1.205	1.234	1.214	0.118	0.115
Ca	0.000	0.003	0.003	0.002	-	0.001	0.004	0.002	0.001	0.004
Mn	0.004	0.008	0.005	0.002	0.006	0.007	0.008	0.009	-	0.002
Fe	1.107	1.107	1.103	0.107	1.050	1.011	1.024	1.025	0.081	0.076
Na	0.016	0.035	0.027	0.049	0.018	0.021	0.017	0.028	0.061	0.060
K	0.933	0.930	0.911	0.864	0.931	0.930	0.916	0.926	0.930	0.907
Wt% Total	93.23	93.24	93.90	94.03	94.05	94.84	94.18	93.29	94.18	93.66
Fe/(Fe+Mg)	0.488	0.491	0.493	0.459	0.457	0.456	0.453	0.458	0.406	0.397
Original										
Fe/(Fe+Mg)	0.507	0.510	0.512	0.461	0.461	0.461	0.459	0.463		

Cations normalized to an anhydrous 11 oxygens
* Biotite composition corrected for ReNTR's

Table 4.8 Mineral Compositions of Rocks from GHS Formation III.

Garnet

Sample	25a	25a	25a
Garnet	2	2	2
Traverse	1	1	1
Analysis	14	16	18
Si	2.970	2.973	2.967
Ti	-	-	0.002
Al	2.013	2.013	2.016
Mg	0.285	0.280	0.278
Ca	0.305	0.333	0.362
Mn	0.327	0.319	0.325
Fe	2.119	2.098	2.068
Na	0.009	0.010	0.006
K	0.000	0.000	0.002
Wt% Total	99.39	99.24	99.10
Alm	0.698	0.693	0.682
Grs	0.100	0.110	0.119
Prp	0.094	0.092	0.092
Sps	0.108	0.105	0.107
Fe/(Fe+Mg)	0.881	0.882	0.881

Cations are normalized to an anhydrous basis of 12 oxygens.

Plagioclase

Sample	25a	25a	25a	25a
Analysis	318	319	321	322
X_{An}(%)	16.6	16.2	16.8	17.5
Wt% Total	100.22	101.60	100.30	101.38

Other Major Silicate Minerals

Sample	25a	25a	25a	25a	25a	25a	25a	25a
Mineral	Bt	Bt	Bt	Bt	Ms	Ms	Ksp	Ksp
Analysis	304*	305*	310*	311*	309	313	324	327
Si	2.721	2.711	2.730	2.709	3.117	3.126	2.973	2.973
Ti	0.146	0.194	0.175	0.197	0.051	0.052	-	-
Al	1.596	1.545	1.559	1.582	2.616	2.602	1.041	1.040
Mg	0.855	0.857	0.861	0.844	0.100	0.109	-	-
Ca	0.001	-	0.000	0.004	0.000	0.000	0.002	0.003
Mn	0.015	0.017	0.012	0.013	0.001	0.001	-	-
Fe	1.507	1.507	1.503	1.475	0.136	0.133	0.000	-
Na	0.002	0.015	0.006	0.004	0.053	0.054	0.094	0.089
K	0.965	0.961	0.969	0.963	0.953	0.944	0.886	0.893
Wt% Total	94.40	95.98	94.43	94.96	93.23	93.17	100.16	100.30
Fe/(Fe+Mg)	0.638	0.637	0.636	0.636	0.576	0.549		
Original Bt Fe/(Fe+Mg)	0.646	0.645	0.644	0.644				

Cations normalized to an anhydrous 11 (biotite and muscovite) or 8 (K-Feldspar) oxygens

* Biotite composition corrected for ReNTR's

Table 4.9 Thermobarometric Results from Rocks Along the Modi Khola.

Sample	T (°C)	P (kbar)
GHS Fm II (MCT)		
AS01-25a	775 ± 20*	14.0 ± 1.0*
Average	*775*	*14.0*
GHS Fm Ic (MCT)		
AS01-24a	775 ± 20*	13.0 ± 0.5*
AS01-23	780 ± 20*	13.0 ± 0.5*
AS01-32	765 ± 20*	12.0 ± 0.5*
AS01-20c	765 ± 30*	12.5 ± 0.5*
AS01-20a	775 ± 20*	11.5 ± 0.5*
Average	*775*	*12.5*
GHS Fm Ib (MCT)		
AS01-19c	745 ± 20*	11.5 ± 0.5*
AS01-18d	725 ± 20*	11.5 ± 1.0*
AS01-18b	740 ± 20*	12.0 ± 0.5*
AS01-17b	735 ± 20	13.5 ± 0.5
AS01-16b	725 ± 20*	13.0 ± 0.5*
AS01-16a	740 ± 30	12.5 ± 1.0
Average	*735*	*12.5*
GHS Fm Ia (MCT)		
AS01-33b	650 ± 20	11.5 ± 1.0
AS01-33a	645 ± 20	12.0 ± 0.5
AS01-15c	670 ± 30	11.5 ± 0.5
AS01-15a	625 ± 40	12.0 ± 1.0
Average	*650*	*12.0*
LHS (MT)		
AS01-36b	575 ± 20	11.5 ± 0.5
AS01-36a	545 ± 20	10.0 ± 0.5
AS01-38b	550 ± 30	10.5 ± 1.0
Average	*555*	*10.5*
LHS (LHD)		
AS01-40e	515 ± 30	7.0 ± 1.0
AS01-41b	530 ± 50[a]	
AS01-43a	530 ± 50[a]	
AS01-44a	500 ± 20	7.0 ± 0.5
AS01-45a	505 ± 20	8.5 ± 1.0
AS01-46	510 ± 30	8.0 ± 0.5
Average	*515*	*7.5*

Note: All temperatures and associated errors rounded to nearest 5°C, pressures and associated errors to 0.5 kbar. All temperatures calculated via garnet-biotite thermometry except AS01-41b, which was calculated via garnet-chlorite thermometry. Pressures calculated from garnet-plagioclase-muscovite-biotite, garnet-plagioclase-kyanite-quartz, and garnet-plagioclase-biotite-quartz barometry.
a: T calculated at an assumed pressure of 8 ± 1 kbar.
*Biotite corrected for ReNTRs

Table 4.10 Electron Microprobe Chemical Analysis of Monazite from Sample AS01-16a.

mnz #	1	1	1	1	3	3	3	3	4	4	4	4	4	5	5	5	5
Analysis	44	45	46	47	51	52	54	55	56	58	59	60	62	63	64	65	66
SiO_2	0.38	0.38	0.25	0.32	0.29	0.40	0.27	0.43	0.24	0.29	0.20	0.33	0.44	1.35	0.28	0.30	0.40
P_2O_5	30.09	30.28	30.34	30.41	29.69	30.06	29.75	30.27	29.99	30.04	30.21	30.08	30.00	28.45	30.04	29.89	29.73
SO_3	0.71	0.77	0.79	0.44	0.85	0.65	0.90	0.29	0.84	0.73	0.98	0.74	0.59	0.47	0.54	0.80	0.70
CaO	2.01	1.94	1.51	1.63	1.60	1.94	1.62	1.30	1.52	1.71	1.58	1.94	2.08	1.59	1.30	1.79	2.09
Y_2O_3	2.59	2.57	2.11	2.53	2.11	2.82	2.10	2.57	1.52	2.02	1.81	2.04	2.12	0.65	1.56	1.87	2.25
La_2O_3	12.23	12.32	15.00	13.21	14.51	11.81	14.43	12.20	15.35	13.31	14.64	12.94	14.03	13.81	14.48	13.64	12.01
Ce_2O_3	25.84	26.26	28.50	27.00	27.73	25.24	28.31	26.78	29.13	27.38	28.28	26.82	25.85	27.59	28.68	27.33	25.67
Pr_2O_3	2.84	2.91	3.02	2.96	2.97	3.05	2.99	3.08	2.92	2.94	3.09	2.91	2.58	2.96	3.05	2.91	2.98
Nd_2O_3	11.28	11.59	10.97	11.13	11.10	11.90	11.13	11.84	11.10	11.41	11.24	11.13	10.19	11.02	11.66	11.59	11.23
Sm_2O_3	1.88	2.00	1.69	1.94	1.86	2.11	1.72	2.18	1.76	1.86	1.83	2.03	1.63	1.79	1.96	2.01	2.03
Gd_2O_3	1.68	1.73	1.42	1.63	1.41	1.73	1.48	1.97	1.44	1.63	1.72	1.79	1.70	1.33	1.51	1.65	1.80
Tb_2O_3	0.12	0.11	0.09	0.16	0.16	0.16	0.14	0.05	0.04	0.13	0.17	0.16	0.13	0.08	0.16	0.14	0.12
Dy_2O_3	0.75	0.72	0.60	0.72	0.61	0.88	0.61	0.85	0.53	0.65	0.71	0.69	0.71	0.35	0.55	0.65	0.74
ThO_2	7.11	6.51	4.11	6.11	4.26	7.18	4.22	5.31	3.68	5.20	3.22	6.55	8.12	5.59	4.18	5.41	7.54
UO_2	1.03	0.86	0.57	0.82	0.55	1.01	0.52	0.71	0.49	0.80	0.63	0.94	0.80	0.69	0.60	0.77	1.00
PbO	0.02	0.02	0.02	0.02	0.02	0.01	0.01	0.01	0.01	0.02	0.01	0.01	0.02	0.01	0.01	0.01	0.02
Total	100.57	100.96	100.98	101.03	99.66	100.95	100.20	99.85	100.56	100.11	100.31	101.10	100.99	97.72	100.56	100.76	100.32
Si	0.0144	0.0142	0.0097	0.0123	0.0111	0.0153	0.0102	0.0167	0.0091	0.0110	0.0075	0.0126	0.0168	0.0533	0.0107	0.0113	0.0153
P	0.9723	0.9725	0.9750	0.9815	0.9682	0.9708	0.9662	0.9870	0.9715	0.9756	0.9740	0.9709	0.9709	0.9526	0.9784	0.9686	0.9683
S	0.0203	0.0218	0.0225	0.0125	0.0246	0.0185	0.0258	0.0083	0.0241	0.0210	0.0279	0.0210	0.0168	0.0138	0.0156	0.0231	0.0202
Ca	0.0822	0.0787	0.0615	0.0664	0.0661	0.0792	0.0667	0.0537	0.0624	0.0702	0.0643	0.0794	0.0852	0.0672	0.0534	0.0736	0.0862
Y	0.0527	0.0520	0.0426	0.0513	0.0432	0.0571	0.0428	0.0526	0.0311	0.0412	0.0366	0.0414	0.0431	0.0137	0.0319	0.0380	0.0461
La	0.1722	0.1724	0.2100	0.1858	0.2062	0.1661	0.2042	0.1734	0.2166	0.1884	0.2056	0.1819	0.1978	0.2014	0.2055	0.1926	0.1703
Ce	0.3610	0.3647	0.3961	0.3769	0.3910	0.3525	0.3976	0.3777	0.4081	0.3845	0.3944	0.3743	0.3618	0.3995	0.4040	0.3830	0.3615
Pr	0.0395	0.0402	0.0418	0.0412	0.0417	0.0424	0.0418	0.0432	0.0407	0.0411	0.0429	0.0404	0.0360	0.0427	0.0428	0.0406	0.0418
Nd	0.1538	0.1571	0.1487	0.1515	0.1527	0.1621	0.1525	0.1629	0.1518	0.1563	0.1529	0.1515	0.1391	0.1556	0.1603	0.1585	0.1542
Sm	0.0248	0.0262	0.0221	0.0255	0.0247	0.0277	0.0227	0.0290	0.0231	0.0245	0.0240	0.0266	0.0215	0.0244	0.0259	0.0265	0.0269
Gd	0.0212	0.0218	0.0179	0.0206	0.0180	0.0219	0.0188	0.0251	0.0182	0.0208	0.0218	0.0226	0.0215	0.0175	0.0193	0.0209	0.0230
Tb	0.0015	0.0013	0.0011	0.0020	0.0021	0.0020	0.0018	0.0007	0.0005	0.0016	0.0021	0.0020	0.0017	0.0011	0.0020	0.0018	0.0016
Dy	0.0093	0.0088	0.0074	0.0089	0.0075	0.0108	0.0075	0.0106	0.0066	0.0080	0.0087	0.0085	0.0088	0.0044	0.0068	0.0080	0.0092
Th	0.0617	0.0562	0.0355	0.0530	0.0373	0.0624	0.0368	0.0465	0.0321	0.0453	0.0279	0.0568	0.0706	0.0503	0.0366	0.0472	0.0660
U	0.0087	0.0073	0.0048	0.0070	0.0047	0.0086	0.0045	0.0061	0.0042	0.0069	0.0053	0.0080	0.0068	0.0061	0.0052	0.0065	0.0086
Pb	0.0002	0.0002	0.0002	0.0002	0.0002	0.0001	0.0001	0.0001	0.0001	0.0002	0.0001	0.0001	0.0002	0.0001	0.0001	0.0001	0.0002

Table 4.11 Electron Microprobe Chemical Analysis of Monazite from Sample AS01-19c.

mnz # Analysis	3 21	2 19	2 18	2 17	2 16	2 15	2 14	2 13	2 12	1 10	1 9	1 7	1 6	1 5	1 4	1 3	1 1
SiO$_2$	0.26	0.26	0.25	0.50	0.52	0.26	0.26	0.35	0.24	0.46	0.26	0.37	0.39	0.24	0.25	0.42	0.25
P$_2$O$_5$	30.58	30.75	30.77	29.07	30.23	30.72	30.58	30.12	30.58	30.04	30.58	29.95	30.15	30.67	30.28	30.00	30.80
SO$_3$	0.01	0.00	0.01	0.04	0.01	0.02	0.01	0.02	0.01	0.01	0.01	0.01	0.01	0.01	0.01	0.01	0.01
CaO	1.30	1.25	1.34	1.19	1.53	1.31	1.29	1.01	1.30	1.17	1.22	1.19	1.18	1.30	1.25	1.10	1.31
Y$_2$O$_3$	2.85	2.57	2.81	0.50	0.61	2.27	2.24	0.48	2.84	0.45	2.69	0.45	0.55	2.23	2.39	0.47	2.69
La$_2$O$_3$	12.76	13.30	13.21	14.08	13.61	13.55	13.32	14.71	12.92	14.12	13.35	14.94	14.43	13.37	13.43	14.14	13.52
Ce$_2$O$_3$	26.94	27.12	27.05	28.95	27.82	27.84	27.49	29.54	27.18	29.36	27.38	29.62	29.49	27.81	27.53	29.76	27.50
Pr$_2$O$_3$	2.86	3.03	2.99	3.24	3.08	2.95	3.01	3.23	2.89	3.18	3.09	3.18	3.21	3.03	3.02	3.27	3.00
Nd$_2$O$_3$	11.48	11.51	11.30	11.92	11.49	11.19	11.69	12.06	11.42	12.12	11.36	11.64	11.98	11.49	11.54	11.90	11.64
Sm$_2$O$_3$	1.95	1.90	1.95	1.74	1.87	1.98	2.03	1.89	2.04	2.08	2.06	1.92	2.09	1.93	2.06	1.98	2.05
Gd$_2$O$_3$	1.88	1.72	1.83	1.24	1.30	1.75	1.80	1.20	1.99	1.36	1.83	1.21	1.26	1.71	1.74	1.17	1.95
Tb$_2$O$_3$	0.13	0.13	0.14	0.00	0.04	0.17	0.16	0.01	0.20	0.11	0.11	0.05	0.10	0.12	0.12	0.02	0.17
Dy$_2$O$_3$	0.85	0.79	0.86	0.21	0.25	0.72	0.74	0.18	0.88	0.17	0.88	0.13	0.20	0.71	0.72	0.19	0.78
ThO$_2$	5.21	5.12	5.41	5.77	7.95	5.78	5.64	5.09	5.12	6.27	5.01	5.48	5.99	5.64	5.35	5.75	5.36
UO$_2$	1.52	1.33	1.38	0.65	0.99	1.02	1.03	0.62	1.47	0.67	1.21	0.65	0.67	0.96	0.97	0.71	1.29
PbO	0.01	0.01	0.01	0.01	0.02	0.01	0.02	0.01	0.02	0.00	0.01	0.01	0.02	0.01	0.01	0.01	0.02
Total	100.59	100.79	101.30	99.11	101.30	101.52	101.30	100.50	101.08	101.56	101.07	100.79	101.72	101.22	100.69	100.91	102.36
Si	0.0099	0.0099	0.0095	0.0199	0.0199	0.0098	0.0099	0.0135	0.0093	0.0178	0.0101	0.0144	0.0150	0.0093	0.0097	0.0164	0.0096
P	0.9955	0.9980	0.9951	0.9777	0.9879	0.9942	0.9932	0.9922	0.9930	0.9843	0.9933	0.9870	0.9860	0.9951	0.9905	0.9873	0.9905
S	0.0003	0.0001	0.0004	0.0013	0.0002	0.0005	0.0004	0.0006	0.0004	0.0004	0.0004	0.0003	0.0004	0.0003	0.0003	0.0003	0.0003
Ca	0.0537	0.0513	0.0548	0.0506	0.0631	0.0537	0.0531	0.0421	0.0533	0.0484	0.0500	0.0494	0.0489	0.0536	0.0520	0.0460	0.0534
Y	0.0584	0.0525	0.0572	0.0105	0.0126	0.0461	0.0456	0.0099	0.0581	0.0092	0.0550	0.0093	0.0112	0.0456	0.0491	0.0097	0.0543
La	0.1810	0.1881	0.1861	0.2064	0.1937	0.1910	0.1885	0.2111	0.1828	0.2016	0.1889	0.2146	0.2056	0.1890	0.1914	0.2028	0.1894
Ce	0.3793	0.3806	0.3784	0.4212	0.3933	0.3897	0.3862	0.4207	0.3817	0.4160	0.3846	0.4222	0.4170	0.3902	0.3895	0.4236	0.3825
Pr	0.0400	0.0423	0.0416	0.0469	0.0433	0.0411	0.0421	0.0458	0.0403	0.0449	0.0432	0.0451	0.0452	0.0423	0.0426	0.0463	0.0415
Nd	0.1576	0.1575	0.1541	0.1691	0.1585	0.1527	0.1602	0.1676	0.1564	0.1675	0.1556	0.1618	0.1652	0.1573	0.1593	0.1651	0.1579
Sm	0.0259	0.0250	0.0257	0.0239	0.0248	0.0260	0.0268	0.0253	0.0269	0.0277	0.0272	0.0257	0.0279	0.0255	0.0275	0.0265	0.0268
Gd	0.0240	0.0218	0.0232	0.0164	0.0166	0.0222	0.0229	0.0155	0.0253	0.0174	0.0233	0.0157	0.0162	0.0217	0.0223	0.0150	0.0246
Tb	0.0016	0.0016	0.0017	0.0000	0.0005	0.0021	0.0020	0.0001	0.0025	0.0014	0.0014	0.0006	0.0013	0.0015	0.0016	0.0003	0.0021
Dy	0.0105	0.0098	0.0106	0.0026	0.0031	0.0089	0.0091	0.0023	0.0108	0.0021	0.0109	0.0016	0.0024	0.0087	0.0090	0.0024	0.0096
Th	0.0456	0.0447	0.0470	0.0522	0.0699	0.0503	0.0492	0.0451	0.0447	0.0552	0.0438	0.0486	0.0526	0.0492	0.0471	0.0509	0.0464
U	0.0130	0.0113	0.0117	0.0058	0.0085	0.0087	0.0088	0.0053	0.0125	0.0058	0.0104	0.0056	0.0058	0.0082	0.0083	0.0062	0.0109
Pb	0.0001	0.0001	0.0001	0.0001	0.0002	0.0001	0.0002	0.0001	0.0002	0.0000	0.0001	0.0001	0.0002	0.0001	0.0001	0.0001	0.0002

Table 4.11 Continued.

mnz #	3	3	3	3	4	4	4	4	4	5	5	5	5	5	5	5	5
Analysis	23	24	25	26	27	28	29	31	33	34	35	36	37	39	40	42	43
SiO$_2$	0.40	0.48	0.22	0.25	0.26	0.33	0.43	0.26	0.25	0.25	0.42	0.26	0.26	0.38	0.51	0.26	0.26
P$_2$O$_5$	30.00	29.98	30.49	30.22	30.87	30.38	30.37	30.60	30.63	30.55	30.29	30.67	30.37	30.39	29.94	30.62	30.65
SO$_3$	0.00	0.01	0.01	0.01	0.01	0.01	0.02	0.01	0.00	0.02	0.01	0.02	0.00	0.02	0.02	0.01	0.01
CaO	1.37	1.25	1.28	1.31	1.32	1.12	1.24	1.30	1.32	1.25	1.18	1.31	1.25	1.24	1.32	1.34	1.19
Y$_2$O$_3$	0.67	0.57	2.02	1.87	2.62	0.46	0.49	2.21	1.97	2.09	0.53	2.29	1.29	2.70	0.48	2.23	1.10
La$_2$O$_3$	13.57	14.18	13.54	13.28	12.85	14.16	13.90	13.44	13.24	13.58	14.58	13.68	13.24	12.78	14.56	13.35	13.49
Ce$_2$O$_3$	28.56	28.62	28.20	27.91	27.46	29.58	28.78	27.67	27.59	27.69	29.05	27.72	28.60	26.83	28.52	27.55	28.46
Pr$_2$O$_3$	2.97	3.08	2.97	2.94	2.86	3.18	3.08	2.95	3.02	3.03	3.14	2.87	3.11	2.95	2.91	3.03	3.20
Nd$_2$O$_3$	11.63	11.79	11.47	11.63	11.37	11.92	11.84	11.34	11.44	11.47	11.58	10.90	12.30	11.57	11.35	11.46	11.99
Sm$_2$O$_3$	2.05	1.92	1.95	2.08	1.98	1.99	2.02	2.00	2.10	1.97	1.78	1.90	2.19	2.02	1.68	1.98	2.13
Gd$_2$O$_3$	1.40	1.16	1.64	1.85	1.76	1.20	1.25	1.83	1.82	1.63	1.22	1.67	1.67	1.89	1.10	1.71	1.62
Tb$_2$O$_3$	0.05	0.02	0.12	0.12	0.11	0.04	-	0.18	0.22	0.12	-	0.12	0.12	0.11	0.02	0.14	0.06
Dy$_2$O$_3$	0.25	0.19	0.63	0.68	0.78	0.20	0.23	0.68	0.69	0.66	0.19	0.71	0.52	0.87	0.19	0.74	0.43
ThO$_2$	6.82	6.66	5.51	5.73	5.65	5.53	6.28	5.73	5.87	5.48	6.14	5.93	5.48	5.18	7.22	5.70	5.35
UO$_2$	0.95	0.80	0.97	0.93	1.16	0.66	0.86	1.02	0.96	0.94	0.75	0.90	0.89	1.12	0.75	1.01	0.84
PbO	0.01	0.02	0.01	0.01	0.02	0.01	0.01	0.01	0.01	0.01	0.01	0.01	0.01	0.01	0.01	0.01	0.01
Total	100.69	100.71	101.03	100.83	101.07	100.77	100.77	101.24	101.14	100.75	100.87	100.96	101.30	100.05	100.59	101.14	100.78
Si	0.0156	0.0186	0.0085	0.0096	0.0098	0.0128	0.0166	0.0100	0.0098	0.0097	0.0162	0.0098	0.0100	0.0145	0.0199	0.0101	0.0099
P	0.9883	0.9870	0.9940	0.9903	0.9984	0.9958	0.9944	0.9941	0.9957	0.9956	0.9924	0.9962	0.9919	0.9935	0.9867	0.9942	0.9999
S	0.0001	0.0004	0.0002	0.0003	0.0003	0.0004	0.0005	0.0002	0.0001	0.0006	0.0002	0.0005	0.0001	0.0006	0.0005	0.0003	0.0004
Ca	0.0571	0.0519	0.0526	0.0543	0.0541	0.0465	0.0514	0.0534	0.0543	0.0516	0.0491	0.0537	0.0516	0.0513	0.0549	0.0552	0.0490
Y	0.0140	0.0118	0.0415	0.0385	0.0533	0.0095	0.0101	0.0451	0.0403	0.0428	0.0109	0.0467	0.0265	0.0554	0.0100	0.0456	0.0225
La	0.1948	0.2034	0.1923	0.1896	0.1811	0.2022	0.1983	0.1902	0.1875	0.1929	0.2081	0.1936	0.1883	0.1821	0.2090	0.1889	0.1917
Ce	0.4069	0.4075	0.3976	0.3956	0.3842	0.4193	0.4074	0.3888	0.3878	0.3903	0.4117	0.3894	0.4039	0.3794	0.4064	0.3869	0.4014
Pr	0.0421	0.0436	0.0416	0.0414	0.0398	0.0448	0.0435	0.0412	0.0422	0.0425	0.0443	0.0401	0.0438	0.0416	0.0412	0.0423	0.0449
Nd	0.1617	0.1638	0.1577	0.1608	0.1551	0.1648	0.1635	0.1555	0.1569	0.1578	0.1600	0.1494	0.1695	0.1596	0.1578	0.1570	0.1650
Sm	0.0274	0.0258	0.0259	0.0278	0.0260	0.0266	0.0269	0.0264	0.0278	0.0261	0.0237	0.0252	0.0291	0.0269	0.0225	0.0262	0.0282
Gd	0.0180	0.0149	0.0210	0.0238	0.0222	0.0154	0.0160	0.0232	0.0232	0.0208	0.0156	0.0212	0.0214	0.0241	0.0142	0.0217	0.0207
Tb	0.0007	0.0002	0.0015	0.0016	0.0014	0.0006	-	0.0022	0.0027	0.0016	-	0.0015	0.0015	0.0013	0.0002	0.0017	0.0007
Dy	0.0031	0.0024	0.0078	0.0085	0.0096	0.0025	0.0028	0.0084	0.0086	0.0082	0.0023	0.0088	0.0064	0.0108	0.0024	0.0091	0.0053
Th	0.0604	0.0589	0.0483	0.0505	0.0491	0.0487	0.0552	0.0501	0.0513	0.0481	0.0541	0.0518	0.0481	0.0455	0.0639	0.0497	0.0469
U	0.0082	0.0069	0.0083	0.0080	0.0099	0.0057	0.0074	0.0087	0.0082	0.0081	0.0065	0.0077	0.0076	0.0096	0.0065	0.0087	0.0072
Pb	0.0001	0.0002	0.0001	0.0001	0.0002	0.0001	0.0001	0.0001	0.0001	0.0001	0.0001	0.0001	0.0001	0.0002	0.0001	0.0001	0.0001

Table 4.12 Ion Microprobe Age Analyses of Monazite

Sample	Age±2σ (Ma)	Comment	Sample	Age±2σ (Ma)	Comment
AS01-35			*AS01-19c*		
1-1	21.6 ± 2.6	low-Y	3-1	19.8 ± 1.0	intermediate-Y
AS01-15b			3-2	20.1 ± 0.9	low-Y
1-1	25.5 ± 2.1	mottled Y, Th	3-3	18.1 ± 0.9	high-Y rim
4-1	113.7 ± 5.5	mixed	3-4	20.9 ± 0.9	intermediate-Y
4-2	47.0 ± 2.1	mixed	3-5	19.3 ± 0.9	intermediate-Y
5-1	24.3 ± 1.3	mottled Y, Th	5-1	27.5 ± 1.1	low-Y
5-2	25.3 ± 1.5	mottled Y, Th	5-2	18.5 ± 0.8	high-Y rim
AS01-33b			5-3	22.9 ± 1.0	mixed date
1-1	21.7 ± 1.0	mottled Y, Th	5-4	20.8 ± 1.0	intermediate-Y
1-2	23.1 ± 1.3	mottled Y, Th	6-1*	16.9 ± 0.7	high-Y
4-1	22.1 ± 1.0	mottled Y, Th	6-2*	20.2 ± 0.4	low-Y core
4-2	22.6 ± 1.3	mottled Y, Th	7-1*	20.8 ± 0.7	intermediate-Y rim
5-1	21.3 ± 0.9	mottled Y, Th	7-2*	28.6 ± 0.8	low-Y core
5-2	22.0 ± 1.0	mottled Y, Th	7-3*	19.8 ± 0.9	high-Y rim
AS01-16a			*AS01-20a*		
1-2	25.9 ± 1.2	low-Y, Th core	1-1	21.7 ± 1.3	intermediate-Y
1-3	24.9 ± 1.3	intermediate-Y	1-2	26.8 ± 2.0	high-Y
3-1	25.7 ± 1.3	intermediate-Y	3-1	93.6 ± 4.7	inherited
3-2	18.7 ± 1.4	intermediate-Y	5-1	74.7 ± 3.3	inherited
3-3	25.3 ± 1.9	intermediate-Y	5-2	22.7 ± 1.0	mixed date
4-1	33.2 ± 2.0	low-Y, Th core	*AS01-22a*		
4-2	25.7 ± 1.5	intermediate-Y	1-1	178.9 ± 7.0	inherited
4-3	27.2 ± 1.5	low-Y, Th	3-1	20.9 ± 1.0	high-Y
*AS01-16b**			*AS01-32*		
1-1	20.3 ± 0.4	mottled Y, Th	1-1	29.3 ± 1.4	low-Y core
1-2	25.2 ± 0.4	mottled Y, Th	3-1	25.0 ± 1.2	mixed date
2-1	24.4 ± 0.4	mottled Y, Th	3-2	29.1 ± 1.4	low-Y core
2-2	27.0 ± 0.4	mottled Y, Th	4-1*	28.2 ± 0.4	mottled Y, Th
3-1	25.4 ± 0.3	mottled Y, Th	4-2*	28.7 ± 0.4	mottled Y, Th
3-2	19.8 ± 1.2	mottled Y, Th	4-3*	28.2 ± 0.4	mottled Y, Th
4-1	26.0 ± 0.4	mottled Y, Th	5-1*	31.9 ± 1.0	high-Y
4-2	25.9 ± 0.4	mottled Y, Th	5-2*	31.5 ± 0.8	high-Y
4-3	26.1 ± 0.3	mottled Y, Th	6-1*	29.7 ± 0.4	mottled Y, Th
AS01-17b			*AS01-23*		
2-1	17.9 ± 0.9	High-Y, Th	1-1	18.9 ± 1.0	high-Y rim
3-1	17.9 ± 1.8	High-Y, Th	1-2	23.1 ± 1.4	low-Y core
AS01-18d			1-3	20.5 ± 1.0	low-Y
1-1	25.6 ± 1.3	mixed date	1-4	20.5 ± 1.2	high-Y rim
1-2	25.1 ± 1.5	mixed date	2-1	20.0 ± 1.0	low-Y
1-3	27.7 ± 1.7	low-Y core	2-2	21.4 ± 1.0	low-Y
4-1	29.5 ± 1.3	low-Y core	5-1	20.3 ± 0.9	low-Y
4-2	21.3 ± 1.2	high-Y rim	5-2	20.3 ± 1.1	low-Y
4-3	19.7 ± 1.8	high-Y rim	*AS01-27*		
AS01-19c			1-1	32.7 ± 1.4	mottled Y, Th
1-1	19.0 ± 0.7	high-Y	1-2	30.2 ± 1.5	mottled Y, Th
1-2	18.7 ± 0.9	high-Y	3-1	36.7 ± 1.7	mottled Y, Th
1-3	28.4 ± 1.2	low-Y core	4-1	33.0 ± 1.5	mottled Y, Th
1-4	24.9 ± 1.0	mixed date	5-1*	37.4 ± 1.3	mottled Y, Th
2-1	27.4 ± 1.4	low-Y core	5-2*	34.2 ± 1.3	mottled Y, Th
2-2	18.7 ± 0.8	intermediate-Y	6-1*	37.8 ± 3.3	intermediate-Y
2-3	19.6 ± 1.1	intermediate-Y	6-2*	37.3 ± 3.0	intermediate-Y
			6-3*	37.2 ± 4.6	intermediate-Y
			6-4*	35.0 ± 4.0	low Y, Th rim

Note: All analyses contained 95% radiogenic 208Pb or higher
*Data from Kohn, 2005

Table 4.13 Estimates of Thrust Temperatures, Times, Minimum
Displacements and Displacement Rates.

Thrust	Peak T (°C)	t (Ma)	Cooling T (°C)	t (Ma)	Distance (km)	Rate (cm/yr)
Sinuwa	775±20	27±1	735±20	23±1	55	1.4±2.8
Bhanuwa	735±20	23±1	650±25	19±2	80	2.0±1.2
Main Central	650±25	22±1	400±25	15 ±1	130	1.9±0.5

CHAPTER 5. GEOCHRONOLOGY AND THERMOBAROMETRY OF THE

CENTRAL HIMALAYA, ARUN RIVER VALLEY, EASTERN NEPAL

5.1 Introduction

Although eclogites have been found in only a few localities in the Himalaya, they are key in understanding the orogen's metamorphic and tectonic evolution (Figure 5.1). In the northwest Himalaya, ultra-high pressure eclogites (UHP) have been documented in the Kaghan Valley of Pakistan (Pognante and Spencer, 1991; Tonarini et al., 1993) and the Tso Morari dome in the Ladakh region of India (de Sigoyer et al., 1997, 2000). In the central Himalaya, eclogites have been documented in the Ama Drime range in the Kharta region of Tibet (Lombardo and Rolfo, 2000; Groppo et al., 2007; Cottle et al., 2009), and the Makalu-Everest region of the Arun River valley in eastern Nepal (Parkinson and Kohn, 2002). Both NW Himalayan eclogite localities occur within the Greater Himalayan Sequence immediately south of the Indus Suture Zone (O'Brien et al., 2001), and are considered to indicate subduction of the leading edge of the Indian continental crust during the initial stages of Indo-Asian collision. These eclogites reached conditions of $725\pm25°C$ and 28-30 kbar (Mukherjee and Sachan, 2001; O'Brien et al., 2001). Accessory zircon (Kaneko et al., 2003; Parrish et al., 2006) and garnet (Tonarini et al., 1993), whose chemistry or texture link them to UHP metamorphism, have been directly dated at ~46 Ma in the Kaghan Valley, and a garnet isochron yields ~54 Ma for Tso Morari (de Sigoyer et al., 2000).

In contrast, eclogites in the central Himalaya do not appear to have attained

UHP conditions (Lombardo and Rolfo, 2000; Groppo et al., 2007) and direct correlations

with eclogites in the NW Himalaya are unclear. The Ama Drime eclogites occur north of

the Arun eclogite, up-drainage along the Arun/Phung Chu River within the Ama Drime

Massif. Both eclogite occurrences have been strongly overprinted by subsequent

metamorphism, leaving sparse evidence for eclogitization. Groppo et al. (2007) proposed

four phases of metamorphism for the Ama Drime eclogites on the basis of

microstructural observations, pseudosection analysis, and conventional thermobarometry:

an initial (M1) eclogitic metamorphism at >15 kbar and >580°C; a peak-T (M2)

granulite-facies event at 8-10 kbar and >750°C, and another (M3) at ~4 kbar and 750°C;

and a final cooling stage (M4) at ~700°C and 4 kbar. Attempts to date the Ama Drime

eclogites have yielded U-Pb SHRIMP ages of 13-14 Ma from low-U rims of zircon, the

growth of which was assumed to result from reactions occurring during the "M3" low-P

granulitic event (Groppo et al., 2007). Cottle et al. (2009) present monazite and xenotime

ages of 13.2 ± 1.4 Ma that they interpret to constrain the timing of peak (M2) granulite

metamorphism. Other published ages include zircon $^{206}Pb/^{238}U$ ages of 17.6±0.3 Ma,

interpreted to represent granulite metamorphism in the northern Ama Drime Range (Li et

al., 2003). In sum, all these ages are thought to reflect the granulite-facies overprint, not

the age of eclogitization.

In this chapter, we use Lu-Hf dating techniques on garnet, an eclogite-facies

mineral, to provide the first direct measurement of the timing of eclogitization in the

central Himalaya, as garnet growth would have been initiated during the prograde

transition to eclogite facies. The timing of this event is then interpreted in the context

of models of Indo-Asian collision and Himalayan tectonics.

5.2 Petrology

Samples from both the LHS and GHS were collected in eastern Nepal along the

west side of the Arun River (Figure 5.2). The metabasites occur as decimeter- to meter-

scale boudinaged sills and small bodies within the surrounding felsic schist and gneiss,

similar to those documented by Cottle et al. (2009) along strike in southern Tibet.

Amphibolite samples were collected from LHS (meta)basaltic sills that are structurally

continuous with the surrounding schists and gneisses. The granulitized eclogites from the

GHS Barun Gneiss were collected from the core of a ~3 meter diameter boudinaged sill.

All field documentation, that is photographs, field notes, and GPS points, were lost

during the Hurricane Katrina disaster.

Samples of the GHS Barun Gneiss (AR01-43c and AR01-43e) from this study are

similar to the granulitized eclogites described previously from the Ama Drime massif

(Lombardo and Rolfo, 2000; Groppo et al., 2007; Cottle et al., 2009). These internally

undeformed, medium-grained rocks contain garnet, clinopyroxene, plagioclase,

amphibole, quartz, trace orthopyroxene (in AR01-43c only), biotite, scapolite, calcite,

ilmenite, titanite, zircon, and apatite (Figure 5.3-5.4). The high-calcium bulk composition

of these rocks stabilizes titanite as the primary titanium-bearing phase rather than rutile,

which is typically assumed to be the higher-P phase. Direct evidence for eclogitization

was all but eliminated during subsequent metamorphism. Calcium-rich (~30% grossular)

cores of large garnet are the only direct record of the prograde eclogitic assemblage, and

were overgrown by thin rims during the later thermal peak of metamorphism (Figure 5.5). True omphacite is not preserved in the matrix or as inclusions in garnet, although sparse inclusions of relatively sodic clinopyroxene (up to 15% jadeite) are preserved in garnet (Figure 5.6). However, these pyroxene inclusions may be prograde, rather than peak-P eclogitic pyroxene (Groppo et al., 2007). In the matrix, presumed omphacite has been entirely replaced by a plagioclase + Na-poor clinopyroxene symplectite that has been documented in other retrogressed eclogites as the result of the transition from eclogite to granulite facies (Lombardo and Rolfo, 2000; Groppo et al., 2007; Liu et al., 2007; Cottle et al., 2009). Similar to Cottle et al. (2009), no pseudomorphs after phengite, i.e., symplectites of high-Fe biotite and plagioclase as described by Groppo et al. (2007), were observed in any samples.

The thermal peak metamorphic assemblage is characterized by relatively coarse-grained diopsidic clinopyroxene (Figure 5.7), plagioclase, garnet, quartz, and trace orthopyroxene. A final thermal event is recorded in the retrograded eclogite by the almost total replacement of orthopyroxene by brown amphibole, which also grew in the clinopyroxene-plagioclase symplectite.

The LHS mafic amphibolites (AR01-2b, -11b, -35b, and -41) generally have a mineralogy consisting of quartz + amphibole + garnet + biotite + ilmenite ± clinopyroxene ± plagioclase ± rutile or titanite (Figs. 5.8-5.11). Regionally, different amphibolites exhibit a range of mineral assemblages (Goscombe and Hand, 2000), probably reflecting basaltic to hydrothermally altered volcanic protoliths. There is no petrographic or textural evidence that these rocks ever experienced eclogite-facies conditions. The samples contain no evidence for omphacite (no pseudomorphs,

symplectites, or inclusions in garnet), and garnets exhibit simple growth zoning of major elements (Figure 5.12).

5.3 Thermobarometry

5.3.1 Major Element Thermobarometry

While no direct barometric measurements can be made for eclogite-facies conditions, an estimate for the minimum pressures experienced by the rocks can be obtained by reintegrating sodic plagioclase into pyroxene (e.g., Will and Schmädicke, 2001). This integration assumes: 1) at eclogite facies, all sodium was hosted in clinopyroxene; 2) the albite and anorthite components of plagioclase texturally associated with matrix pyroxene (either in the symplectites or surrounding large diopsidic clinopyroxenes; Figure 5.7) were hosted in omphacite as the jadeite and Ca-Tschermaks components, respectively. This does not account for sodium in matrix hornblende or calcium originally hosted by garnet, and provides only a minimum estimate of the jadeite content. Assuming an average composition for plagioclase and diopside as measured by electron microprobe, the number of moles of each species is calculated via their respective modal abundances and molar volume. In sample AR01-43e, plagioclase has an average composition of $An_{19}Ab_{79}$ and modal abundances are 23 and 16% for plagioclase and clinopyroxene (estimated via ~300 point counts per sample). This reintegrates to an omphacitic pyroxene with a jadeite content of 39.1 mol%, which corresponds to a minimum pressure of 15 kbar at 670°C (Figure 5.6; Holland, 1980), with temperature estimated via Zr-in-titanite thermometry (see below). The same calculation for AR01-43c ($An_{39}Ab_{58}$; 21% plagioclase, 12.5% clinopyroxene) returns a jadeite component of 30.9

mol%, corresponding to 14.1 kbar at 670°C. Calculations based on small regions of symplectite yield greater scatter, but comparable results.

Pressure-temperature conditions for the post-eclogite metamorphic events were calculated using the garnet-clinopyroxene (Pattison and Newton, 1989) and garnet-hornblende (Graham and Powell, 1984) thermometers and the garnet-plagioclase-clinopyroxene-quartz (Eckert et al., 1991) and garnet-plagioclase-hornblende-quartz (Kohn and Spear, 1990) barometers (Figure 5.13a). Compositions for each calculation were selected based on spatial and textural relationships among the individual components; i.e., symplectitic and coronal plagioclase was chosen for garnet-plagioclase-clinopyroxene-quartz barometry and matrix plagioclase associated with hornblende for garnet-plagioclase-hornblende-quartz barometry (Tables 5.1-5.4). Intersection of the garnet-clinopyroxene and the garnet-plagioclase-clinopyroxene-quartz equilibria indicate pressure-temperature conditions of about 780°C and 12 kbar for the granulite-facies overprint. A later, third metamorphic event, represented by the growth of amphibole in the matrix, occurred around 675°C and 6 kbar.

5.3.2 Trace Element Thermobarometry

Zirconium-in-titanite thermometry (Hayden et al., 2008) was used to calculate temperatures for retrograded eclogites AR01-43c and -43e. Back-scattered electron images of titanite show no intracrystalline chemical zoning, although different grains have different compositions. Zircon is evident in all samples, either as observable matrix grains, or in mineral separates, or by relatively high Hf contents of bombed whole rock powders. Rutile is not present in samples where Zr-in-titanite thermometry was applied,

and the activity of TiO_2 was estimated to be 0.75 based on equilibrium among garnet, plagioclase, titanite, and quartz. Variations in $a(TiO_2)$ of ±0.1 change apparent temperatures by 7°C. Temperatures were calculated for matrix grains at pressures previously obtained via conventional thermobarometry for both the granulite and amphibolite metamorphic events, about 12 and 6 kbar, respectively (Table 5.5). At 12 kbar, core and rim temperatures of matrix titanite closely bracketed the ~780 °C calculated via garnet-clinopyroxene thermometry (Figure 5.13b). Yet, at 6 kbar, temperatures were ~710°C, 35°C higher than garnet-hornblende temperatures. It is possible titanite growth ceased prior to final growth and equilibration of hornblende.

Zirconium concentrations were measured from titanite inclusions in large matrix pyroxenes from sample AR01-43e (Table 5.5; Figure 5.7b). The resultant Zr-in-titanite temperatures (Hayden et al., 2008) were 35-130°C lower than matrix temperatures calculated for the same pressure (e.g., 650-745°C vs. ~780°C at 12 kbar), although apparent temperatures generally increase towards the pyroxene rim. A minimum pressure estimate for the lowest temperature titanite inclusion from a pyroxene core (~670°C), which presumably pre-dates the granulite event, is 15 kbar (Figure 5.13b; Holland, 1980), well within the eclogite-facies. This is consistent with initial formation of titanite in the eclogite-facies, with continued growth or recrystallization as the system began to exhume and heat from the eclogite-facies toward the peak-T granulite event.

The Zr-in-rutile thermometer (Watson et al., 2006) was also used on amphibolite samples AR01-35b and -41 and the temperatures calculated were approximately 660°C, similar to temperatures calculated for the amphibolite facies overprint in the eclogites. The Zr-in-rutile thermometer is only weakly pressure dependent (Tomkins et al., 2007),

and as these two samples do not contain plagioclase, an independent evaluation of pressure was not possible.

5.4 Lu-Hf Dating of Garnet

Garnet-whole rock isochrons yield ages ranging from 13.9 to 15.1 Ma for amphibolite samples, and 20.7 ± 0.4 Ma for a retrograded eclogite (Table 5.6, Figure 5.14). Analysis of bomb-digested whole-rock revealed significantly lower Lu-Hf ratios and higher Hf concentrations compared to tabletop digestions due to dissolution in the former of zircon. Such data were omitted from calculated isochrons if the $^{176}Hf/^{177}Hf$ of the bomb-digested whole-rock differed from the $^{176}Hf/^{177}Hf$ of the tabletop-digested whole-rock by more than 1.5×10^{-5}, presuming the zircon in these samples contained an inherited component not in equilibrium with garnet growth. If used in the regression, these data cause the calculated age to be spuriously old (e.g., Scherer et al., 2000). Models of Lu uptake in garnet (Lapen et al., 2003; Kohn, 2009) imply that garnet Lu-Hf ages should reflect early growth of garnet. Garnet X-ray maps from AR01-43c indicate that garnet cores represent ~75% of total garnet volume, but rims are enriched in Lu by a factor of ~1.4 compared to cores (Figure 5.5). Thus, 60-70% of the bulk garnet Lu-Hf age reflects eclogite-facies garnet growth, while 30-40% reflects growth in granulite-facies. Given the chemical simplicity of the amphibolite-facies LHS garnets in the underlying MCT footwall, their Lu-Hf ages are interpreted simply to reflect later amphibolite-facies metamorphism.

5.5 Discussion: P-T-t evolution and tectonic implications

Three main metamorphic stages are recognized in the retrograded eclogite

samples from eastern Nepal. Pressure-temperature conditions of primary eclogite facies

metamorphism are loosely constrained at 670°C and >15 kbar (≥50 km depth) by albite-

jadeite-quartz barometry and Zr-in-titanite thermometry. These are similar to conditions

inferred by Lombardo and Rolfo (2000) and Groppo et al. (2007) for rocks along strike in

Tibet. The eclogite was then strongly overprinted by a peak-temperature, granulite-facies

metamorphism at ~780°C and 12 kbar, recorded by garnet-plagioclase-clinopyroxene

equilibria and Zr-in-titanite thermometry. This was followed by a later, lower pressure

and temperature event at ~675°C and 6 kbar, represented by the widespread growth of

amphibole in the matrix and Zr-in-rutile thermometry. These conditions produce a

clockwise P-T path characterized by heating during initial exhumation (Figure 5.13b).

The general shape of the P-T path agrees well with Groppo et al. (2007), but specific P-T

results differ in that no evidence was found for the low pressures (e.g., 4 kbar) they

reported. Our estimated final pressures correspond well with conventional

thermobarometric results of Goscombe and Hand (2000) in the region for metapelites and

amphibolites.

The 20.7 ± 0.4 Ma age for the GHS eclogite is the first attempt to measure

directly the age of eclogitization in the central Himalaya, although several attempts have

been made to date the granulite metamorphism in the region. Cottle et al. (2009) ascribed

≤13 Ma monazite dates to peak granulite metamorphism and prograde anatexis.

However, partial melting should consume, not produce, monazite (Pyle and Spear, 2003;

Kohn et al., 2004, 2005; Kelsey et al., 2008), and these ages more likely represent post-

peak cooling and crystallization, presumably related to exhumation, thrust transport, or both. Groppo et al. (2007) also interpreted zircon rim ages of 13-14 Ma to represent late-stage granulite-facies metamorphism, but provide little direct evidence for this interpretation and concede that the zircon ages could instead be linked to the amphibolite-facies event. Overall, we interpret the 13-14 Ma monazite and zircon ages to reflect post-granulite facies overprinting associated with cooling during MCT transport. This interpretation agrees with the four 14-15 Ma prograde ages for garnet amphibolites from the LHS in the MCT footwall, and is consistent with relatively late initiation of the MCT along strike in Bhutan and central Nepal (Daniel et al., 2003; Kohn et al., 2004). Considering the weighted proportions of Lu in garnet cores (eclogite-facies: 60-70%) vs. rims (granulite-facies: 30-40%), and assuming that these components are mixed in these proportions in the garnet fractions, it implies an age of eclogitization of 23-26 Ma, and a latest possible granulite-facies age of 13-15 Ma.

The P-T-t evolution of the HP Arun and Ama Drime eclogites contrasts with the UHP eclogites from the northwest Himalaya in three fundamental ways: the Arun rocks were metamorphosed at much lower pressures; they show significant heating during initial exhumation; and they were metamorphosed 20-30 Myr later (Groppo et al., 2007; Cottle et al., 2009; this study). These differences potentially signal different tectonic processes. With respect to P-T paths, the nearly complete granulite-facies overprinting of the Arun eclogite may require either an extra heat source or a combination of slow erosion plus strongly diminished thrust transport in the mid-crust after loading. Rapid erosion alone should exhume rocks isothermally, whereas rapid thrusting on lower level thrusts should cool rocks isobarically. In principle, heating might also occur upon

expulsion of relatively cool lower crustal rocks into an inverted geotherm. The

occurrence of rapid exhumation (~30 km in ~7 Myr) with heating points to additional

heat sources or an inverted geotherm, and we evaluate possible competing models within

that context.

It is important to note that all models of Himalayan orogenesis predict eclogites in

the deep-crust. Thus, they key question is not the genesis of ~25 Ma eclogites, but rather

why they were exhumed and exposed at Arun and apparently not elsewhere. One possible

model is that their appearance simply reflects deepening or longer transport of the MCT

in the Arun area (Figure 5.15, Model 1a and 1b). This explanation is supported by

relatively low pressures of eclogitization – as little as 50 km depth, not ≥90 km as evident

in the northwest Himalaya. Peak metamorphic pressures near the base of the MCT in

central Nepal are already documented at 12 kbar (Kohn, 2008), and slight changes to

thrust geometry and dynamics could allow sampling of eclogite-facies, rather than

amphibolite-facies GHS rocks (Henry et al., 1997). The disparity in eclogite ages then

reflects different exhumation processes – slab breakoff at ~50 Ma and "normal"

Himalayan thrust transport at ~20 Ma. This model, however, does not adequately explain

the granulite-facies overprint at Arun. Within the context of fold-thrust belts, exhumation

between 25 and 14 Ma implies the eclogites were transferred to the hanging wall, but

thrust transport in the hanging wall should cause cooling, not heating.

A second possible model is that (aborted) subduction, slab breakoff, and buoyant

ascent of Indian crust occurred diachronously: ~50 Ma in the western Himalaya, ~25 Ma

in the central Himalaya, and presumably even younger in the eastern Himalaya. By this

model (Figure 5.15, Model 2a), mechanical coupling between the oceanic and Indian

continental lithospheres subducted India beneath Tibet to eclogite-facies conditions. Decoupling and removal of the down-going oceanic plate would cause asthenospheric upwelling and buoyant extrusion of a sliver of Indian crust out of the mantle lithosphere, causing rapid exhumation of the GHS and its eclogites (Kohn and Parkinson, 2002). Increased heat flow due to mantle upwelling could have increased temperatures to the granulite facies during exhumation. Differences along strike in exhumation rate or thermal structure might have allowed eclogites in the northwest Himalaya to exhume isothermally. Subsequent thrusting and transport would have cooled the Arun eclogites as they were incorporated in the Himalayan fold-thrust belt. While this model does explain our data, there is little supporting evidence elsewhere in the Himalaya for such profound along-strike diachroneity in fundamental tectonic processes.

A third, "hybrid" model recognizes the possibility of repeated loss of mantle lithosphere, possibly by different mechanisms (Chemenda et al., 2000). For example, in the northwest Himalaya, UHP eclogites may have been exhumed early by breakoff of the oceanic slab (O'Brien, 2001; Mahéo et al., 2002; Treloar et al., 2003; Parrish et al., 2006), whereas the Arun HP eclogites may have been exhumed later by delamination of Indian lithosphere (Figure 5.15, Model 2b). Like slab breakoff, delamination is expected to produce mantle upwelling, leading to a granulite-facies overprint. Again, we know of no other supporting evidence elsewhere along strike for this process, but the possibly unique occurrence of such young eclogites at Arun may require a geographically restricted process.

Regarding more specific thermal-mechanical models of thrust-belt development in the Himalaya, both channel flow (e.g., Beaumont et al., 2001) and critical taper

(Robinson et al., 2006) have been proposed to explain the metamorphism of the GHS (Jamieson et al., 2004; Kohn, 2008), and could in principle accommodate the presence of eclogites. However, neither model explains some key features of the Arun rocks. Channel flow models predict a focused erosional front for the last c. 25 Myr (Beaumont et al., 2001; Jamieson et al., 2004). Yet the Arun rocks were exhumed by ~30 km between 14 and 25 Ma, apparently far from any erosional front. This admittedly local observation casts doubt on how channel flow models account for erosion distributions and hence their predictive power for the Arun rocks. Moreover, the upper Arun River Valley is already differentiated from other areas along strike in the Himalaya by local E-W extensional structures that formed ≤13 Ma (Jessup et al., 2008; Cottle et al., 2009). As described previously, critical taper has trouble explaining P-T paths that combine exhumation with heating. Major changes must be invoked for the mechanical behavior of the wedge (to accommodate such profound thinning) and thrust rates (to accommodate heating) between 25 and 14 Ma.

One way of reconciling both channel flow and critical taper models with the Arun eclogite P-T-t path postulates that as parts of the lower crust heat and weaken, they may be expelled to the mid-crust, e.g. as modeled by Beaumont et al. (2006, model LHO-2; Figure 5.15, Model 3). An inverted geotherm is required to produce heating during expulsion, but this is predicted both in steady-state and time-dependent models (e.g., Royden, 1993; Henry et al., 1997; Beaumont et al., 2001). Less clear are the effects of expulsion on thermal state and later structures, particularly given the young age of exhumation (14-25 Ma). In this regard, the P-T-t history of the Arun and Ama Drime

eclogites may signal a change in the physical state of the Himalayan metamorphic

wedge at 16-25 Ma, ultimately giving rise to the MCT by 15-16 Ma.

111
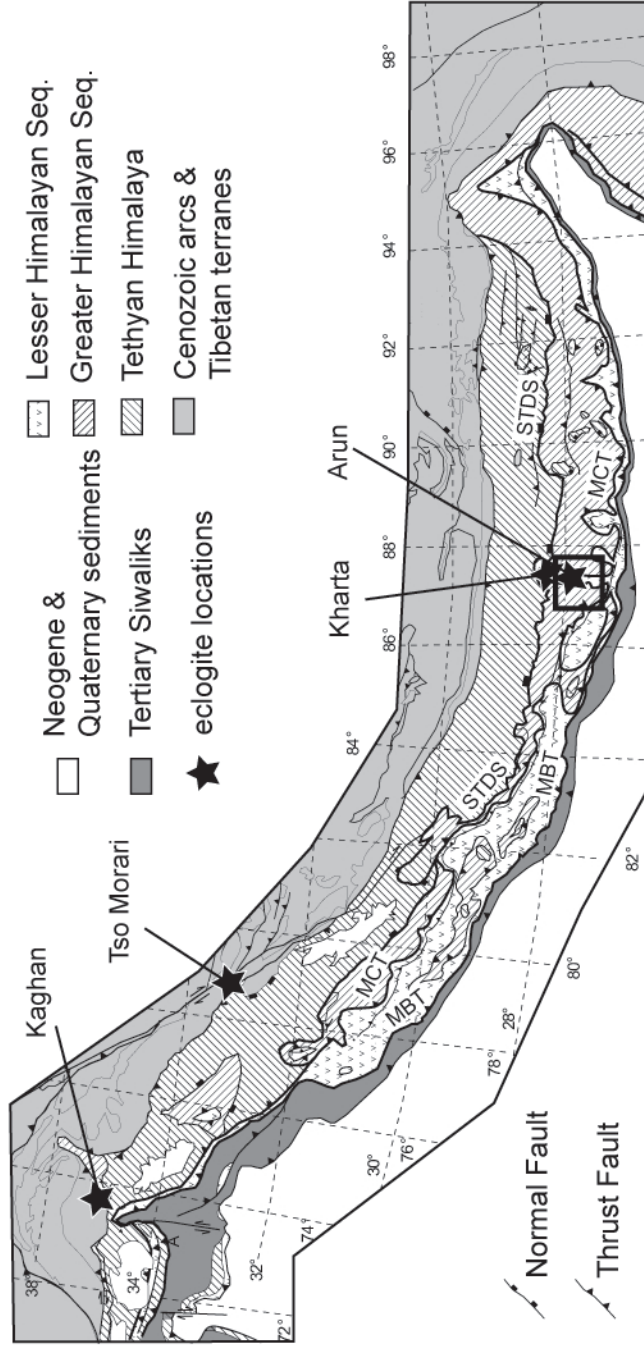
Figure 5.1. Generalized geologic map of the Himalaya showing major rock types and structures, and locations of Himalayan eclogites (modified from Yin, 2006). Black box shows area of Fig. 2. STDS = South Tibetan Detachment System; MCT = Main Central Thrust; MBT = Main Boundary Thrust.
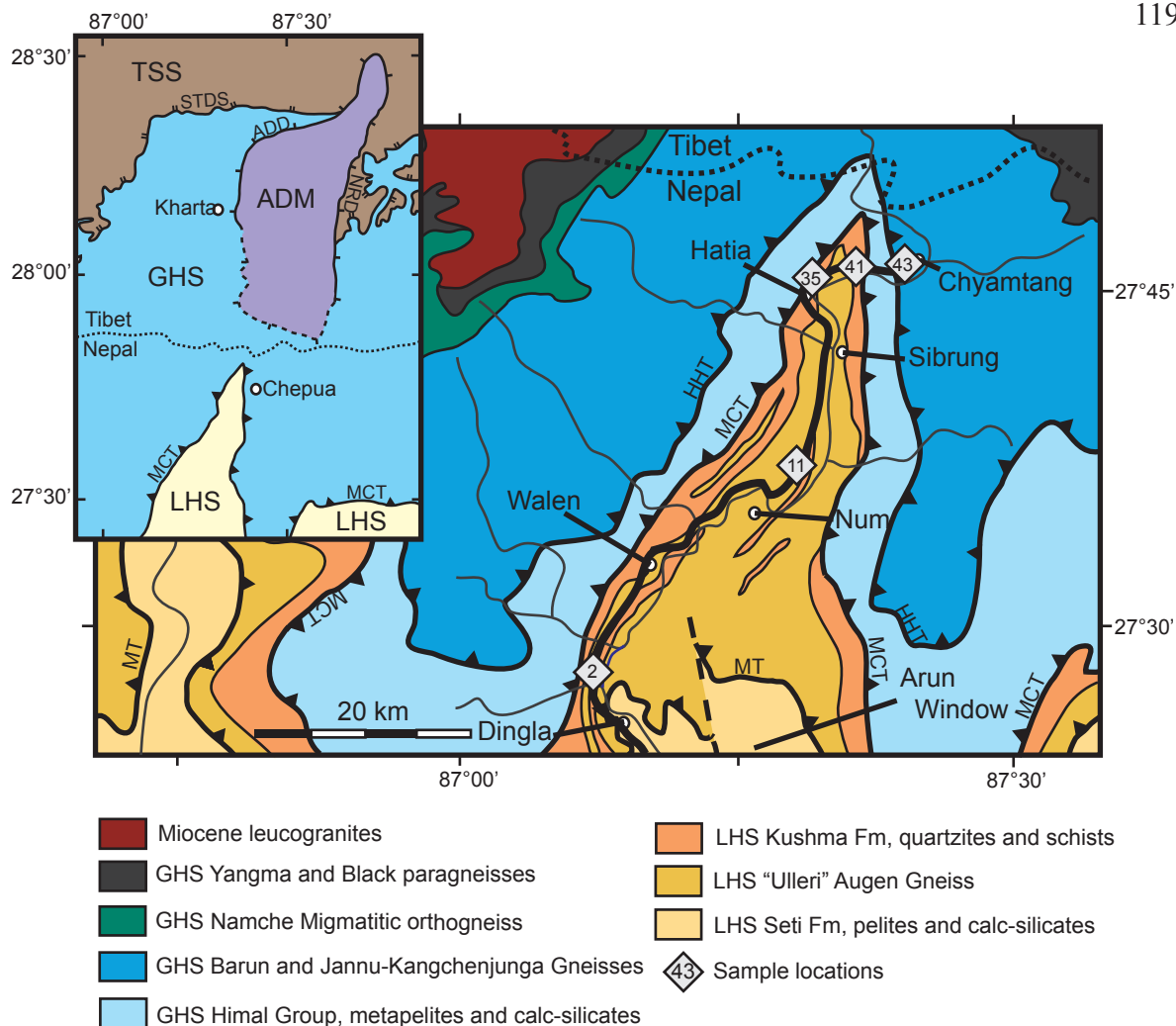
Figure 5.2. Geologic map of the Arun River Valley (after Goscombe and Hand, 2000; Goscombe et al., 2006). Samples were collected along the west side of the Arun Gorge on trails (represented by the thick black line). Numbers for sample locations follow the pattern AR01-X. Inset: Generalized regional map showing relationship between the orthogneiss in the Ama Drime Massif (ADM) and the rocks exposed in the Arun River Valley, Nepal (after Cottle et al., 2009). Thick barbed lines are the High Himalayan Thrust (HHT; a thrust within the GHS), Main Central Thrust (MCT), and Munsiari Thrust (MT). Single dashed lines are the Ama Drime Detachment (ADD) and the Nyonno Ri Detachment (NRD); double-dashed line is the South Tibetan Detachment system (STDS). Labeled circles indicate towns.
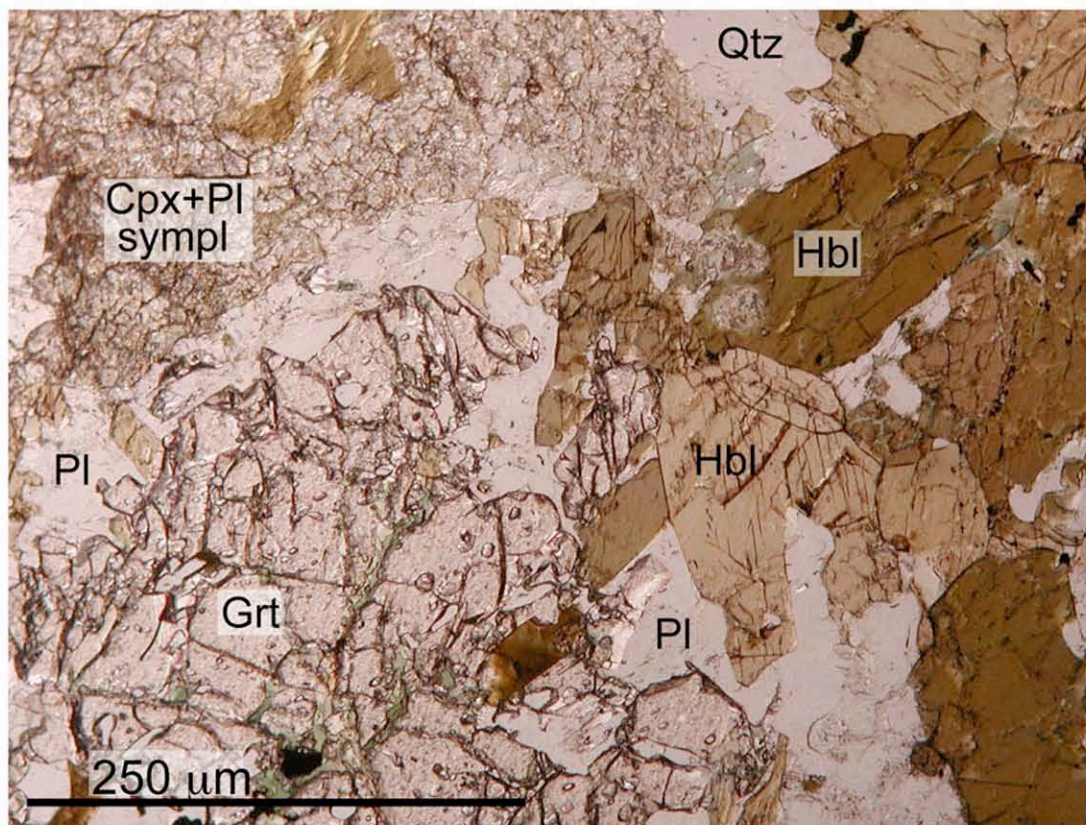
Figure 5.3. Photomicrograph of retrograded eclogite AR01-43c. Mineral assemblage consists of: hornblende + clinopyroxene + garnet + plagioclase + quartz + biotite + trace orthopyroxene + ilmenite + titanite + zircon + apatite + scapolite + calcite. The rock is speckled dark green and white, with 2-3 mm garnets scattered heavily throughout the matrix.
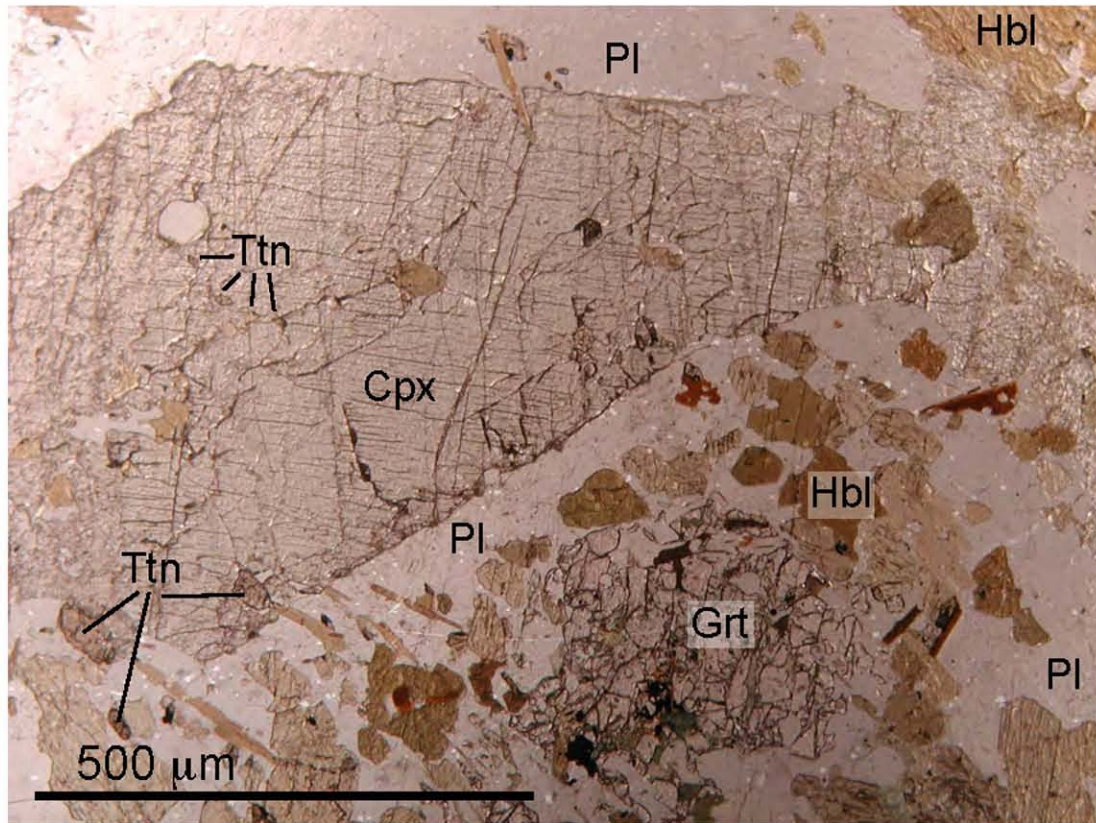
Figure 5.4 Photomicrograph of retrograded eclogite AR01-43e. Mineral assemblage consists of: clinopyroxene + hornblende + garnet + plagioclase + quartz + biotite + ilmenite + titanite + zircon + apatite + scapolite + calcite. The rock is speckled dark green and white, and contains garnets that are 2-3 mm in diameter. Large diopsidic clinopyroxenes in matrix are up to a centimeter in length.
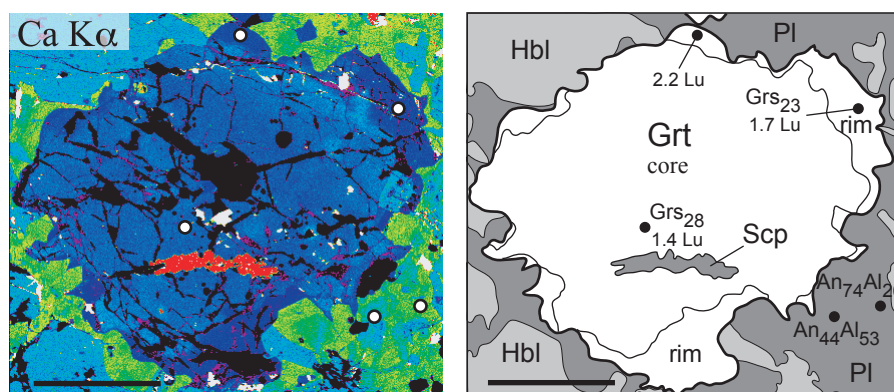
Figure 5.5. Ca X-ray map of garnet from sample AR01-43c with sketch showing core-rim relationship. Garnets exhibit broad cores with a relatively high Ca content (XGrs ≥ 0.28) and lower-Ca rims (XGrs ≤ 0.23). Lutetium concentrations are in ppm and show a slight enrichment of Lu in the overgrowth rims relative to the cores. Also note that matrix plagioclase is zoned from more sodic cores to more calcic rims. Scale bar is 500 mm. Grt = garnet, Hbl = hornblende, Pl = plagioclase, Scp = scapolite.
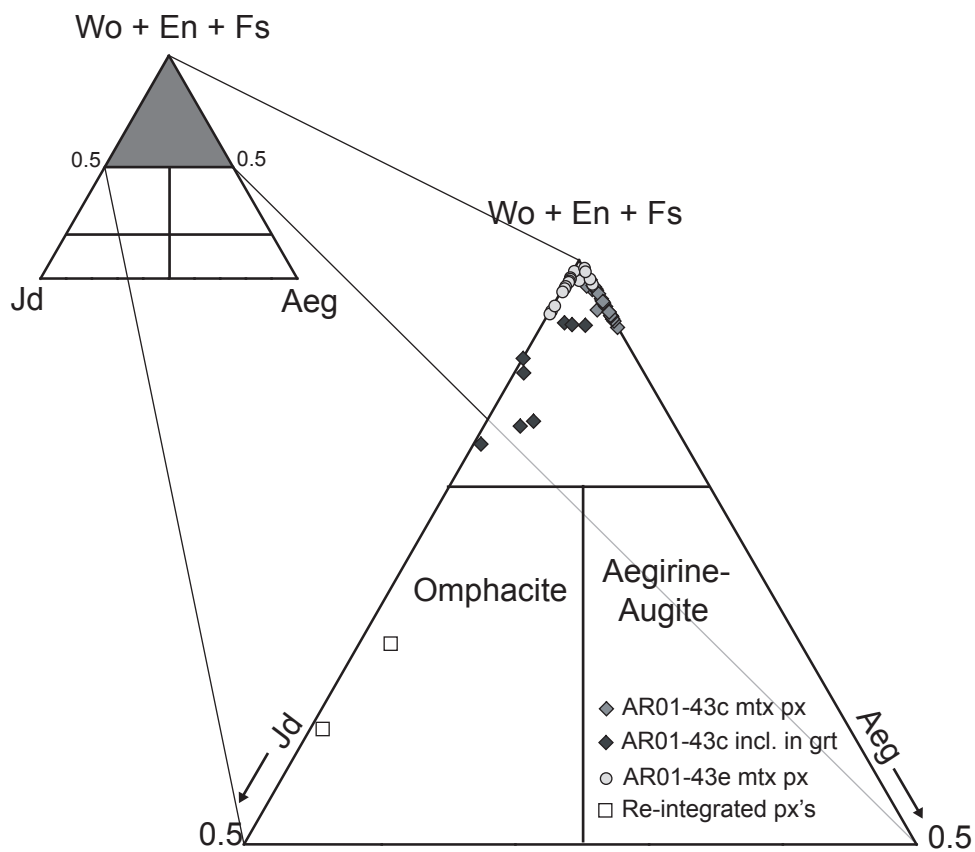
Figure 5.6. (Wollastonite + enstatite + ferrosilite) – jadeite – aegirine pyroxene compositional diagram (Morimoto et al., 1988). Matrix clinopyroxene is Na-poor (diopsidic). Clinopyroxene inclusions in garnet contain up to 15 mol% jadeite and plot close to the omphacite field. Re-integrated pyroxenes plot well within the omphacite field. n = 57.
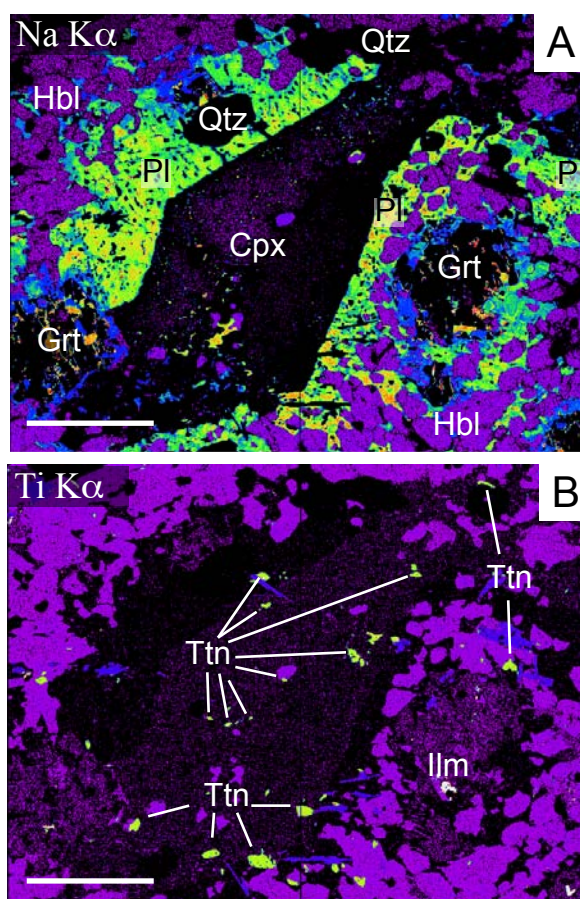
Figure 5.7. X-ray maps of a large crystal of diopsidic matrix pyroxene from sample AR01-43e. (A) Sodium x-ray map. Pyroxene surrounded by corona of sodic (average = Ab66) plagioclase. (B) Titanium x-ray map illustrating abundant titanite in the matrix and as inclusions in pyroxene. Scale bar is 2 mm. Grt = garnet, Hbl = hornblende, Pl = plagioclase, Cpx = clinopyroxene, Qtz = quartz, Ttn = titanite, Ilm = ilmenite.
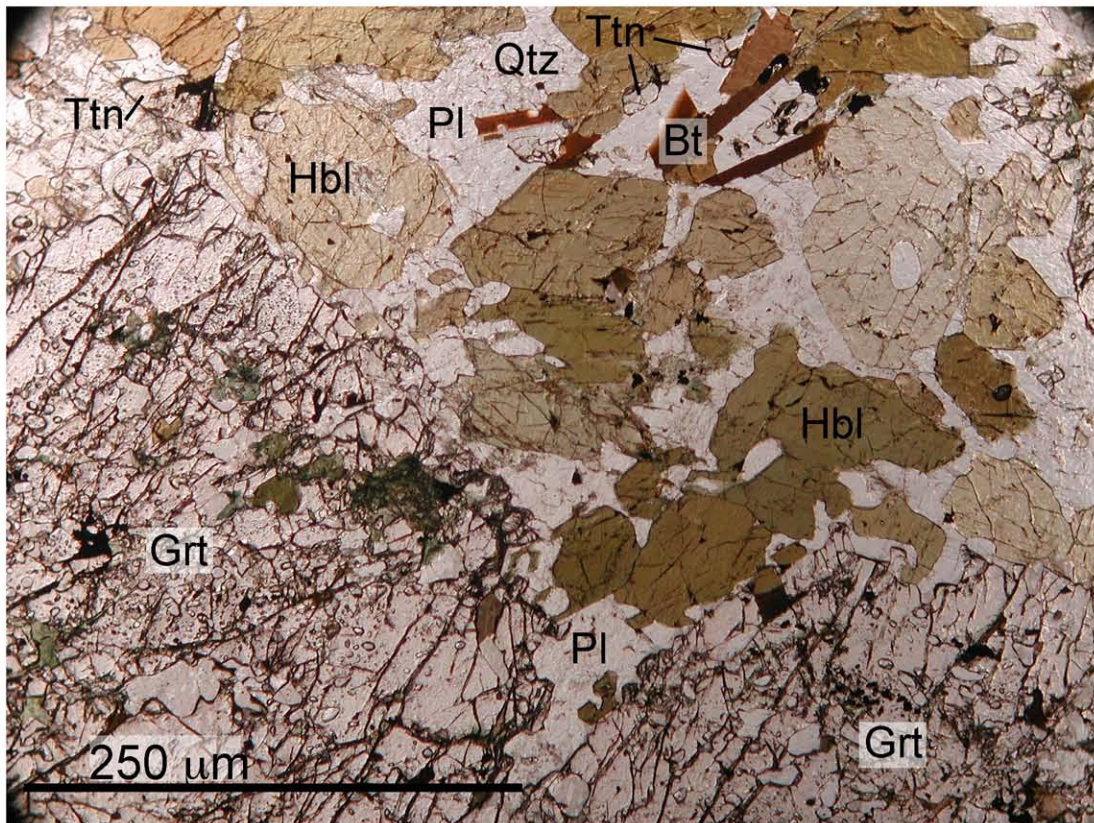
Figure 5.8. Photomicrograph of amphibolite AR01-2b. Mineral assemblage consists of: hornblende + clinopyroxene + garnet + quartz + plagioclase + ilmenite + biotite + titanite + apatite. The rock is dark green and contains abundant garnets that are 2-4 mm in diameter.
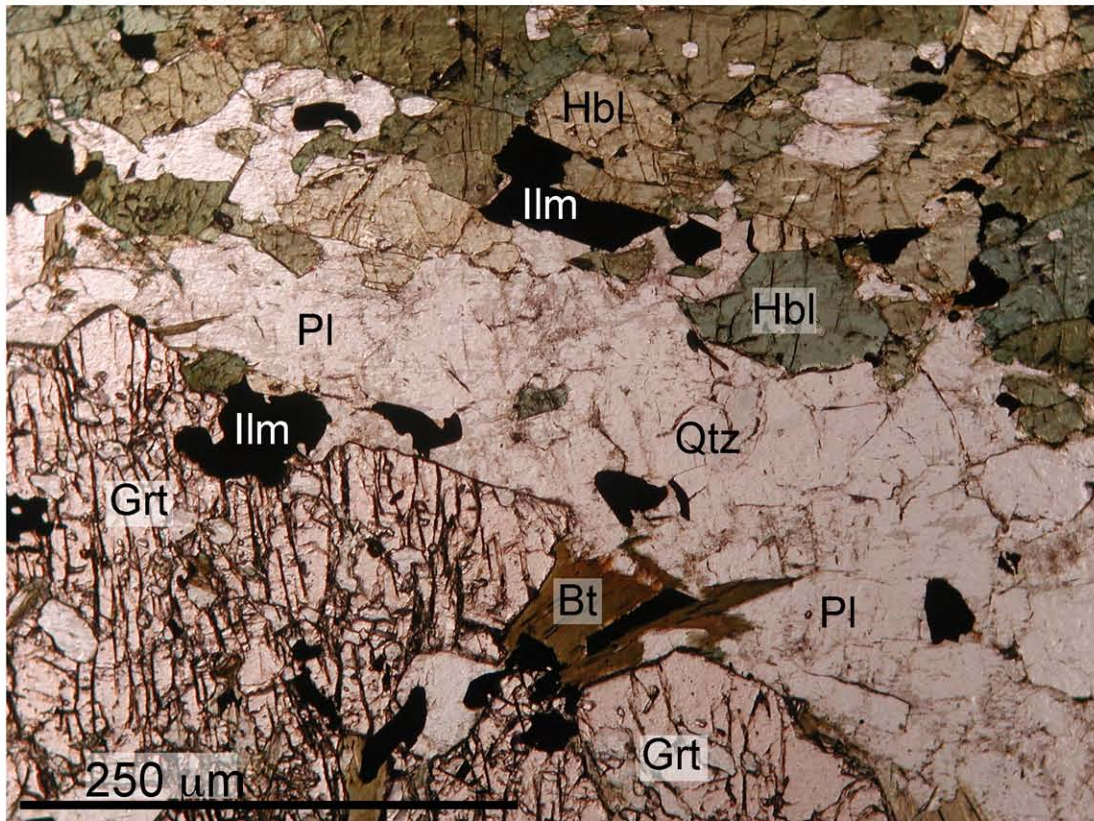
Figure 5.9. Photomicrograph of amphibolite AR01-11b. Mineral assemblage consists of: hornblende + plagioclase + garnet + ilmenite + quartz + rutile + apatite. The rock is dark green, exhibits a weak foiliation and contains irregularly shaped garnets that are ~5 mm in diameter surrounded by coronas of plagioclase and quartz.
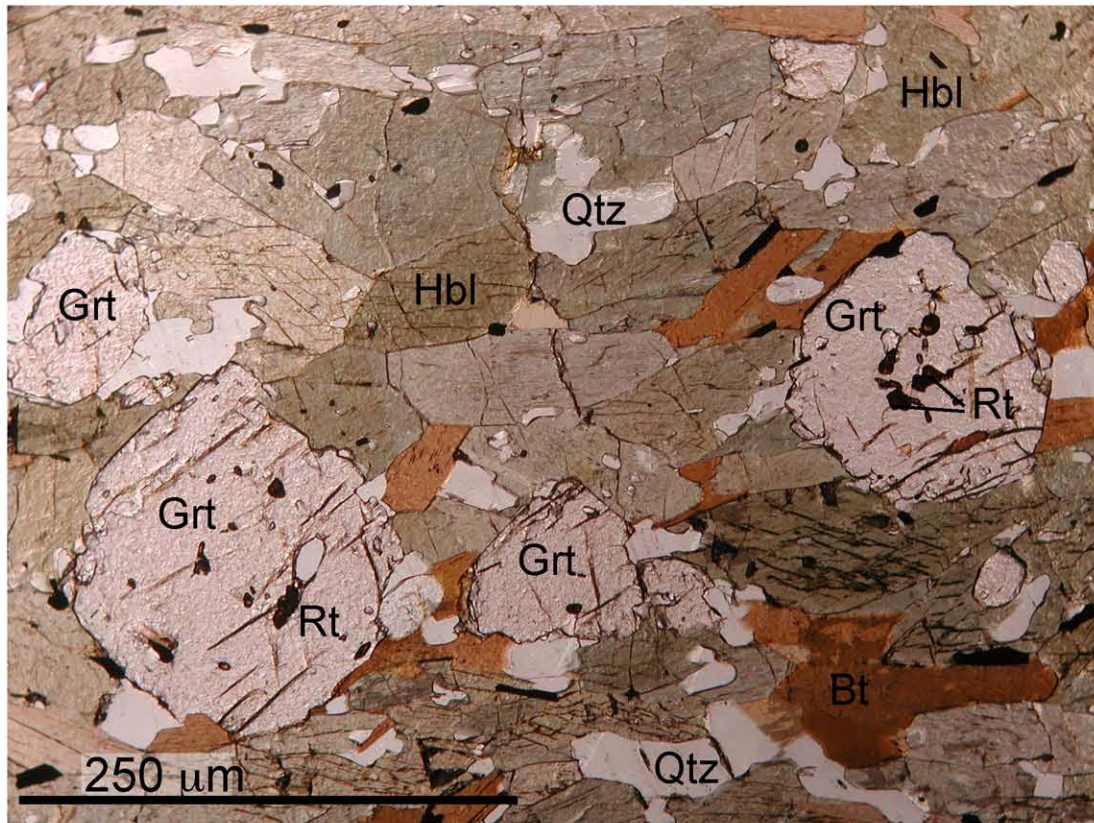
Figure 5.10. Photomicrograph of amphibolite AR01-35b. Mineral assemblage consists of: hornblende + biotite + garnet + quartz + ilmenite + rutile + apatite. The rock is dark green and contains small mm-scale segregations of quartz scattered throughout the body. Garnet sizes range from 1 mm up to 1 cm in diameter, and are scattered heavily throughout the matrix. Rutile is present as inclusions in garnet.
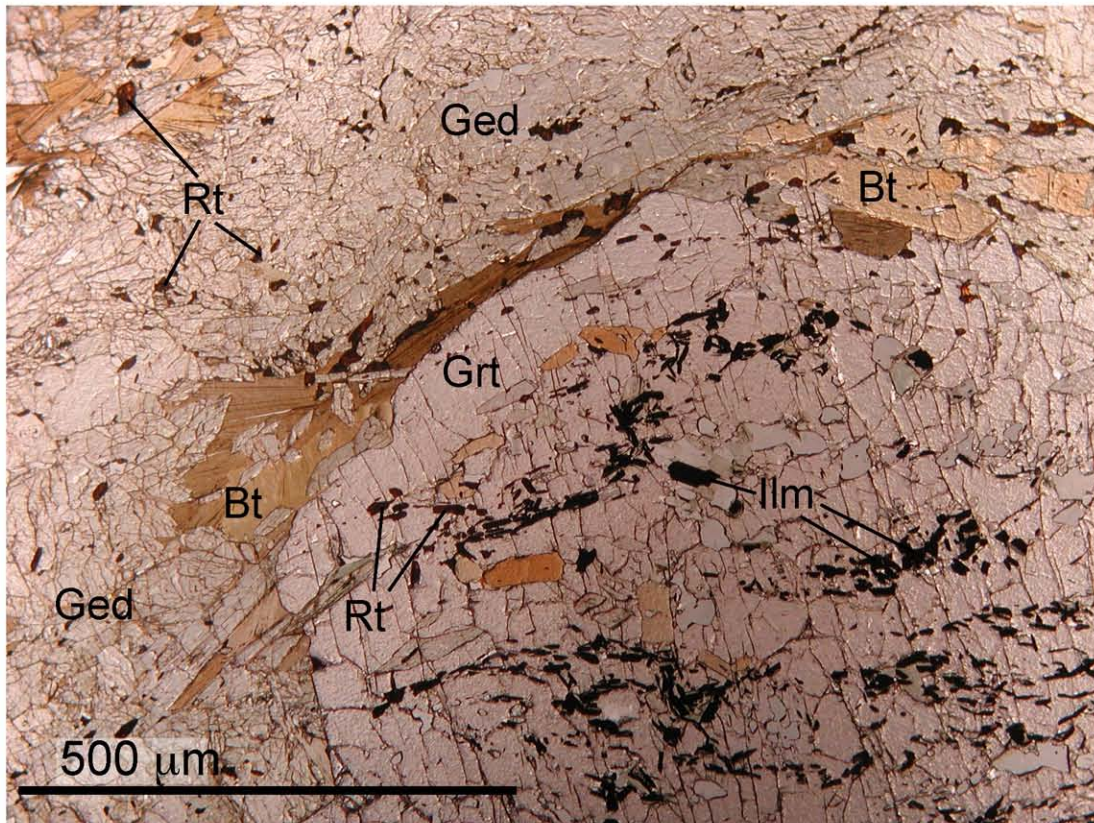
Figure 5.11. Photomicrograph of amphibolite AR01-41. Mineral assemblage consists of: gedrite + garnet + biotite + brown hornblende + ilmenite + rutile + quartz + apatite. The rock is greenish-brown and contains centimeter-sized garnets within a matrix primarily composed of orthoamphibole (gedrite). Thin (mm- to cm-scale) leucosomes, presumably originating from the host felsic rock, intrude into the mafic sill. Ilmenite is present only as inclusions within garnet cores, while the rutile is present in garnet rims and abundant in the matrix
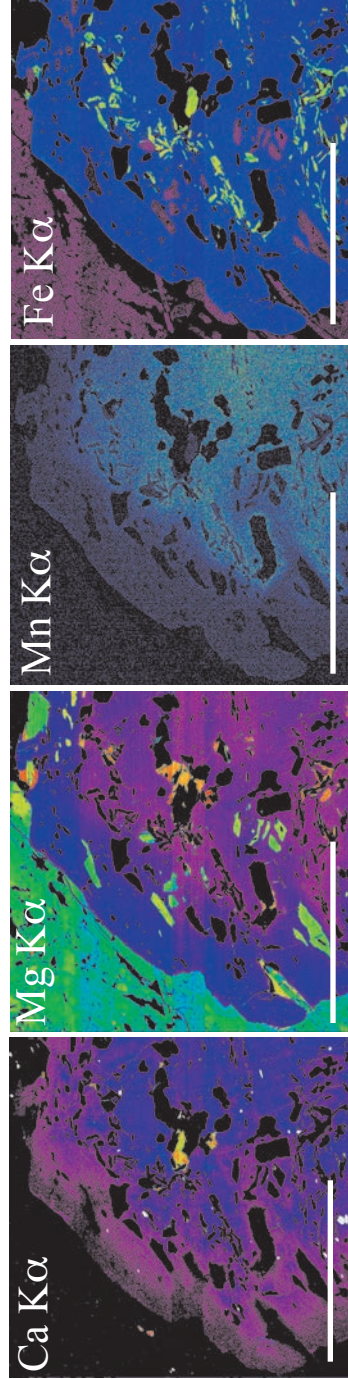
Figure 5.12. Major element x-ray maps of garnet from amphibolite sample AR01–41. Compositional trends are consistent with growth zoning. Scale bars are 500 mm.
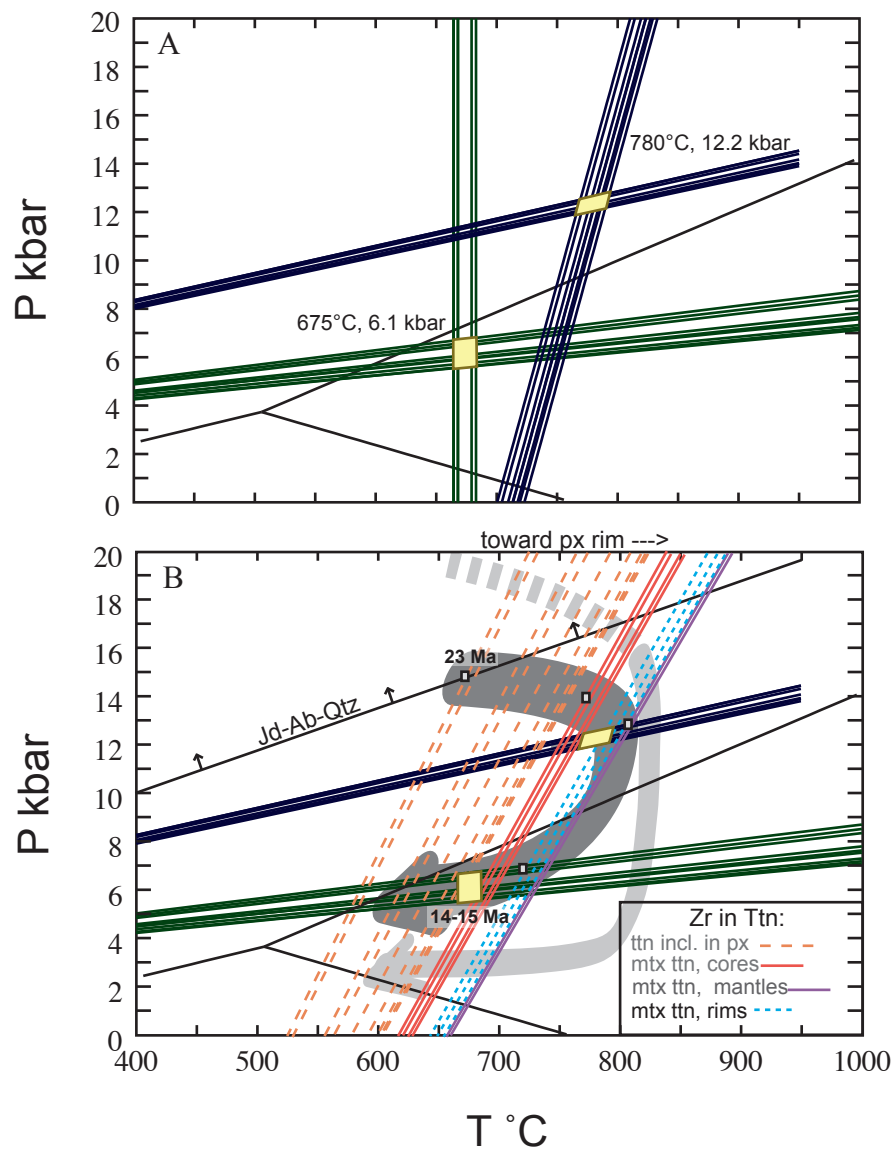
Figure 5.13. Pressure-temperature plots for retrograded eclogite AR01-43e. (A) P-T plot

showing equilibrium conditions for the granulite and amphibolite metamorphic events

calculated for sample AR01-43e. Intersection of the garnet-clinopyroxene (Pattison and

Newton, 1989) and garnet-plagioclase-clinopyroxene-quartz (Eckert et al., 1991)

equilibria indicates ~780°C and ~12 kbar for the granulite event. A later amphibolite-

facies overprint is recorded at ~675°C, ~6 kbar by garnet-hornblende (Graham and

Powell, 1984) and garnet-plagioclase-hornblende-quartz (Kohn and Spear, 1990)

equilibria. (B) Pressure-temperature plot showing Zr-in-titanite equilibrium lines plotted

with the barometers Jd-Ab-Qtz (Holland, 1980, calculated from the re-integration of

plagioclase into clinopyroxene), Grt-Pl-Cpx-Qtz and Grt-Pl-Hbl-Qtz from (A). Small

black arrows indicate minimum pressure estimate for Jd-Ab-Qtz equilibria; yellow boxes

represent average P-T conditions from (A); small white boxes denote points along the P-

T path determined by combining Zr thermometry with conventional barometry; large

dark gray arrow indicates general P-T trajectory; and light gray arrow indicates P-T

trajectory of Groppo et al. (2007) for the Ama Drime.
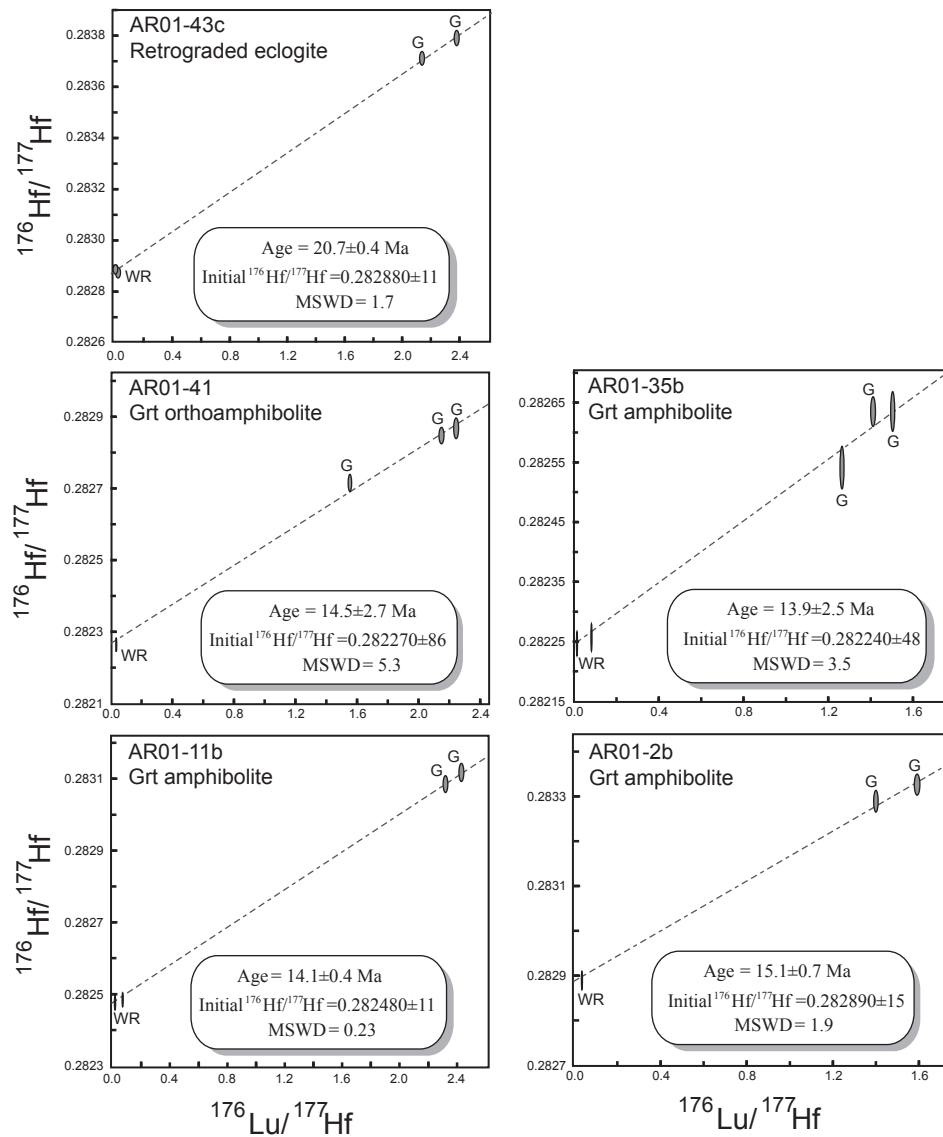
Figure 5.14. Lu-Hf isochron plots for eclogite and amphibolites. An age of ~21 Ma is calculated for the GHS Arun eclogite, and LHS amphibolite ages range from 14 to 15 Ma. All errors are at 95% confidence. G = garnet analysis; WR = whole-rock analysis.
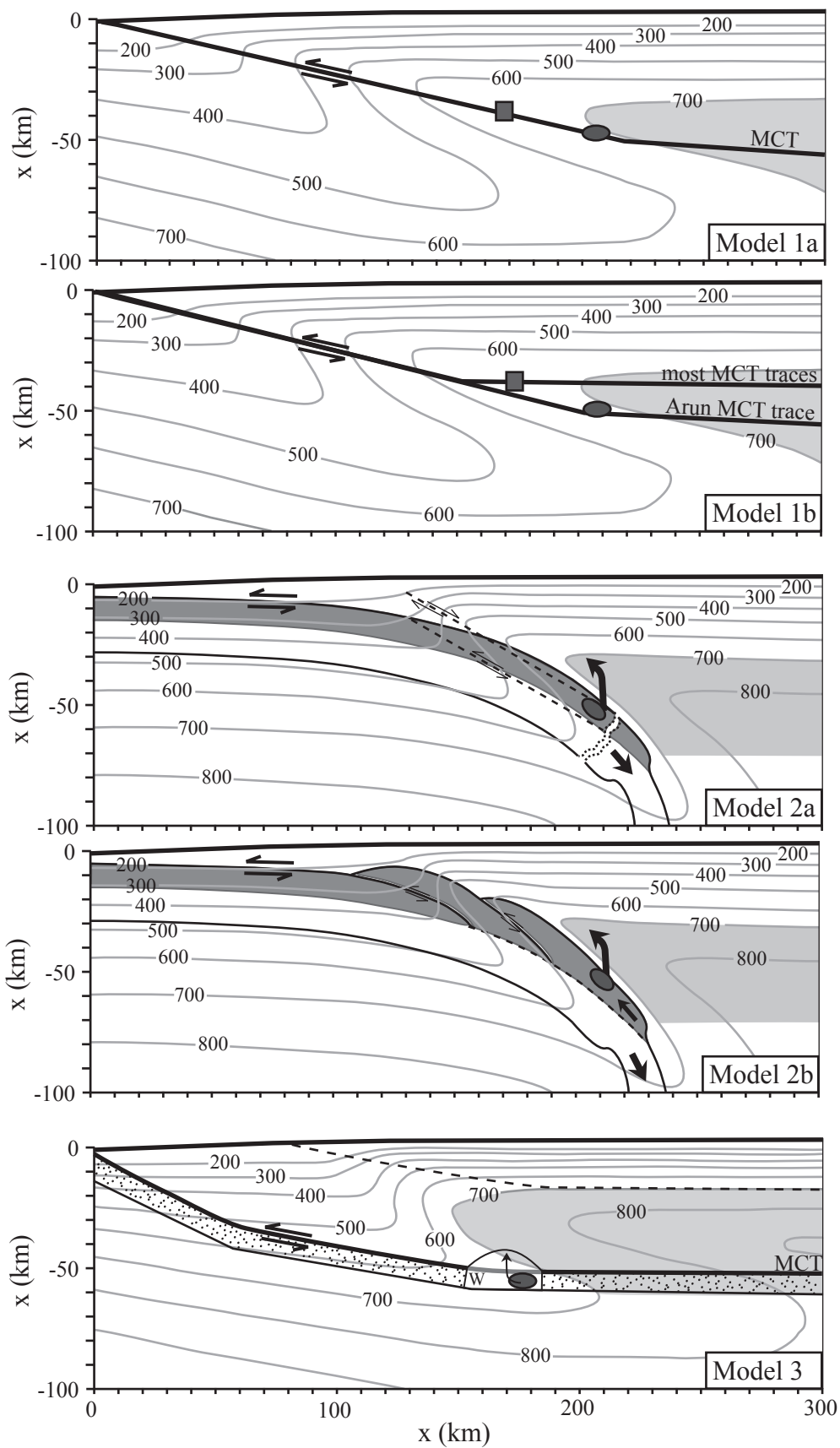
Figure 5.15. Schematic illustrations of potential tectonic models for the P-T-t evolution of

Arun eclogites showing overall thrust geometries, implied thermal structure, and

migmatite zone (T ≥ 700 °C, gray shading). MCT = Main Central Thrust. Gray ellipse =

GHS rocks from Arun; Gray squares = GHS rocks elsewhere. Model 1: Steady-state,

critical taper model for the Himalaya (based on Henry et al., 1997 and Bollinger et al.,

2006). At Arun, the MCT may have transported material further (model 1a) or cut deeper

(model 1b) than elsewhere in the orogen. This model does not explain the granulite-facies

overprint at Arun.

Model 2: Model of slab breakoff (model 2a; after Kohn and Parkinson, 2002) or

delamination (model 2b; after Chemenda et al., 2000). Detachment and removal of the

down-going plate or mantle lithosphere led to asthenospheric upwelling and buoyant

extrusion of a sliver of Indian crust, causing rapid exhumation of the GHS and the

eclogites. Both models explain granulite-facies overprint. Dark gray shaded area = Indian

continental crust.

Model 3: Channel Flow model (based on model LHO-2 from Beaumont et al., 2006) in

which weak areas in the lower plate detach, transfer to the upper-plate, and exhume. This

model may explain granulite-facies overprint. Stippled area = strong lower plate; W =

weak portion of lower plate.

Table 5.1 Representative Electron Microprobe Analyses of Garnet

Analysis #	43e.23	43e.101*	43e.121	43e.116*	43e.105*	43e.140*	43e.4	43e.109	43e.225
Textural setting	rim	rim	rim	mantle	mantle	mantle	core	core	core
SiO_2	37.87	37.59	37.36	37.61	37.34	37.43	38.26	38.07	38.17
TiO_2	0.06	0.04	0.05	0.06	0.05	0.08	0.05	0.06	0.06
Al_2O_3	21.82	22.02	22.10	21.83	21.67	22.07	21.62	22.34	21.73
FeO	28.38	28.51	27.90	26.73	26.52	27.46	27.21	26.75	25.63
MnO	0.74	1.06	1.36	0.82	0.82	1.15	1.97	0.42	0.61
MgO	3.92	4.02	3.82	4.30	4.24	3.32	2.85	3.45	3.45
CaO	8.35	8.28	8.57	9.63	9.85	9.89	10.18	10.95	10.51
Total	101.13	101.51	101.16	100.99	100.48	101.40	102.14	102.03	100.17
Si	2.960	2.933	2.925	2.936	2.932	2.927	2.974	2.941	2.989
Ti	0.003	0.003	0.003	0.004	0.003	0.005	0.003	0.003	0.003
Al	2.009	2.025	2.039	2.009	2.005	2.034	1.980	2.034	2.006
Fe	1.855	1.861	1.827	1.745	1.741	1.795	1.769	1.728	1.679
Mn	0.049	0.070	0.090	0.054	0.054	0.076	0.130	0.027	0.041
Mg	0.456	0.468	0.446	0.501	0.496	0.386	0.330	0.398	0.403
Ca	0.699	0.692	0.719	0.806	0.828	0.829	0.847	0.906	0.882
Alm	60.6	60.2	59.3	56.2	55.8	58.2	57.5	56.5	55.9
Grs	22.9	22.4	23.3	25.9	26.6	26.8	27.6	29.6	29.3
Pyp	14.9	15.1	14.5	16.1	15.9	12.5	10.7	13.0	13.4
Sps	1.6	2.3	2.9	1.7	1.7	2.5	4.2	0.9	1.4

All Fe reported as 2+

Cations calculated on the basis of 12 oxygens

* Composition used for thermobarometric analysis

Table 5.2 Representative Electron Microprobe Analyses of Plagioclase

Analysis #	43e.143*	43e.203*	43e.227	43e.38	43e.39	43e.15	43e.207*	43e.208*	43e.209	43e.210	43e.8	43c.13	43c.14	43c.62	43c.63
Textural setting	sympl.	sympl.	sympl.	mtx, core	mtx, core	mtx, rim	mtx, rim	mtx, rim	cpx corona	cpx corona	vein in grt	sympl.	sympl.	sympl.	cpx corona
SiO_2	61.61	61.64	62.71	56.06	55.39	49.22	52.24	52.26	63.77	64.03	46.84	56.89	56.50	57.38	58.26
Al_2O_3	24.11	23.88	23.47	28.08	28.57	33.25	30.27	30.04	23.02	22.75	34.45	27.37	27.37	26.75	25.45
FeO	0.07	0.01	0.32	0.04	0.04	0.24	0.13	0.09	0.01	0.02	0.29	0.22	0.18	0.19	0.08
CaO	4.99	5.07	4.50	9.33	9.93	14.91	12.54	12.09	3.68	3.63	16.65	8.82	8.73	8.06	7.03
Na_2O	8.81	8.89	9.34	6.20	5.98	2.88	4.36	4.62	9.82	9.56	1.93	6.81	6.89	7.19	8.06
K_2O	0.26	0.40	0.39	0.56	0.61	0.12	0.24	0.21	0.32	0.19	0.08	0.30	0.29	0.58	0.46
Total	99.84	99.90	100.73	100.27	100.52	100.62	99.78	99.30	100.60	100.17	100.24	100.40	99.96	100.15	99.34
Si	2.739	2.742	2.767	2.517	2.487	2.234	2.376	2.385	2.805	2.821	2.146	2.549	2.543	2.576	2.630
Al	1.263	1.252	1.221	1.486	1.512	1.779	1.622	1.616	1.193	1.181	1.861	1.445	1.452	1.415	1.354
Fe	0.003	0.001	0.012	0.001	0.002	0.009	0.005	0.003	0.000	0.001	0.011	0.008	0.007	0.007	0.003
Ca	0.238	0.242	0.213	0.449	0.478	0.725	0.611	0.592	0.173	0.171	0.818	0.423	0.421	0.387	0.340
Na	0.759	0.767	0.799	0.540	0.521	0.254	0.384	0.409	0.837	0.816	0.171	0.591	0.602	0.626	0.706
K	0.015	0.023	0.022	0.032	0.035	0.007	0.014	0.012	0.018	0.011	0.005	0.017	0.017	0.033	0.026
An	23.5	23.4	20.6	44.0	46.2	73.6	60.5	58.4	16.8	17.2	82.3	41.0	40.5	37.0	31.7
Ab	75.1	74.4	77.3	52.9	50.4	25.7	38.1	40.4	81.4	81.8	17.2	57.3	57.9	59.8	65.8
Or	1.4	2.2	2.1	3.1	3.4	0.7	1.4	1.2	1.7	1.1	0.5	1.6	1.6	3.2	2.5

All Fe reported as 2+

Cations calculated on the basis of 8 oxygens

* Composition used for thermobarometric analysis

Table 5.3 Representative electron microprobe analyses of clinopyroxene

Analysis #	43e.18	43e.21	43e.27	43e.135*	43e.138*	43e.139*	43e.154	43e.157	43c.108	43c.119	43c.120	43c.202	43c.203	43c.204
Textural setting	matrix	matrix	matrix	sympl.	sympl.	sympl.	sympl.	sympl.	matrix	matrix	matrix	incl. in grt	incl. in grt	incl. in grt
SiO_2	51.95	52.45	52.65	51.52	52.19	52.73	51.57	51.81	52.06	51.48	52.20	52.27	51.69	52.99
TiO_2	0.20	0.10	0.07	0.10	0.13	0.14	0.22	0.19	0.16	0.16	0.10	0.07	0.13	0.12
Al_2O_3	1.66	1.12	0.69	3.69	2.91	4.17	3.90	3.65	1.58	2.72	1.08	7.01	6.92	4.95
FeO	10.92	10.45	8.88	13.27	12.77	12.03	12.36	11.86	9.10	8.97	8.31	8.84	8.32	8.50
MnO	0.11	0.13	0.10	0.03	0.10	0.09	0.05	0.05	0.06	0.08	0.08	0.03	0.04	0.01
MgO	12.13	12.03	13.15	11.64	11.10	10.33	11.58	11.18	12.96	12.61	13.20	11.52	12.51	13.40
CaO	21.96	22.86	23.27	19.07	20.08	19.70	19.89	20.64	23.78	22.99	24.40	17.97	18.23	17.66
Na_2O	0.31	0.23	0.22	0.60	0.61	0.71	0.67	0.69	0.32	0.49	0.23	2.22	1.96	2.01
Total	99.25	99.36	99.02	99.92	99.89	99.90	100.23	100.06	100.03	99.50	99.58	99.93	99.79	99.65
Si	1.969	1.987	1.987	1.944	1.974	1.994	1.935	1.949	1.943	1.929	1.955	1.923	1.898	1.947
Al^{IV}	0.031	0.013	0.013	0.056	0.026	0.006	0.065	0.051	0.057	0.071	0.045	0.077	0.102	0.053
Al^{VI}	0.043	0.037	0.018	0.108	0.104	0.180	0.108	0.111	0.013	0.049	0.002	0.226	0.198	0.162
Ti	0.006	0.003	0.002	0.003	0.004	0.004	0.006	0.005	0.005	0.005	0.003	0.002	0.004	0.003
Fe^{3+}	0.000	0.000	0.007	0.000	0.000	0.000	0.000	0.000	0.057	0.048	0.054	0.005	0.035	0.027
Fe^{2+}	0.346	0.331	0.274	0.419	0.404	0.380	0.388	0.373	0.227	0.233	0.206	0.267	0.220	0.234
Mg	0.685	0.679	0.739	0.654	0.626	0.582	0.647	0.627	0.721	0.704	0.736	0.631	0.684	0.734
Mn	0.004	0.004	0.003	0.001	0.003	0.003	0.002	0.002	0.002	0.002	0.003	0.001	0.001	0.000
Ca	0.892	0.928	0.941	0.771	0.814	0.798	0.800	0.832	0.951	0.923	0.979	0.708	0.717	0.695
Na	0.023	0.017	0.016	0.044	0.045	0.052	0.048	0.050	0.023	0.035	0.017	0.158	0.139	0.143
Aeg	0.0	0.0	0.7	0.0	0.0	0.0	0.0	0.0	2.3	3.5	1.7	0.5	3.5	2.7
Jd	2.3	1.7	0.9	4.4	4.5	5.2	4.8	5.0	0.0	0.0	0.0	15.4	10.4	11.6
Wo	44.6	46.4	47.0	35.6	39.2	39.4	36.5	38.8	47.6	46.2	48.9	35.4	35.9	34.8
En	34.2	34.0	37.0	32.7	31.3	29.1	32.4	31.3	36.1	35.2	36.8	31.6	34.2	36.7
Fs	17.3	16.6	13.7	20.9	20.2	19.0	19.4	18.7	11.4	11.7	10.3	12.4	11.0	11.7

Fe3+ recalculated according to stoichiometry
Cations calculated on the basis of 6 oxygens
* Composition used for thermobarometric analysis

Table 5.4 Representative Electron Microprobe Analyses of Hornblende

Analysis #	43e.148	43e.149	43e.211*	43e.303*	43c.21	43c.24	43c.26	43c.61
Textural setting	sympl.	sympl.	matrix	matrix	matrix	sympl.	sympl.	matrix
SiO_2	40.55	40.67	42.24	42.04	42.44	41.16	41.32	41.39
TiO_2	2.03	1.91	1.95	2.04	1.66	1.75	1.97	1.79
Al_2O_3	12.68	12.85	12.68	12.32	12.88	13.28	13.33	13.63
FeO	17.75	17.44	16.03	16.95	14.71	15.56	15.21	14.68
MnO	0.13	0.15	0.12	0.10	0.09	0.09	0.06	0.02
MgO	9.10	9.17	9.45	9.84	10.87	10.19	10.13	10.47
CaO	11.04	11.04	11.25	11.21	11.22	11.03	11.06	11.36
Na_2O	1.35	1.34	1.35	1.32	1.21	1.37	1.45	1.60
K_2O	2.84	2.81	3.10	2.92	3.23	3.44	3.42	3.46
Total	97.47	97.37	98.18	98.75	98.31	97.87	97.95	98.39
Si	6.213	6.225	6.356	6.317	6.339	6.224	6.232	6.202
Ti	0.234	0.220	0.221	0.231	0.186	0.199	0.223	0.202
Al	2.290	2.318	2.250	2.182	2.268	2.366	2.369	2.407
Fe	2.275	2.233	2.017	2.130	1.837	1.968	1.918	1.839
Mn	0.016	0.019	0.015	0.013	0.011	0.012	0.008	0.002
Mg	2.079	2.093	2.119	2.204	2.420	2.297	2.277	2.339
Ca	1.813	1.810	1.814	1.805	1.795	1.788	1.788	1.823
Na	0.402	0.398	0.394	0.385	0.351	0.401	0.424	0.466
K	0.555	0.548	0.596	0.560	0.616	0.664	0.657	0.661

All Fe reported as 2+

Cations calculated on the basis of 23 oxygens

* Composition used for thermobarometric analysis

Table 5.5 Zr-in-Rutile and Zr-in-Titanite Results

	Zr-in-Rt			Zr-in-Ttn*		
Sample	35b	41	Sample	43c	43e	43e incl. in cpx
	matrix	matrix		matrix	matrix	
# of analyses	5	8	# of analyses	7	9	9
ppm Zr ($\pm 1\sigma$)	367$\pm$25	355$\pm$20	ppm Zr ($\pm 1\sigma$)	168$\pm$63	162$\pm$56	39$\pm$23
T °C ($\pm 1\sigma$)	659$\pm$6	656$\pm$5	T °C[a] ($\pm 1\sigma$)	708$\pm$21	707$\pm$18	
			T °C[b] ($\pm 1\sigma$)	776$\pm$22	775$\pm$20	697$\pm$34
			T °C[c] ($\pm 1\sigma$)			718$\pm$35

*Activity of TiO_2 assumed to be 0.75

[a] Temperature calculated at 6 kbar

[b] Temperature calculated at 12 kbar

[c] Temperature calculated at 14 kbar

Table 5.6 Lu-Hf Isotopic Results for Garnet and Whole-rock Separates

Sample	Fraction	Lu (ppm)	Hf (ppm)	$^{176}Lu/^{177}Hf$	$^{176}Hf/^{177}Hf$	Initial $^{176}Hf/^{177}Hf$ [a]	Isochron Age (Ma)
AR01-2b	grt1	1.60	0.162	1.400	0.283291±13	0.282890±15	15.1±0.7
	grt2	1.60	0.142	1.593	0.283327±13		
	WR	0.160	0.779	0.0291	0.282894±06		
	*WR'	0.158	1.97	0.0114	0.282869±06		
AR01-11b	grt1	1.87	0.115	2.312	0.283086±12	0.282480±11	14.1±0.4
	grt2	1.95	0.114	2.422	0.283119±14		
	WR	0.269	0.591	0.0647	0.282494±05		
	WR'	0.284	4.16	0.0097	0.282486±05		
AR01-35b	grt1	1.54	0.155	1.412	0.282635±14	0.282240±48	13.9±2.5
	grt2	1.77	0.167	1.504	0.282635±23		
	grt3	1.62	0.182	1.264	0.282542±24		
	WR	0.234	0.417	0.0795	0.282263±10		
	WR'	0.254	3.38	0.0107	0.282252±06		
AR01-41	grt1	2.33	0.147	2.244	0.282865±17	0.282270±86	14.5±2.7
	grt2	2.23	0.204	1.550	0.282716±11		
	grt3	3.54	0.234	2.149	0.282847±11		
	WR	0.085	0.506	0.0240	0.282271±05		
	*WR'	0.104	3.43	0.0043	0.282069±05		
AR01-43c	grt1	1.57	0.094	2.378	0.283787±18	0.282880±11	20.7±0.4
	grt2	1.57	0.104	2.140	0.283708±15		
	WR	0.158	0.738	0.0303	0.282878±03		
	WR'	0.177	1.95	0.0129	0.282889±05		

WR, whole rock by savillex digestion; WR', whole rock by bomb digestion.

reported errors are 2σ

* data not used in regression

[a] calculated from isochron

CHAPTER 6: SUMMARY OF CONCLUSIONS

Several themes emerge from the data reported in this dissertation. The following outlines the contributions and prospective future research related to the questions posed in Chapter 1.

6.1 Annapurna

• Rocks in the Modi Khola valley display the apparent inverted metamorphic gradient associated with the Main Central Thrust. Temperatures increase structurally upsection, with a steep gradient at the Munsiari and Main Central Thrusts. Pressures also increase upsection, including all samples from the GHS, unlike at Langtang, 200 km to the east. With increasing structural level, peak P-T conditions were: 515 °C and 7.5 kbar (LHS below the Munsiari Thrust), 555 °C and 10.5 kbar (within the Munsiari Thrust sheet), 650 °C and 12.0 kbar (base of the Main Central Thrust Sheet), 735 °C and 12.5 kbar (Formation 1b), and 775 °C and 12.5 kbar (Formation 1c).

• Four generations of monazite have been identified in samples in central Nepal. From oldest to youngest they are: inherited, early prograde, late prograde, and post-anatectic, and can be distinguished chemically and chronologically.

• Peak metamorphic and post-anatectic monazite ages both progressively increase up-section. Monazite from GHS Formation 1a exhibits prograde

- metamorphic ages of 21-25 Ma. Formation 1b monazite contains prograde cores that are 24-29 Ma and high-Y rims that register cooling and melt crystallization ages of 17-22 Ma. In samples from Formation 1c, post-anatectic cooling and monazite growth occurred 19-15 Ma. In monazite from GHS Formation III, just below the South Tibetan Detachment, early prograde monazites are 35-38 Ma with later prograde growth at 30-35 Ma.

- Based on P-T gradients (increasing pressures up-section), we revise the original interpretation of the Bhanuwa Fault from a normal fault to a thrust, and identify a new thrust called the Sinuwa Fault structurally above the Bhanuwa thrust.

- Thrust rate calculations are generally consistent with a 2 cm/yr convergence rate component across the Himalaya from ~25 to ~15 Ma, supporting models that presume constant rates since at least 25 Ma, though the similarity in inferred peak ages for the ST, BT, and MCT could in principle indicate simultaneous initial cooling of all three sheets at ~22 Ma. A simultaneous cooling model could indicate as much as 100 km of out-of-sequence thrusting.

- Geochemically similar generations of monazite occur at both Langtang and Annapurna, but monazite ages along the Modi Khola appear older by ~5 Myr compared to Langtang, potentially indicating that the MCT at Annapurna is equivalent to the Langtang Thrust at Langtang (i.e., the thrust cuts up section from west to east).

• The similarity between the chemical systematics of monazite, peak P-T conditions, and thrust rates calculated for Langtang and Annapurna implies that strain measurements in one part of an orogen can be realistically extrapolated to another within a few hundred kilometers.

6.2 Arun

• Garnet geochronology was used to provide the first direct measurement of the timing of eclogitization in the central Himalaya. Lu-Hf dates from garnet separates in one relict eclogite from the Arun River valley in eastern Nepal indicate an age of 20.7±0.4 Ma, significantly younger than ultra-high pressure eclogites from the western Himalaya, reflecting either different origins or substantial time lags in tectonics along strike.

• Four proximal garnet amphibolites from structurally lower horizons are 14-15 Ma, similar to post-eclogitization ages published for rocks along strike in southern Tibet.

• P-T calculations indicate three stages of metamorphism for the eclogite: i) eclogite-facies metamorphism at ~670 °C and ≥ 15 kbar at 23-16 Ma; ii) a peak-T granulite event at ~780 °C and 12 kbar; iii) late-stage amphibolite-facies metamorphism at ~675°C and 6 kbar at ~14 Ma.

• Three models are considered to explain the observed P-T-t evolution: 1) deepening or longer transport of the MCT in the Arun area; 2) subduction, slab breakoff, and buoyant ascent of Indian crust occurred diachronously; and 3)

repeated loss of mantle lithosphere. These models either have difficulty

explaining the P-T data, or require significant along-strike diachroneity and/or

geographically restricted tectonic behavior at Arun.

• The channel flow and critical taper thermal-mechanical models of thrust-

belt development in the Himalaya could in principle accommodate the presence of

eclogites. However, neither model explains some key features of the Arun rocks.

Channel flow models predict a focused erosional front for the last c. 25 Myr, yet

the Arun rocks were exhumed by ~30 km between 14 and 25 Ma, apparently far

from any erosional front. Critical taper has difficulty explaining P-T paths that

combine exhumation with heating.

• A model that reconciles channel flow and critical taper with the eclogite P-

T-t path suggests that as parts of the lower crust heat and weaken, they may be

expelled to the mid-crust. An inverted geotherm is required to produce heating

during expulsion, but this is predicted both in steady-state and time-dependent

models.

• The P-T-t history of the central Himalayan eclogites may signal a change

in the physical state of the Himalayan metamorphic wedge at 16-25 Ma.

6.3 Future Research

• Additional measurements of the chemical systematics of monazite, peak

P-T conditions, and thrust rates from other parts of the orogen, e.g. in India or

Bhutan, are needed to verify whether P-T-t results and strain estimates from Annapurna and Langtang could be applied to the orogen as a whole.

• Geochronologic and thermobarometric information reported here directly impacts our understanding of the stages of mountain building, especially with regard to the classic assumption of in-sequence thrusting and convergence of the Greater Himalayan sequence. Additional measurements of peak metamorphic and cooling ages from elsewhere in Nepal as well as other parts of the orogen are needed to assess the viability of assuming in-sequence thrusting as a part of tectonic models of Himalayan development.

• Eclogites may well be present at the surface in many locations in the central and eastern Himalaya, but have been overlooked due to the classic mistake of selective collection of rocks most appropriate for thermobarometric and geochronologic analaysis (e.g., metapelites). Thorough sampling and petrologic analysis is necessary to identify these rocks, which may have significant implications for Himalayan tectonic and thermal-mechanical models.

REFERENCES

Ahmad, T., Harris, N., Bickle, M., Chapman, H., Bunbury, J., and Prince, C. 2000. Isotopic constraints on the structural relationships between the Lesser Himalayan Series and High Himalayan Crystalline Series, Garhwal Himalaya. GSA Bulletin, v. 112, p. 467-477.

Beaumont, C., Jamieson, R. A., Nguyen, M. H., and Lee, B. 2001. Himalayan tectonics explained by extrusion of a low-viscosity crustal channel coupled to focused surface denudation. Nature, v.414, p. 738-742.

Beaumont, C., Jamieson, R.A., Nguyen, M.H., and Medvedev, S., 2004. Crustal channel flows: 1. Numerical models with applications to the tectonics of the Himalayan-Tibetan Orogen. Journal of Geophysical Research, v. 109, p. B6.

Beaumont, C., Nguyen, M.H., Jamieson, R.A., and Ellis, S. 2006. Crustal flow modes in large hot orogens. Geological Society Special Publication, v. 268, p. 91-145.

Berman, R.G. 1990. Mixing properties of Ca-Mg-Fe-Mn garnets. American Mineralogist, v. 75, p. 328-244.

Bilham, R., Larson, K., and Freymueller, J. 1997. Indo-Asian convergence rates in the Nepal Himalaya. Nature, v. 311, p. 621-626.

Bollinger, L., Henry, P., and Avouac, J.P. 2006. Mountain building in the Nepal Himalaya; thermal and kinetic model. Earth and Planetary Science Letters, v. 244, p. 58-71.

Bordet, P. 1961. Recherches Géologiques dans l'Himalaya du Népal, Région du Makalu. Centre National de la Recherches Scientifiques, Paris. 275 pp.

Carosi, R., Lombardo, B., Musumeci, G., and Pertusati, P.C. 1999. Geology of the Higher Himalayan Crystallines in Khumbu Himal (eastern Nepal). Journal of Asian Earth Science, v. 17, p. 785-803.

Catlos, E.J., Gilley, L.D., and Harrison, T.M. 2002. Interpretation of monazite ages obtained via in situ analysis. Chemical Geology, v. 188, p. 193-215.

Catlos, E.J., Harrison, T.M., Kohn, M.J., Grove, M., Ryerson, F.J., Manning, C.E., and Upreti, B.N. 2001. Geochronologic and thermobarometric constraints on the evolution of the Main Central Thrust, central Nepal Himalaya. Journal of Geophysical Research, v. 106, p. 16177-16204.

Chemenda, A.I., Burg, J.-P., and Mattauer, M. 2000. Evolutionary model of the Himalaya-Tibet system: geopoem based on new modeling, geological and geophysical data. Earth and Planetary Science Letters, v. 174, p. 397-409.

Cheng, H., King, R.L., Nakamura, E., Vervoort, J.D., and Zhou, Z. 2008. Coupled Lu-Hf and Sm-Nd geochronology constrains garnet growth in ultra-high-pressure eclogites from the Dabie orogen. Journal of Metamorphic Geology, v. 26, p. 741-758.

Colchen, M., Le Fort, P., and Pêcher, A. 1986. Annapurna-Manaslu-Ganesh Himal. Centre National de la Recherches Scientifiques, Paris. 136 pp.

Coleman, M.E. 1998. U-Pb constraints on Oligocene-Miocene deformation and anatexis within the central Himalaya, Marsyandi Valley, Nepal. American Journal of Science, v. 298, p. 553-571.

Coleman, M.E. and Hodges, K.V. 1998. Contrasting Oligocene and Miocene thermal histories from the hanging wall and footwall of the South Tibetan detachment in the central Himalaya from $^{40}Ar/^{39}Ar$ thermochronology, Marsyandi Valley, central Nepal. Tectonics, v. 17, p. 726-740.

Corrie, S.L. and Kohn, M.J. 2008. Trace-element distributions in silicates during prograde metamorphic reactions: implications for monazite formation. Journal of Metamorphic Geology, v. 26, p. 451-464.

Cottle, J.M., Jessup, M.J., Newell, D.L., Horstwood, M.S.A., Noble, S.R., Parrish, R.R., Waters, D.J., and Searle, M.P. 2009. Geochronology of granulitized eclogite from the Ama Drime Massif: implications for the tectonic evolution of the South Tibetan Himalaya. Tectonics, v. 28, p. TC1002

de Sigoyer, J., Chavagnac, V., Blichert-Toft, J., Villa, I.M., Luais, B., Guillot, S., Cosca, M., and Mascle, G. 2000. Dating the Indian continental subduction and collisional thickening in the northwest Himalaya: Multichronology of the Tso Morari eclogites. Geology, v. 28, p. 487-490.

de Sigoyer, J., Guillot, S., Lardeaux, J.-M., and Mascle, G. 1997. Glaucophane-bearing eclogites in the Tso Morari dome (eastern Ladakh, NW Himalaya). European Journal of Mineralogy, v. 9, p. 1073-1083.

Dahl, P.S., Hamilton, M.A., Jercinovic, M.J., Terry, M.P., Williams, M.L., and Frei, R. 2005. Comparative isotopic and chemical geochronometry of monazite, with implications for U-Th-Pb dating by electron microprobe: an example from metamorphic rocks of the eastern Wyoming craton (USA). American Mineralogist, v. 90, p. 619-638.

Daniel, C.G., Hollister, LS., Parrish, R.R., and Grujic, D. 2003. Exhumation of the Main Central Thrust from lower crustal depths, eastern Bhutan Himalaya. Journal of Metamorphic Geology, v. 21, p. 317-334.

DeCelles, P.G., Gehrels, G.E., Najman, Y., Martin, A.J., Carter, A., and Garzanti, E. 2004. Geochronology and geochemistry of Cretaceous-early Miocene strata of Nepal: implications for timing and diachroneity of initial Himalayan orogenesis. Earth and Planetary Science Letters, v. 227, p. 313-330.

DeCelles, P.G., Gehrels, G.E., Quade, J., Ojha, T.P., Kapp, P.A., and Upreti, B.N. 1998. Neogene foreland basin deposits, erosional unroofing, and the kinematic history of the Himalayan fold-thrust belt, western Nepal. GSA Bulletin, v. 110, p. 2-21.

DeCelles, P.G., Gehrels, G.E., Quade, J., LaReau, B., and Spurlin, M. 2000. Tectonic implications of U-Pb zircon ages of the Himalayan orogenic belt in Nepal. Science, v. 288, p. 497-499.

DeCelles, P.G., Robinson, D.M., Quade, J., Ojha, T.P., Garzione, C.N., Copeland, P., and Upreti, B.N. 2001. Stratigraphy, structure, and tectonic evolution of the Himalayan fold-thrust belt in western Nepal. Tectonics, v. 20, p. 487-509.

DeCelles, P.G., Robinson, D.M., and Zandt, G. 2002. Implications of shortening in the Himalayan fold-thrust belt for uplift of the Tibetan Plateau. Tectonics, v. 21, p. 12-1 - 12-25.

Dickenson, M.P. and Hewitt, D. 1986. A garnet-chlorite geothermometer. Geological Society of America Abstracts with Programs, v. 18, p. 584.

Dunlap, W.J., Weinberg, R.F., and Searle, M.P. 1998. Karakoram fault zone rocks cool in two phases. Journal of the Geological Society of London, v. 155, p. 903-912.

Eckert, J.O., Newton, R.C., and Kleppa, O.J. 1991. The H of reaction and recalibration of garnet-pyroxene-plagioclase-quartz geobarometers in the CMAS system by solution calorimetry. American Mineralogist, v. 76, p. 148-160.

Edwards, M.A. and Harrison, T.M. 1997. When did the roof collapse? Late Miocene north-south extension in the high Himalaya revealed by Th-Pb monazite dating of the Khula Kangri granite. Geology, v. 25, p. 543-546.

England, P.C. and Molnar, P. 1993. The interpretation of inverted metamorphic isograds using simple physical calculations. Tectonics, v. 12, p. 145-157.

Ernst, W.G. 1973. Blueschist metamorphism and P-T regimes in active subduction zones. Tectonophysics, v. 17, p. 255.

Ferry, J.M. 2000. Patterns of mineral occurrence in metamorphic rocks. American Mineralogist, v. 85, p. 1573-1588.

Ferry, J.M. and Spear, F.S. 1978. Experimental calibration of partitioning of Fe and Mg between biotite and garnet. Contributions to Mineralogy and Petrology, v. 66, p. 113-117.

Florence, F.P. and Spear, F.S. 1991. Effects of diffusional modification of garnet growth zoning on P-T path calculations. Contributions to Mineralogy and Petrology, v. 107, p. 487-500.

Foster, G., Gibson, H.D., Parrish, R., Horstwood, M., Fraser, J., and Tindle, A. 2002. Textural, chemical and isotopic insights into the nature and behavior of metamorphic monazite. Chemical Geology, v. 191, p. 183-207.

Foster, G., Kinny, P., Vance, D., Prince, C., and Harris, N. 2000. The significance of monazite U-Th-Pb age data in metamorphic assemblages; a combined study of monazite and garnet chronometry. Earth and Planetary Science Letters, v. 181, p. 327-340.

Foster, G., Parrish, R.R., Horstwood, M.S.A., Chenery, S., Pyle, J., and Gibson, H.D. 2004. The generation of prograde P-T-t points and paths; a textural, compositional, and chronological study of metamorphic monazite. Earth and Planetary Science Letters, v. 228, p. 125-142.

Fraser, G., Worley, B., and Sandiford, M. 2000. High-precision geothermobarometry across the High Himalayan metamorphic sequence, Langtang Valley, Nepal. Journal of Metamorphic Geology, v. 18, p. 665-681.

Gansser, A. 1964. Geology of the Himalayas. Wiley Interscience, London-New York-Sydney, 289 pp.

Gehrels, G.E., DeCelles, P.G., Martin, A., Ojha, T.P., Pinhassi, G., and Upreti, B.N. 2003. Initiation of the Himalayan Orogen as an early Paleozoic thin-skinned thrust belt. GSA Today, v. 13, p. 4-9.

Gibson, H.D., Carr, S.D., Brown, R.L., and Hamilton, M.A. 2004. Correlations between chemical and age domains in monazite and metamorphic reactions involving major pelitic phases: an integration of ID-TIMS and SHRIMP geochronology with Y-Th-U X-ray mapping. Chemical Geology, v. 211, p. 237-260.

Godin, L., Parrish, R.R., Brown, R.L., and Hodges, K.V. 2001. Crustal thickening leading to exhumation of the Himalayan Metamorphic core of central Nepal: Insight from U-Pb Geochronology and $^{40}Ar/^{39}Ar$ Thermochronology. Tectonics, v. 20, p. 729-747.

Goscombe, B., Gray, D., and Hand, M. 2006. Crustal architecture of the Himalayan metamorphic front in eastern Nepal. Gondwana Research, v. 10, p. 232-255.

Goscombe, B. and Hand, M. 2000. Contrasting P-T paths in the Eastern Himalaya, Nepal: inverted isograds in a paired metamorphic mountain belt. Journal of Petrology, v. 41, p. 1673-1719.

Graham, C. M. and England, P.C. 1976. Thermal regimes and regional metamorphism in the vicinity of overthrust faults: an example of shear heating and inverted metamorphic zonation from southern California. Earth and Planetary Science Letters, v. 31, p. 142-152.

Graham, C.M. and Powell, R. 1984. A garnet-hornblende geothermometer: calibration, testing, and application to the Pelona Schist, Southern California. J. Met. Geol. 2, 13-31.

Groppo, C., Lombardo, B., Rolfo, F., and Pertusati, P., 2007. Clockwise exhumation path of granulitized eclogites from the Ama Drime range (eastern Himalayas). Journal of Metamorphic Geology, v. 25, p. 51-75.

Grujic, D., Hollister, L.S., and Parrish, R.R. 2002. Himalayan metamorphic sequence as an orogenic channel:insight from Bhutan. Earth and Planetary Science Letters, v. 198, p. 177-191.

Guillot, S., Garzanti, E., Baratoux, D., Marquer, D., Maheo, G., and de Sigoyer, J. 2003. Reconstructing the total shortening history of the NW Himalaya. Geochemistry, Geophysics, Geosystems, v. 4, doi:10.1029/2002GC000484 (22).

Guillot, S. and Le Fort, P. 1995. Geochemical constraints on the bimodal origin of High Himalayan leucogranites. Lithos, v. 35, p. 221-234.

Harris, N. and Massey, J. 1994. Decompression and anatexis of Himalayan metapelites. Tectonics, v. 13, p. 1537-1546.

Harrison, T.M., Grove M., Lovera O.M., and Catlos E.J. 1998. A model for the origin on Himalayan anatexis and inverted metamorphism. Journal of Geophysical Research, v. 103, p. 27017-27032.

Harrison, T.M., Grove, M., Lovera, O.M., Catlos, E.J., and D'Andrea, J. 1999a. The origin of Himalayan anatexis and inverted metamorphism: models and constraints. Journal of Asian Earth Science, v. 17, p. 755-772.

Harrison, T.M., Grove, M., McKeegan, K.D., Coath, C.D., Lovera, O.M., and Le Fort, P. 1999b. Origin and episodic emplacement of the Manaslu Intrusive Complex, central Himalaya. Journal of Petrology, v. 40, p. 3-19.

Harrison, T.M., McKeegan, K.D., and Le Fort, P. 1995. Detection of inherited monazite in the Manaslu leucogranite by $^{208}Pb/^{232}Th$ ion microprobe dating: crystallization age and tectonic implications. Earth and Planetary Science Letters, v. 133, p. 271-282.

Harrison, T.M., Ryerson, F.J., Le Fort, P., Yin, A., Lovera, O.M., and Catlos, E.J. 1997. A Late Miocene-Pliocene origin for central Himalayan inverted metamorphism. Earth and Planetary Science Letters, v. 146, p. E1-E8.

Harrison, T. M., Catlos, E. J., and Montel, J.-M. 2002. U-Th-Pb dating of Phosphate Minerals. Reviews in Mineralogy, v. 48, p. 523-552.

Hayden, L.A., Watson, E.B., and Wark, D.A. 2008. A thermobarometer for sphene (titanite). Contributions to Mineralogy and Petrology, v. 155, p. 529-540.

Henry, P., Le Pichon, X., and Goffé, B. 1997. Kinematic, thermal and petrological model of the Himalayas: constraints related to metamorphism within the underthrust Indian crust and topographic elevation. Tectonophysics, v. 373, p. 31-56.

Hodges, K., Bowring, S., Davidek, K., Hawkins, D., and Krol, M. 1998. Evidence for rapid displacement on Himalayan normal faults and the importance of tectonic denudation in the evolution of mountain ranges. Geology, v. 26, p. 483-486.

Hodges, K.V., Parrish, R.R., and Searle, M.P. 1996. Tectonic evolution of the central Annapurna Range, Nepalese Himalayas. Tectonics, v. 15, p. 1264-1291.

Hoisch, T.D. 1990. Empirical calibration of six geobarometers for the mineral assemblage quartz+muscovite+biotite+plagioclase+garnet. Contributions to Mineralogy and Petrology, v. 104, p. 225-234.

Holland, T.J.B. 1980. The reaction albite = jadeite + quartz determined experimentally in the range 600-1200°C. American Mineralogist, v. 65, p. 129-134.

Hubbard, M.S. 1996. Ductile shear as a cause of inverted metamorphism: example from the Nepal Himalaya. Journal of Geology, v. 104, p. 493-499.

Hubbard, M.S. and Harrison, T.M. 1989. ^{40}Ar/^{39}Ar age constraints on deformation and metamorphism in the Main Central Thrust zone and Tibetan Slab, eastern Nepal Himalaya. Tectonics, v. 8, p. 865-880.

Huerta, A.D., Royden, L.H., and Hodges, K.V. 1998. The thermal structure of collisional orogens as a response to accretion, erosion, and radiogenic heating. Journal of Geophysical Research, v. 103, p. 15287-15302.

Huerta, A.D., Royden, L.H., and Hodges, K.V. 1999. The effects of accretion, erosion, and radiogenic heat on the metamorphic evolution of collisional orogens. Journal of Metamorphic Geology, v. 17, p. 349-366.

Inger, S. and Harris, N.B.W. 1992. Tectonothermal evolution of the High Himalaya Crystalline sequence, Langtang Valley, northern Nepal. Journal of Metamorphic Geology, v. 10, p. 439-452.

Jamieson, R.A., Beaumont, C., Hamilton, J., and Fullsack, P. 1996. Tectonic assembly of inverted metamorphic sequences. Geology, v. 24, p. 839-842.

Jamieson, R.A., Beaumont, C., Nguyen, M.H., and Lee, B. 2002. Interaction of metamorphism, deformation, and exhumation in large convergent orogens. Journal of Metamorphic Geology, v. 20, p. 1-16.

Jamieson, R.A., Beaumont, C., Medvedev, S., and Nguyen, M.H. 2004. Crustal channel flows: 2. Numerical models with implications for metamorphism in the Himalayan-Tibetan orogen. Journal of Geophysical Research, v. 109, p. B6.

Jessup, M.J, Newell, D.L., Cottle, J.M., Berger, A.L., and Spotila, J.A. 2008. Orogen-parallel extension and exhumation enhanced by denudation in the trans-Himalayan Arun River gorge, Ama Drime Massif, Tibet-Nepal. Geology, v. 36, p. 587-590.

Johnson, M.R.W., Oliver, G.J.H., Parrish, R.R., and Johnson, S.P. 2001. Synthrusting metamorphism, cooling, and erosion of the Himalayan Kathmandu Complex, Nepal. Tectonics, v. 20, p. 394-415.

Kaneko, Y. 1995. Thermal structure in the Annapurna region, central Nepal Himalaya: implication for the inverted metamorphism. Journal of Mineralogy, Petrology, and Economic Geology, v. 90, p. 143-154.

Kaneko, Y., Katayama, I., Yamamoto, H., Misawa, K., Ishikawa, M., Rehman, H.U., Kausar, A.B., and Shiraishi, K. 2003. Timing of Himalayan ultrahigh-pressure metamorphism: sinking rate and subduction angle of the Indian continental crust beneath Asia. Journal of Metamorphic Geology, v. 21, p. 589-599.

Kelsey, D.E., Clark, C., and Hand, M. 2008. Thermobarometric modeling of zircon and monazite growth in melt-bearing systems: examples using model metapelitic and metapsammitic granulites. Journal of Metamorphic Geology, v. 26, p. 199-212.

Kohn, M.J. 2004. Oscillatory- and sector-zoned garnets record cyclic (?) rapid thrusting in central Nepal. Geochemistry, Geophysics, Geosystems, v. 5, Q12014.

Kohn, M.J. 2005. Monazite chemistry and chronology reveal diachronous movement of the Main Central Thrust, central Nepal. Geochimica et Cosmochimica Acta, v. 69 Supplement, p. 30.

Kohn, M.J. 2008. P-T-t data from central Nepal support critical taper and repudiate large-scale channel flow of the Greater Himalayan Sequence. GSA Bulletin, v. 120, p. 259-273.

Kohn, M.J. 2009. Models of garnet differential geochronology. Geochimica et Cosmochimica Acta, v. 73, p. 170-182.

Kohn, M.J. and Malloy, M.A. 2004. Formation of monazite via prograde metamorphic reactions among common silicates: implications for age determinations. Geochimica et Cosmochimica Acta, v. 68, p. 101-113.

Kohn, M.J. and Parkinson, C.D. 2002. Petrologic case for Eocene slab breakoff during the Indo-Asian collision, Geology, v. 30, p. 591-594.

Kohn, M.J. and Spear, F.S. 1990. Two new geobarometers for garnet amphibolites, with applications to southeastern Vermont. American Mineralogist, v. 75, p. 89-96.

Kohn, M.J. and Spear, F.S. 2000. Retrograde Net Transfer Reaction (ReNTR) Insurance for P-T Estimates. Geology, v. 28, p. 1127-1130.

Kohn, M.J., Catlos, E.J., Ryerson, F.J., and Harrison T.M. 2001. Pressure-Temperature-time Path Discontinuity in the MCT Zone, Central Nepal. Geology, v. 29, p. 571-574.

Kohn, M.J., Paul, S.K., and Corrie, S.L. 2010. The lower Lesser Himalayan Sequence: a Paleoproterozoic arc on the northern margin of the Indian Plate. GSA Bulletin, v. 122, p. 323-335.

Kohn, M.J., Wieland, M., Parkinson, C.D., and Upreti, B.N. 2004. Miocene faulting at plate tectonic velocity in the Himalaya of central Nepal. Earth and Planetary Science Letters, v. 228, p. 299-310.

Kohn, M.J., Wieland, M., Parkinson, C.D., and Upreti, B.N. 2005. Five generations of monazite in Langtang gneisses: implications for geochronology of the Himalayan metamorphic core. Journal of Metamorphic Geology, v. 23, p. 399-406.

Koziol, A.M. and Newton, R.C. 1988. Redetermination of the anorthite breakdown reaction and improvement of the plagioclase-garnet-Al$_2$SiO$_5$-quartz geobarometer. American Mineralogist, v. 73, p. 216-223.

Laird, J. 1988. Chlorites: Metamorphic petrology. Hydrous phyllosilicates (exclusive of micas). Reviews in Mineralogy, v. 19, p. 405-453.

Lapen, T.J., Johnson, C.M., Baumgartner, L.P., Mahlen, N.J., Beard, B.L., and Amato, J.M. 2003. Burial rates during prograde metamorphism of an ultra-high pressure terrane: and example from Lago di Cignana, western Alps, Italy. Earth and Planetary Science Letters, v. 215, p. 57-72.

Larson, K.M., Bürgmann, R., Bilham, R., and Freymueller, J.T. 1999. Kinematics of the India- Eurasia collision zone from GPS measurements. Journal of Geophysical Research, v. 104, p. 1077-1093.

Lavé, J. and Avouac, J.P. 2001. Fluvial incision and tectonic uplift across the Himalaya of central Nepal. Journal of Geophysical Research, v. 106, p. 26,561-26,591.

Le Fort, P. 1975. Himalaya, the collided range, present knowledge of the continental arc. American Journal of Science, v. 275A, p. 1-44.

Le Fort, P. 1996. Evolution of the Himalaya. In: Yin, A., Harrison, T.M. (eds.) The Tectonic Evolution of Asia. Cambridge University Press, p. 95-109.

Le Fort, P., Cuney, M., Deniel, C., France-Lanord, C., Sheppard, S.M.F., Upreti, B.N., and Vidal, P. 1987. Crustal generation of the Himalayan leucogranites. Tectonophysics, v. 134, p. 39-57.

Li, D., Liao, Q., Yuan, Y., Wan, Y., Liu, D., Zhang, X., Yi, S., Cao, S., and Xie, D. 2003. SHRIMP U-Pb zircon geochronology of granulites at Rimana (southern Tibet) in the central segment of the Himalayan orogen. Chinese Science Bulletin, v. 48, p. 2647-2650.

Liu, Y., Siebel, W., Massonne, H.-J., and Xiao, X. 2007. Geochronological and petrological constraints for tectonic evolution of the central Greater Himalayan Sequence in the Kharta area, southern Tibet. Journal of Geology, v. 115, p. 215-230.

Lombardo, B., Pertusati, P., and Borghi, S. 1993. Geology and tectono-magmatic evolution of the eastern Himalaya along the Chomolungma-Makalu transect. In: Treloar, P.J., Searle, M.P. (eds.). Himalayan Tectonics. Geological Society of London, Special Publication, v. 74, p. 341-355.

Lombardo, B. and Rolfo, F. 2000. Two contrasting eclogite types in the Himalayas: implications for the Himalayan orogeny. Journal of Geodynamics, v. 30, p. 37-60.

Ludwig, K.R. 2003. User's Manual for Isoplot 3.00: A Geochronological Toolkit for Microsoft Excel. Berkeley Geochronology Center Special Publication, Berkeley.

Macfarlane, A.M. 1993. The chronology of tectonic events in the crystalline core of the Himalaya, Langtang National Park, central Nepal. Tectonics, v. 12, p. 1004-1025.

Macfarlane, A.M. 1995. An evaluation of the inverted metamorphic gradient at Langtang National Park, central Nepal Himalaya. Journal of Metamorphic Geology, v. 13, p. 595-612.

Mahéo, G., Guillot, S., Blichert-Toft, J., Rolland, Y., and Pêcher, A. 2002. A slab breakoff model for the Neogene thermal evolution of south Karakorum and south Tibet. Earth and Planetary Science Letters, v. 195, p. 45-58.

Martin, A.J., Gehrels, G.E., DeCelles, P.G. 2007. The tectonic significance of (U,Th)/Pb ages of monazite inclusions in garnet from the Himalaya of central Nepal. Chemical Geology, v. 244, p. 1-24.

Martin, A.J., DeCelles, P.G., Gehrels, G.E., Patchett, P.J., and Isachsen, C. 2005. Isotopic and structural constraints on the location of the Main Central thrust in the Annapurna Range, central Nepal Himalaya. GSA Bulletin, v. 117, p. 926-944.

Martin, A.J., Ganguly, J., and DeCelles, P.G. 2010, Metamorphism of Greater and Lesser Himalayan rocks exposed in the Modi Khola valley, central Nepal. Contributions to Mineralogy and Petrology, v. 159, p. 203-223.

Molnar, P. and England, P.C. 1990. Temperatures, heat flux, and frictional stress near major thrust faults. Journal of Geophysical Research, v. 95, p. 4833-5856.

Morimoto, N., Fabries, J., Ferguson, A.K., Ginzburg, I.V., Ross, M., Seifert, F.A., Zussman, J., Aoki, K., and Gottardi, G. 1988. Nomenclature of pyroxenes. American Mineralogist, v. 73, p. 1123-1133.

Mukherjee, B.K. and Sachan, H.K. 2001. Discovery of coesite from Indian Himalaya: a record of ultra-high pressure metamorphism in Indian continental crust. Current Science, v. 81, p. 1358-1361.

Murphy, M.A. and Harrison, T.M. 1999. Relationship between leucogranites and the Qomolangma detachment in the Rongbuk Valley, south Tibet. Geology, v., 27, p. 831-834.

Nelson, K.D., Zhao, W., Brown, L.D., and Project INDEPTH. 1996. Partially molten crust beneath Southern Tibet: synthesis of project INDEPTH results. Science, v. 274, p. 1684-1688.

O'Brien, P.J. 2001. Subduction followed by collision: Alpine and Himalayan examples. Physics of the Earth and Planetary Interiors, v. 127, p. 277-291.

O'Brien, P.J., Zotov, N., Law, R., Khan, M.A., and Jan, M.Q. 2001. Coesite in Himalayan eclogite and implications for models of India-Asia collision. Geology, v. 29, p. 435-438.

Overstreet, W.C. 1967. The geologic occurrence of monazite. Geological Survey Professional Papers, v. 530, p. 1-327.

Parkinson, C.D. and Kohn, M.J. 2002. A first record of eclogite from Nepal and consequences for the tectonic evolution of the Greater Himalayan Sequence. Eos, Transactions, American Geophysical Union, v. 83, p. V42A-11.

Parrish, R.R. 1990. U-Pb dating of monazite and its application to geological problems. Canadian Journal of Earth Science, v. 27, p. 1431-1450.

Parrish, R.R., Gough, S.J., Searle, M.P., and Waters, D.J. 2006. Plate velocity exhumation of ultrahigh-pressure eclogites in the Pakistan Himalaya. Geology, v. 34, p. 989-992.

Parrish, R.R. and Hodges, K.V. 1996. Isotopic constraints on the age and provenance of the Lesser and Greater Himalayan sequences, Nepalese Himalaya. GSA Bulletin, v. 108, p. 904-911.

Pattison, D.R.M. and Newton, R.C. 1989. Reversed experimental calibration of the garnet-clinopyroxene Fe-Mg exchange thermometer. Contributions to Mineralogy and Petrology, v. 101, p. 87-103.

Pearson, O.N. and DeCelles, P.G. 2005. Structural geology and regional tectonic significance of the Ramgarh thrust, Himalayan fold-thrust belt of Nepal. Tectonics, v. 24, p. TC4008.

Pêcher, A. 1989. The metamorphism in the central Himalaya. Journal of Metamorphic Geology, v. 7, p. 31-41.

Pêcher, A. and Le Fort, P. 1986. The metamorphism in central Himalaya, its relations with the thrust tectonics. In: Le Fort, P., Colchen, M., Montenat, C. (eds.) Évolution des domains orogéniques d'Asie méridionale (de la Turquie à l'Indoneasie). Science de la Terre, v. 47, p. 285-309.

Pognante, U. and Benna, P. 1993. Metamorphic zonation, migmitization and leucogranites along the Everest transect of Eastern Nepal and Tibet: Record of an exhumation history. In: Treloar, P.J., Searle, M.P. (eds.). Himalayan Tectonics. Geological Society of London, Special Publication, v. 74, p. 323-340.

Pognante, U. and Spencer, D.A. 1991. First report of eclogites from the Himalayan belt, Kaghan valley (northern Pakistan). European Journal of Mineralogy, v. 3, p. 613-618.

Pyle, J.M. and Spear, F.S. 1999. Yttrium zoning in garnet: Coupling of major and accessory phases during metamorphic reactions. Geological Materials Research, v. 1, p. 2-49.

Pyle, J.M. and Spear, F.S. 2003. Four generations of accessory-phase growth in low-pressure migmatites from SW New Hampshire. American Mineralogist, v. 88, p. 338-351.

Pyle, J.M., Spear, F.S., Rudnick, R.L., and McDonough, W.F. 2001. Monazite-xenotime-garnet equilibrium in metapelites and a new monazite-garnet thermometer. Journal of Petrology, v. 42, p. 2083-2107.

Pyle, J.M., Spear, F.S., Cheney, J.T., and Layne, G. 2005. Monazite ages in the Chesham Pond Nappe, SW New Hampshire, USA: implications for assembly of central New England thrust sheets. American Mineralogist, v. 90, p. 592-606.

Richards, A., Argles, T., Harris, N., Parrish, R., Ahmad, T., Darbyshire, F., and Draganits, E. 2005. Himalayan architecture constrained by isotopic tracers from clastic sediments. Earth and Planetary Science Letters, v. 236, p. 773-796.

Richards, A., Parrish, R., Harris, N., Argles, T., and Zhang, L. 2006. Correlation of lithotectonic units across the eastern Himalaya, Bhutan. Geology, v. 34, p. 341-344.

Robinson, D.M., DeCelles, P.G., Patchett, P.J., and Garzione, C.N. 2001. The kinematic evolution of the Nepalese Himalaya interpreted from Nd isotopes. Earth and Planetary Science Letters, v. 192, p. 507-521.

Robinson, D.M., DeCelles, P.G., Garzione, C.N., Pearson, O.N., Harrison, T.M., and Catlos, E.J. 2003. Kinematic model for the Main Central thrust in Nepal. Geology, v. 31, p. 359-362.

Robinson, D.M., DeCelles, P.G., and Copeland, P. 2006. Tectonic evolution of the Himalayan thrust belt in western Nepal: implications for channel flow models. GSA Bulletin, v. 118, p. 865-885.

Royden, L. H. 1993. The steady state thermal structure of eroding orogenic belts and accretionary prisms. Journal of Geophysical Research, v, 98, p. 4487-4507.

Sakai, H. 1983. Geology of the Tansen Group of the Lesser Himalaya in Nepal. Memoirs of the Faculty of Science Kyushu University Series D Geology, v. 25, p. 337-397.

Schärer, U. 1984. The effect of initial ^{230}Th disequilibrium on U-Pb ages: The Makalu case. Earth and Planetary Science Letters, v. 67, p. 191-204.

Scherer, E.E., Cameron, K.L., and Blichert-Toft, J. 2000. Lu-Hf geochronology: closure temperature relative to the Sm-Nd system and the effects of trace mineral inclusions. Geochimica et Cosmochimica Acta, v. 64, p. 3413-3432.

Scherer, E., Muenker, C., and Mezger, K. 2001. Calibration of the lutetium-hafnium clock. Science, v. 293, p. 683-687.

Searle, M.P. and Godin, L. 2003. The South Tibetan detachment and the Manaslu leucogranite; a structural reinterpretation and restoration of the Annapurna-Manaslu Himalaya, Nepal. Journal of Geology, v. 111, p. 505-523.

Searle, M.P., Law, R.D., Godin, L., Larson, K.P., Streule, M.J., Cottle, J.M., and Jessup, M.J. 2008. Defining the Himalayan Main Central Thrust in Nepal. Journal of the Geological Society, London 165, 523-534.

Simpson, R.L., Parrish, R.R., Searle, M.P., and Waters, D.J. 2000. Two episodes of monazite crystallization during metamorphism and crustal melting in the Everest region of the Nepalese Himalaya. Geology, v. 28, p. 403-406.

Söderlund, U., Patchett, P.J., Vervoort, J.D., and Isachsen, C.E. 2004. The ^{176}Lu decay constant determined by Lu-Hf and U-Pb isotope systematics of Precambrian mafic intrusions. Earth and Planetary Science Letters, v. 219, p. 311-324.

Spear, F.S. and Pyle, J.M. 2002. Apatite, monazite and xenotime in metamorphic rocks. Reviews in Mineralogy, v. 48, p. 293-335.

Spear, F.S., Kohn, M. J., Florence, F. P., and Menard, T. 1990. A model for garnet and plagioclase growth in pelitic schists: implications for thermobarometry and P-T path determinations. Journal of Metamorphic Geology, v. 8, p. 683-696.

Spear, F.S., Kohn, M.J., and Paetzold, S. 1995. Petrology of the regional sillimanite zone, west-central New Hampshire, USA, with implications for the development of inverted isograds. American Mineralogist, v. 80, p. 361-376.

Stewart, R.J., Hallet, B., Zeitler, P.K., Allen, C., and Trippett, D. 2004. Extreme localized erosion in the eastern Himalayan syntaxis; results of fission-track and U-Pb ICP/MS dating of detrital zircons from Brahmaputra River sands. Abstracts with Programs, Geological Society of America, v. 36, p. 282.

Tonarini, S., Villa, I.M., Oberli, F., Meier, M., Spencer, D.A., Pognante, U., and Ramsay, J.G. 1993. Eocene age of eclogite metamorphism in Pakistan Himalaya; implications for India-Eurasia collision. Terra Nova, v. 5, p. 13-20.

Tomkins, H.S., Powell, R., and Ellis, D.J. 2007. The pressure dependence of the zirconium-in-rutile thermometer. Journal of Metamorphic Geology, v. 25, p. 703-713.

Treloar, P.J., O'Brien, P.J., Parrish, R.R., and Khan, M.A. 2003. Exhumation of early Tertiary, coesite-bearing eclogites from the Pakistan Himalaya. Journal of the Geological Society of London, v. 160, p. 367-376.

Valdiya, K.S. 1995. Proterozoic sedimentation and pan-African geodynamic development in the Himalaya. Precambrian Research, v. 74, p. 35-55.

Vannay, J.-C. and Hodges, K.V. 1996. Tectonomorphic evolution of the Himalayan metamorphic corebetween the Annapurna and Dhaulagiri, central Nepal. Journal of Metamorphic Geology v. 14, p. 635-656.

Vervoort, J.D., Patchett, P.J., Soderlund, U., and Baker, M. 2004. Isotopic composition of Yb and the determination of Lu concentrations and Lu/Hf ratios by isotope dilution using MC-ICPMS. Geochemistry, Geophysics, Geosystems, v. 5, p. 1-15.

Viskupic, K. and Hodges, K.V. 2001. Monazite-xenotime thermochronometry: methodology and an example from the Nepalese Himalaya. Contributions to Mineralogy and Petrology, v. 141, p. 233-247.

Watson, E.B., Wark, D.A., and Thomas, J.B. 2006. Crystallization thermometers for zircon and rutile. Contributions to Mineralogy and Petrology, v. 151, p. 413-433.

Will, T.M. and Schmädicke, E. 2001. A first find of retrogressed eclogites in the Odenwald Crystalline Complex, Mid-German Crystalline Rise, Germany: evidence for a so far unrecognized high-pressure metamorphism in the Cental Variscides. Lithos, v. 59, p. 109-125.

Wing, B.A., Ferry, J.M., and Harrison, T.M. 2003. Prograde destruction and formation of monazite and allanite during contact and regional metamorphism of pelites: petrology and geochronology. Contributions to Mineralogy and Petrology v. 145, p. 228-250.

Yin, A. 2006. Cenozoic tectonic evolution of the Himalayan orogen as constrained by along-strike variation of structural geometry, exhumation history, and foreland sedimentation. Earth-Science Reviews, v. 76, p. 1-131.

Yin, A. and Harrison, T.M. 2000. Geologic evolution of the Himalayan-Tibet orogen. Annual Review of Earth and Planetary Sciences, v. 28, p. 211-280.

Zeitler, P.K., Koons, P.O., Bishop, M.P., Chamberlain, C.P., Craw, D., Edwards, M.A., Hamidullah, S., Jan, M.Q., Khan, M.A., Khattak, M.U.K., Kidd, W.S.F., Mackie, R.L., Meltzer, A.S., Park, S.K., Pecher, A., Poage, M.A., Sarker, G., Schneider, D.A., Seeber, L., and Shroder, J.F. 2001. Crustal reworking at Nanga Parbat, Pakistan: Metamorphic consequences of thermal-mechanical coupling facilitated by erosion. Tectonics, v. 20, p. 712-728.

Zhao, W., Nelson K.D., and Project INDEPTH. 1993. Deep seismic reflection evidence for continental underthrusting beneath southern Tibet. Nature, v. 366, p. 557-559.